UiT The Arctic University of Norway

Faculty of Science and Technology
Department of Physics and Technology

Assessing ice rate and ice load at Davvi wind farm using WRF model with wind turbine scheme

Isak Leonhardsen

EOM-3901 Master's thesis in energy, climate and environment 30 SP
May 2024

This thesis document was typeset using the *UiT Thesis LaTeX Template*.
© 2024 – http://github.com/egraff/uit-thesis

Abstract

Wind farms located in cold climates are exposed to temperatures under the design limit and icing conditions, where the main challenges are production losses and mechanical failures. The goal of this thesis is to investigate the impact related to icing on the location of Davvi wind farm using Weather Research and Forecasting (WRF) model. The thesis have investigated the icing intensity and production loss at Davvi wind farm using WRF with a wind turbine scheme.

Weather parameter from the model are used to calculate icing hours above the icing rate thresholds of 10 g/h, 50 g/h and 250 g/h for the proposed turbine locations. The Makkonen ice accretion model is used for icing rates calculations. To estimate production loss, an experimental method where ice build up only occur during an ongoing icing period is used.

Estimation show that the turbine location higher up in the terrain experience greater icing severity, due to lower temperature and higher liquid water content (LWC). Icing estimation show a greater variability in icing severity than what stated in NVE's 2009 report of Norway. Turbine location T26 with the highest icing severity experienced 17.75% annual meteorological icing, while T22, the location with lowest icing severity, experienced 3.17%. Based IEA Task 19 Ice Site Classification, this correspond to an annual production loss of > 20% and 3-12%, respectively. The experimental production result show a slightly lower production loss, where the locations had an annual production loss of 19.86% and 4.16% for 2017, respectively. Differences between data with and without turbines, shows that wind turbines positioned downstream, relative to the wind direction, experienced wake effect created by upstream turbines. The maximum annual mean wind speed difference is 1.425 m/s, and the greatest difference in icing rate above 10 g/h is 113 hours. Icings maps like in NVE's 2009 report, where the wind turbine scheme is not included, could therefore expect higher icings rate than what a wind park would experience. This show the importance of including wind turbine for wind and ice siting at a location for accurate assessments.

Acknowledgement

I want to thank my supervisor Yngve Birkelund and co-supervisor Pravin Punde, for great guidance and discussions. I am especially thankful for their constant availability and willingness to answer my questions.

Thanks to Svein Skudal Aase and the rest of St1, for providing great engagement and essential data to the thesis.

And thanks to my friends and family, for their unquestionable support. Special thanks to my girlfriend, Anni Alice Rapp, for unparalleled support throughout my years at university, couldn't have done it without you!

Isak Leonhardsen

Contents

List of Figures

List of Tables

1 Introduction

1.1 Background

Norway is heading for 27% and 80% reduction of green gas emissions for 2030 and 2050 respectively. In 2016 when Paris Agreement was signed, 140 TWh came from fossil fuel. To replace fossil consumption, roughly 100 TWh of additional renewable energy capacity was targeted. We are ways away from achieving this and is facing net electricity deficit from 2028 to 2032. About three times the current renewable power production is needed for 2050, total about 390 TWh where onshore wind would contribute 40-50 TWh [Alvik et al., 2023]. Norway's 65 active wind farms produced 14.8 TWh in 2022 [Wold et al., 2022].

Wind farms located in cold climates are exposed to temperatures under the design limit and icing conditions. Production losses and increased mechanical failure due to ice loads are the main challenges for operating under such conditions [Bredesen et al., 2017].

The company Grenselandet AS, with main owner St1, has applied for licence application to build and operate Davvi wind farm in Lebesby, Finnmark county. The park would have an installed effect of 800 MW, and lies in an area where Norges vassdrag -og energi direktorat (NVE) in a report from 2009 calculated 500 - 1000 icing hours per year.

Atmospheric icing is a general term for frozen water substance, and ice accretion can cause severe damage to the structure [Farzaneh, 2008, Fikke, 2005],

as well as hindering optimal power production due to disruptive aerodynamics [Homola, 2011]. The planned area of Davvi wind farm is located in altitudes of around 500 - 800 m above sea level [Grenselandet AS, 2022], and could therefore face challenges of moderate - strong ice intensity [Fikke et al., 2007].

1.2 Previous work

Using outputs from Numerical Weather Prediction (NWP) and estimating in-cloud ice accretion on a standard reference cylinder is proven to provide good approximation. Ice accretion calculation using Weather Research Forecast (WRF) outputs on exposed high altitude sites in Norway predicted the timing and duration of icing events with good skill [Ingvaldsen et al., 2019].

Performance of wind prediction in complex terrain proves to be more accurate in higher resolutions [Solbakken et al., 2021]. This also applies for in-cloud icing parameters, where the accuracy is greater in higher resolution. [Nygaard et al., 2011] relates this to orographic lifting, where the height of the mountain top is strongly dependent on horizontal resolution.

Modelling an ice event using Computational Fluid Dynamic (CFD) solver show that a NREL 5 MW turbine has a significant power loss of 27% between 8 and 10 m/s [Homola et al., 2011]. Other power loss estimations show that power production drops already in the early process of rime icing due to the increase in drag [Turkia et al., 2013].

1.3 Goal of thesis

The goal of this thesis is to investigate the impact related to icing on the location of Davvi wind farm. We will focus on assessing atmospheric icing, and identify parameter for meteorological icing on wind turbines. We will estimate an annual icing intensity for 2017 on the suggested turbine location of Davvi wind farm using WRF model with wind turbine scheme.

Additionally, the thesis aims to estimate the production loss due to icing load, which will provide valuable insights into the economic impact on energy production.

Secondary goal of the thesis was to build further on the understanding of icing estimation and weather simulation using Numerical Weather Predictions model, including wind turbines inside the simulation.

1.4 Thesis structure

Chapter 2 consist of theory of wind, wind power and atmospheric icing. We start to introduce meteorology and weather, look at how wind is created, then to focus on how wind power in extracted. We look into the different type of atmospheric icing and how we estimate it using Numerical Weather Prediction model. Parts of this chapter was copied from my project paper "Icing on Davvi wind farm" delivered December 2023.

Chapter 3 describes the methodology of the thesis. It gives and description of the site of Davvi wind farm, then it goes through how the models work and how the ice accretion estimation is performed. It introduces the New European Weather Atlas (NEWA), NVE's icing map and statistical metrics for model validation. Parts of this chapter was copied from my project paper "Icing on Davvi wind farm" delivered December 2023.

Chapter 4 showcase and discusses the result given by the model. It starts with model validation, then model comparison with NEWA results and finally annual weather, icing results and production estimation. We compare different location to each other, compare with and without turbine scheme and discuss the results.

Chapter 5 gives a conclusion about the results, before it delves into further research.

2 Theory

2.1 Meteorology and weather

The amount of solar radiation received varies with latitude, time of day and time of year. Earth spins around the sun at a rate of 1 rotation in 365.25 days. The non-perfect circular orbit means that the distance between Earth and the Sun varies with time of year, at January 3 the distance is about $147 \cdot 10^6$ kilometer and is called perihelion, while on July 4 the distance is $152 \cdot 10^6$ kilometers and is called aphelion [Lutgens et al., 2019]. Figure 2.1 illustrates Earth's orbit, dark wavy line show Earth's center path [Stull, 2018]. Earth receives up to 7% more energy from the Sun at perihelion, but since it occurs during northern hemisphere winter, it plays a minor role in seasonal temperature variations [Lutgens et al., 2019].

The biggest contributions to the seasons is the angle of which the solar energy hits the surface. The maximum amount of energy hits when the Sun is directly overhead and the solar rays hit at an 90^o angle. At higher latitudes, the solar ray hits the surface with lower angles and receives less solar radiations. In figure 2.2 we can see how the angle is decreasing as we go from equatorial latitudes towards the pole, also note that the atmosphere is ticker at higher latitudes [Lutgens et al., 2019].

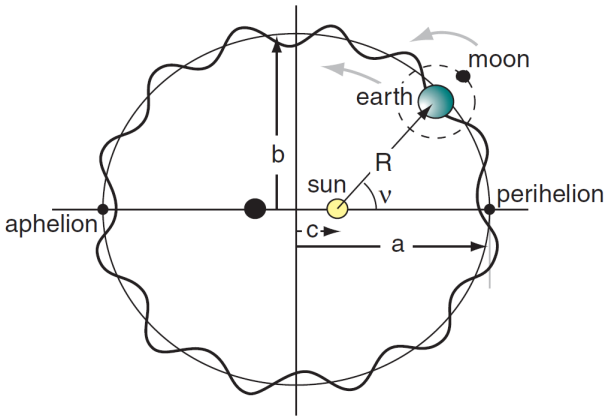

Figure 2.1: Earth's orbit as seen from above Earth's north pole [Stull, 2018].

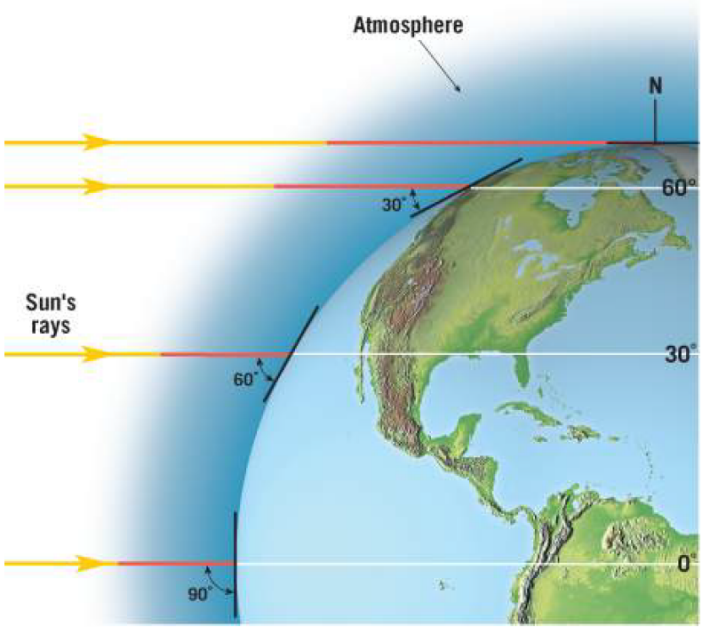

Figure 2.2: Solar radiation angle varies with latitude [Lutgens et al., 2019].

2.2 Wind

Wind is generated as the Sun's uneven heating of the surface, influenced by latitude, season and surface properties. The heat is transported upwards by turbulent sensible and latent heat fluxes, and will create a temperature gradient

in the atmosphere. Air pressure is a measure for the mass of air above a location and will decrease with height. Warm air is less dense than cold air and will rise, causing a decrease in air pressure and creating a horizontal pressure gradient [Emeis, 2018]. Pressure gradient force is described in equation 2.1,

$$F_{PG} = -\frac{1}{\rho}\frac{\Delta p}{\Delta d} \tag{2.1}$$

where Δp is the pressure change over the distance Δd, and ρ is density of air. Note the minus sign, this means that if the pressure is increasing the force will pushing the air in the opposite direction, in other words air from high pressure regions get forced to low pressure regions. This force is at right angels to the isobars showing constant pressure. The tighter the isobars are packed together, the greater the pressure gradient, the greater indication for strong winds [Stull, 2018].

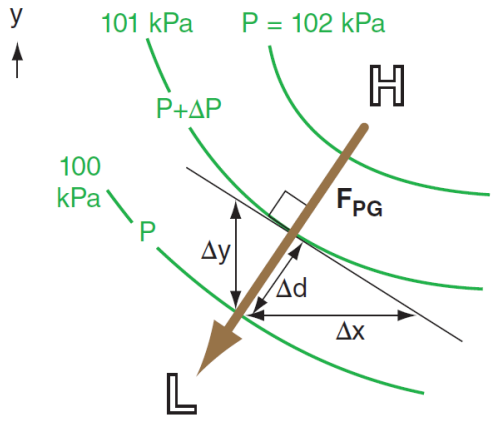

Figure 2.3: Pressure-gradient force (F_{PG}) direction as it goes from high pressure regions (H) to low pressure regions (L) [Stull, 2018].

Arrow in the figure 2.3 show that the direction of the pressure-gradient force (F_{PG}) has direction perpendicular to the isobars.

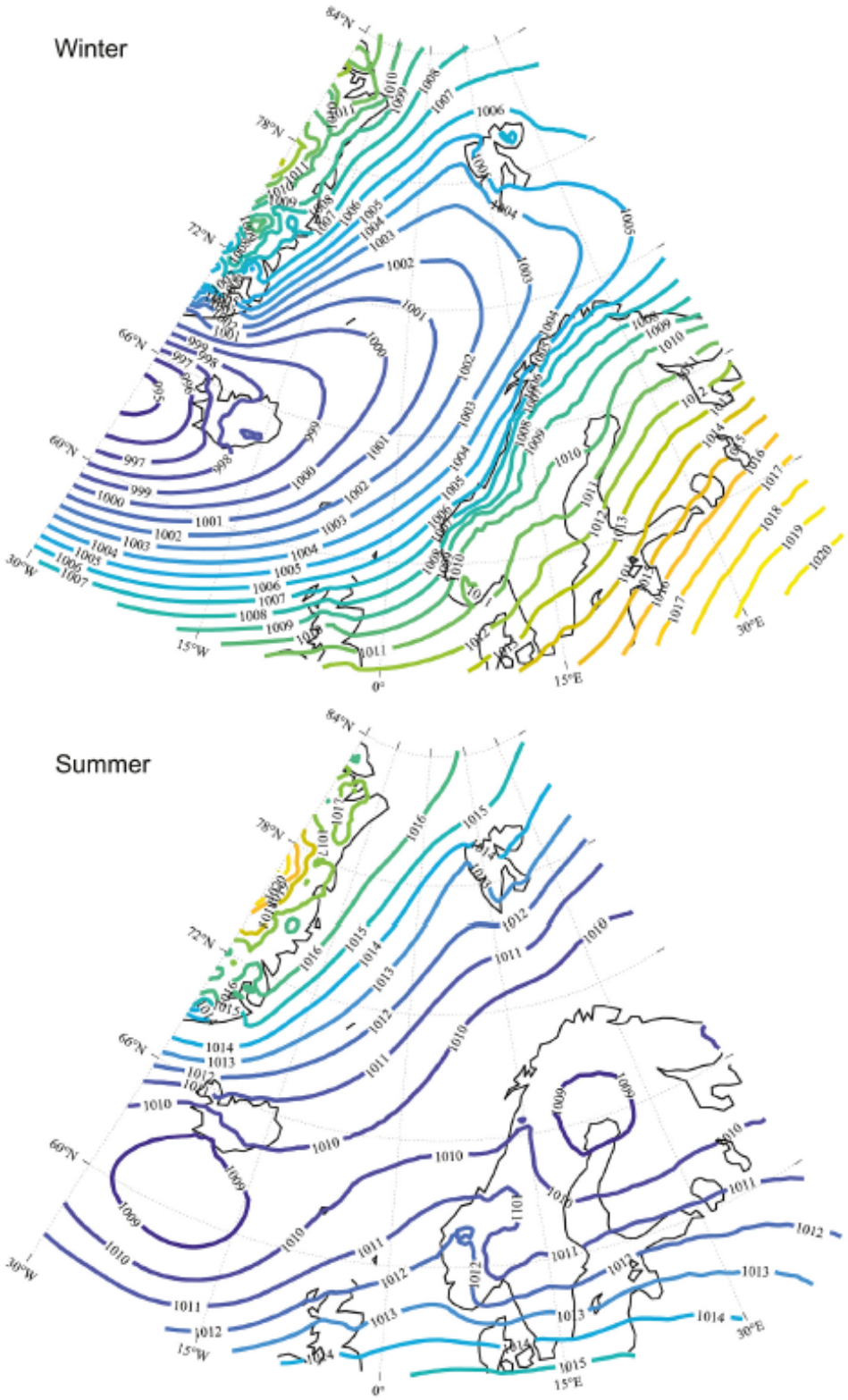

Figure 2.4: Mean sea level pressure for winter (September 2014 - March 2015) and summer (April 2015 - August 2015) [Solbakken et al., 2021].

Since air pressure decrease with altitude, pressure needs to be converted into sea level pressure in order to show pressure pattern across Earth's surface. Pressure is indicated with isobars showing constant pressure. When drawn on a map we can then easily identify high-pressure systems and low-pressure systems. High pressure systems is also called anticyclones and often provide dry conditions. Low-pressure systems is called cyclones and often provide clouds, precipitation and windy conditions [Lutgens et al., 2019]. In figure 2.4 we can see a steeper pressure gradient towards the low-pressure system south of Greenland during the winter months.

However, the wind does not move across the isobars in right angels, as the wind is deviated by Earth's rotation. This deviation is called the Coriolis force and causes wind to be deflected to the right in the northern hemisphere and to the left in the southern hemisphere. This force will not impact the magnitude of the wind, it will only modify the direction of the airflow [Lutgens et al., 2019]. Using the angular rotation rate of Earth (Ω) we can define the Coriolis force,

$$F_{CF} = 2m \cdot \Omega \cdot U \cdot \sin(\phi) \tag{2.2}$$

where m is mass, U is wind speed and ϕ is latitude. Since Ω is fixed, this means that the Coriolis force depends on latitude, mass and wind speed [Stull, 2018]. At the equatorial latitude the Coriolis force is non-existent $\sin(0^o) = 0$ and increasing towards the poles $\sin(70^o) \sim 0.94$, meaning the deflection will increase as an air parcel moves from the equator towards the poles. As the wind accelerate from the influence of the pressure-gradient force the deflection will also increase, until its deflection directs it parallel with the isobars, at that point it is in balance between the pressure-gradient force and the Coriolis force and will flow with constant speed parallel to the isobars. This is called geostrophic wind [Lutgens et al., 2019]. If we combine the equation 2.1 and 2.2 we get the equation for the special case [Stull, 2018]

$$Geostrophic\ wind: 0 = -\frac{1}{\rho}\frac{\Delta p}{\Delta d} + 2m \cdot \Omega \cdot U \cdot \sin(\phi) \tag{2.3}$$

Geostrophic wind is an idealized model that only approximates the flow of air in high altitudes, but it provides a meaningful estimation of the real wind conditions, enabling meteorologists to determine both wind speed and direction [Lutgens et al., 2019].

2.3 Wind energy

Wind power describes the amount of wind energy flowing through an area per unit time. In fluid mechanics, the concept of measuring a flow rate carried with the moving fluid, is called flux. Wind energy is the energy in the content of moving air flow, this type of energy can be described using the kinetic energy [J] [Kalmikov, 2017].

$$E_K = \frac{1}{2} \cdot m \cdot U^2 \tag{2.4}$$

Where m is mass of air [kg] and U is the velocity of air flow [m/s].

Wind power is the rate of kinetic energy flow, we can find that by taking the derivative of the kinetic energy 2.4 with respect to time.

$$P_W = \frac{d}{dt} E_K = \frac{1}{2} \cdot \frac{dm}{dt} \cdot U^2 \tag{2.5}$$

Where $\frac{dm}{dt}$ is the change in mass divided by change in time. We know that mass is equal to density ρ [kg/m^3] times Volume V [m^3]. We can write the volume of a cylinder like the cross section areal A [m^2] times length $U \cdot dt$ [m].

$$\frac{dm}{dt} = \rho \cdot A \cdot U \tag{2.6}$$

When we substitute 2.6 into equation 2.5 we can write the equation for wind power.

$$P_W = \frac{1}{2} \cdot \rho \cdot A \cdot U^3 \tag{2.7}$$

When we observe the fundamental equation for wind power, it is important to note the cubic dependence on wind speed [Kalmikov, 2017].

To compare wind resource independent of wind turbine size it is useful to look at the wind energy flux, called wind power density. This we can find by taking wind power per unit area.

$$WPD = \frac{P_W}{A} = \frac{1}{2} \cdot \rho \cdot U^3 \tag{2.8}$$

For standard air conditions of sea-level altitude and 15°C, the air density is 1.225 [kg/m^3], which means the wind power density is proportional to the wind speed cubed [Manwell et al., 2009].

Wind speed (m/s)	Power/area (W/m^2)
0	0
5	80
10	610
15	2070
20	4900
25	9560
30	16 550

Figure 2.5: Wind speed and power density for standard air condition [Manwell et al., 2009].

If the annual average wind speed for a specific area in known, the average power density for that area could be estimated using the table in figure 2.5 [Manwell et al., 2009].

Power coefficient

When wind is captured by the rotating turbine, the velocity of the wind will be reduced. Seeking to extract more energy in the wind will result in higher velocity reduction. Therefore, it is not possible to extract 100% of the kinetic energy of the air [Betz, 2013]. The efficiency of a wind turbine is the ratio of extracted power to the total power, this is called power coefficient (C_P). The upper theoretical limit is called Betz law and is the maximum possible power coefficient [Kalmikov, 2017].

$$C_{P_{Max}} = \frac{16}{27} \sim 59\% \tag{2.9}$$

Power curve

Power curve is the relation between wind speed and generated power from the wind turbine. Every wind turbine has a characteristic performance curve that makes it possible to predict energy production. Power curve gives generated power output as a function of hub height wind speed [Manwell et al., 2009].

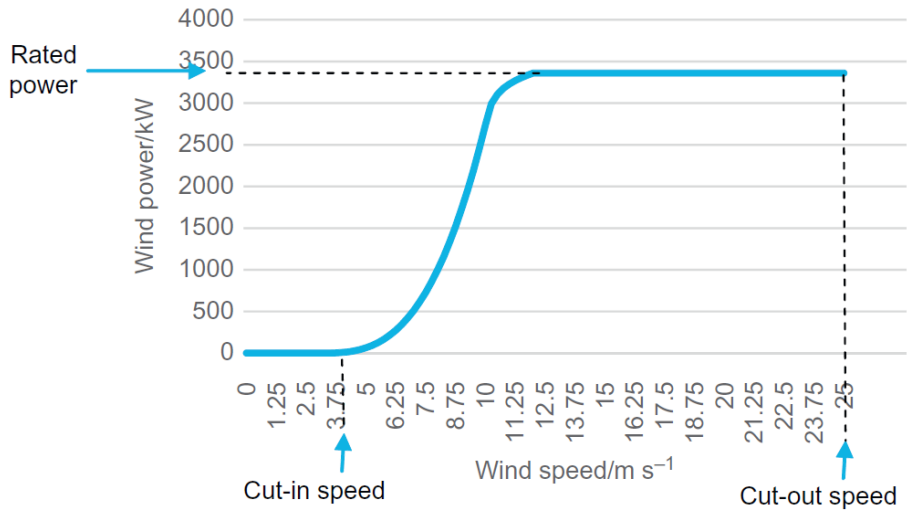

Figure 2.6: Power curve of a hypothetical wind turbine [Kalmikov, 2017]

Capacity factor

At very low wind speeds, the wind cannot create enough torque to generate power. The minimum wind speed for power generation is called cut-in speed and starts the rotation of the turbine blades. The power production is then increasing following the cubic relation to the wind speed until it reach the maximum power production of the turbine, called the rated power. Wind turbine manufacturers often place an upper limit to rotation rate on the turbine to increase lifetime of the blades. To prevent structural damage on the wind turbine, after a certain wind speed the break slows the rotation down and we have reached the cut-of speed. In figure 3.4 we can an example wind turbine where the cut-in speed is around 4 m/s, rated power of around 3400 kW which kicks in at around 12.5 m/s and a cut-of speed of 25 m/s [Kalmikov, 2017].

Capacity factor is the ratio of actual generated power over potential generated power under ideal conditions [Kalmikov, 2017].

$$C_F = \frac{E_{actual}}{E_{ideal}} \tag{2.10}$$

This means that another application of C_F is to give an fraction of the year at which the wind turbine is operating at optimal production. Typical values for economical viable projects is in the 30% mark, with really good wind resource projects reaching about 50% [Kalmikov, 2017].

Wake

For wind turbines arranged in large wind farms, there will be power production loss due to something called wake loss. Second turbine in a row will not experience the same freestream value as the first turbine. This is because the kinetic energy has been extracted from the first turbine, and the subsequent turbine will therefor experience lower kinetic energy. Thrust coefficient is the most important factor for generating wake loss, followed by wind direction, atmospheric stability and turbulence [Barthelmie and Jensen, 2010]. For calculating wake effect we can use the Park Wake Model:

$$U_W = U_F\left[1 - (1 - \sqrt{1 - c_t})\left(\frac{D}{D + 2kx}\right)^2\right] \tag{2.11}$$

where U_W is the wind speed in the wake, U_F is the free stream wind speed, c_t is the thrust coefficient, D is the rotor diameter, x is the wake distance and k is the wake decay coefficient. Recommended value for wake decay coefficient is 0.075 for onshore wind farm and 0.04-0.05 for offshore [Liu et al., 2023].

2.4 Atmospheric icing

Atmospheric icing is a global term that describes all types of ice growth due to frozen water. In general there is three form of atmospheric icing; in-cloud icing, precipitation icing and hoar frost [Fikke, 2005]. In Norway the primary cause of ice accumulation on structures is in-cloud icing mainly on mountaintops [Homola, 2011].

When supercooled water droplets comes in contact with a surface, we get whats called atmospheric icing. Type of ice is dependent of thermal balance equation of the given surface[Homola, 2011]. Thermal balance equation is described by equation 2.12 and illustrated on figure 2.7 [Fortin et al., 2006].

$$Q_F + Q_{ADH} + Q_K = Q_{SS} + Q_{EVA/SUB} + Q_{CD} + Q_{CV} + Q_{RAD} \tag{2.12}$$

Where Q_F is the latent heat of liquid freezing, Q_{ADH} is the viscous adiabatic heating from the friction from inside the boundary layer, Q_K is the kinetic heating from supercooled water droplets, Q_{SS} is the total sensible heat of the temperature change of water and ice, $Q_{EVA/SUB}$ is the heat of evaporation or sublimation of the liquid, Q_{CD} is the heat loss due to conduction into the surface, Q_{CV} is heat loss due to convective airflow over the surface, Q_{RAD} is the heat loss due to radiation from the surface [Fortin et al., 2006]. Most important term in equation 2.12 is the heat of freezing (Q_F), heat loss of convection (Q_{CV}) and evaporation/sublimation ($Q_{EVA/SUB}$) [Homola, 2011].

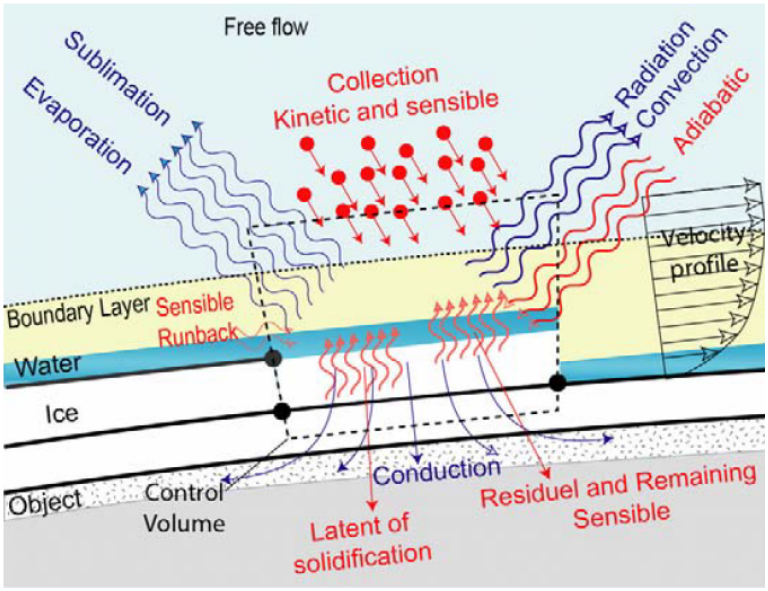

Figure 2.7: Thermal heat balance [Fortin et al., 2006]

Hoar frost, also called "ice condensation" and is when ice is created directly from water vapor. This makes the ice very light and low density, which impose low threat to structures. Therefor it is not considered as a problem for equipment [Fikke, 2005].

Further we can classify the forms of atmospheric icing as in-cloud icing (rime or glaze ice) and precipitation icing (wet snow or freezing rain) as shown in figure 2.8 [Jin, 2021].

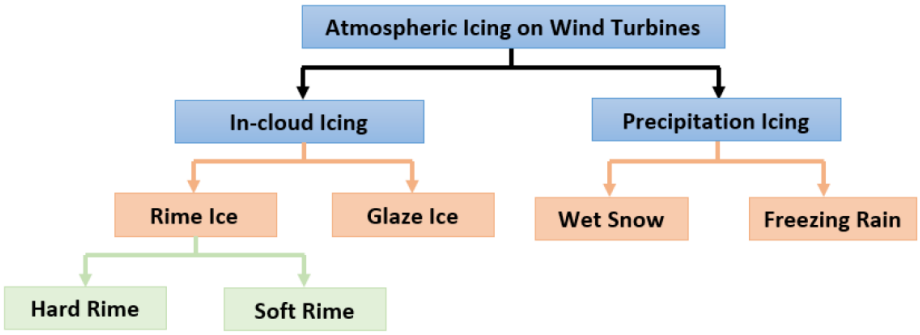

Figure 2.8: Classification of atmospheric icing on wind turbines [Jin, 2021].

2.4.1 In-cloud icing

Clouds consists of large numbers of small water droplets or crystallized ice suspended in the air, together they appear to form a solid mass. Clouds are formed by multiple rising water vapor that cools and condenses, the group of condensed water vapor forms a cloud and leads to rain and drops back to the ground [Homola, 2011].

There are several mechanisms that could lead air to rise. Orographic lifting is when prevailing winds press the air up against mountains, causing it to be driven upwards. Weather front lifting can occur when two weather fronts meet, warm air will be pressed upward by the cold air due to lower density. Heat lift occur when an air parcel is heated relative to its surrounding, increasing its buoyancy leading it to rise [Homola, 2011].

In-cloud icing is when liquid droplets below 0°C consists within clouds. This type of icing often occurs on exposed mountaintops and typically on structures like wind turbines, telecommunication towers and ski lifts. Flux of liquid water in the cloud decides the duration and intensity of the icing [Farzaneh, 2008].

Glaze

Glaze is caused by freezing rain or wet in-cloud icing and is the ice type with the highest density. Glaze can be created on any object when rain or drizzle occurs at temperature below 0°C. The rate for accretion of glaze is dependent on precipitation rate, wind speed and air temperature [Fikke et al., 2007].

Rime

Rime is the most common in-cloud ice type and will often form vanes on non-rotating objects facing the wind. Ice will evenly distribute itself along a horizontal line on the wind side, the ice load will force the string to rotate and create a cylindrical shape. We will find the most severe rime conditions on top of exposed mountains. The rate of accretion depend on object dimension, wind speed, water content in air, drop size and air temperature [Fikke et al., 2007].

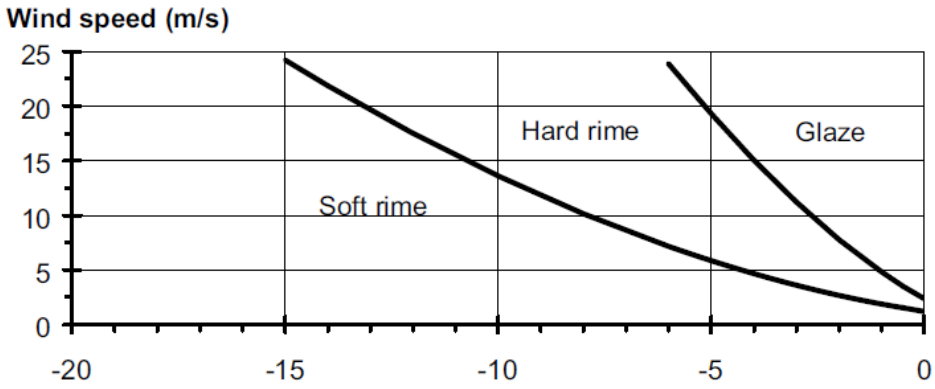

Figure 2.9: Type of ice as a function of wind speed and temperature [Fikke et al., 2007]

In figure 2.9 shows the type of ice as a function of wind speed and temperature. Here we can see that glaze is formed in temperatures close to zero, while rime is formed at colder temperature. This is consistent with fact that glaze is formed from freezing rain/wet in-cloud icing, while rime is formed from in-cloud icing. Note that [Fikke et al., 2007] divide rime into soft and hard, depending on density.

2.4.2 Precipitation icing

Depending on the temperature near the ground and a few hundred meters up, the precipitation icing can result in glaze/rime, wet snow or dry snow. Precipitation icing can occur everywhere where there is precipitation and temperature below 0°C [Farzaneh, 2008, Fikke et al., 2007].

Wet snow

Wet snow occurs when snowflake is partly melted due to travel through air temperature just above o°C, this makes the snow crystals adhere to objects and freeze when air temperature drops below freezing point. The density and strength will vary greatly, depending on degree of water in snow crystal and wind speed [Fikke et al., 2007].

Dry snow

Dry snow are low density snow that often occurs at low wind speeds. This is a precipitation icing that will not affect wind power [Farzaneh, 2008].

Dry and wet icing

The different formation processes and meteorological conditions creates different physical properties to the ice. When the water droplets freeze before the next droplet land on the given objects, we get what is called dry icing. When the water droplet don't have time to freeze before the next arrive, we say that the freezing is wet. Dry icing contains air bubbles and is called rime, while the wet icing is called glaze and is solid and clear [Fikke et al., 2007].

Type of ice	Density [kg/m^3]	Adhesion & Cohesion	General Appearance	
			Colour	Shape
Glaze	900	strong	transparent	evenly distributed/ icicles
Wet snow	300-600	weak (forming) strong (frozen)	white	evenly distributed/ eccentric
Hard rime	600-900	strong	opaque	eccentric, pointing windward
Soft rime	200-600	low to medium	white	eccentric pointing windward

Figure 2.10: Atmospheric ice properties [Fikke et al., 2007]

From the figure 2.10 we can see that [Fikke et al., 2007] have made a table of different properties of some of the different atmospheric ice types. As mentioned earlier, glaze is densest ice with evenly distributed transparent ice. Hard rime and soft rime is divided based on density and colour, we can see that hard rime has a density between 600-900 kg/m^3, while soft rime lies between 200-600

kg/m^3.

2.5 Ice accretion model

The physical model for describing ice accretion is detailed by [Makkonen, 2000] and the International Organization for Standardization (ISO12494, 2001), and is called the Makkonen model:

$$\frac{dM}{dt} = \alpha_1 \cdot \alpha_2 \cdot \alpha_3 \cdot w \cdot A \cdot U \tag{2.13}$$

Where dM/dt is the icing intensity [kg/s], w is the liquid water mass per unit volume (LWC) [kg/m^3], A is the area of the cross section of the given object normal on the wind direction [m^2], U is the wind speed [m/s]. α_1, α_2 and α_3 are coefficient that represents ice intensity-reducing processes. α_1 is the collision efficiency of the water droplet. If the droplets travel around the object instead of colliding in it, the coefficient $\alpha_1 < 1$. α_2 is the sticking efficiency, which mainly happens for wet snow. Under cooled water droplets that stick to the object, the coefficient $\alpha_2 = 1$. α_3 is the latent and kinetic energy heating of the object when water droplets freeze. This determines if the ice growth is "wet" or "dry" for rime ice and freezing precipitation. If the temperature is well below freezing point, the coefficient is considered $\alpha_3 = 1$. But if the air temperature is somewhat around freezing point, there will be some amount of water droplets that is blown away before it freezes, the coefficient $\alpha_3 < 1$. From equation 2.13 we can see that high wind speed, water content and cross section area of the object in question gives high icing intensity, and vice versa for low wind speeds, water content and cross section area [Fikke, 2005][Øyvind Byrkjedal et al., 2009a][Thompson et al., 2009].

In case of rime icing, both the sticking (α_2) and freezing (α_3) efficiency are equal 1 [Homola, 2011]. This means we can simplify equation 2.13:

$$\frac{dM}{dt} = \alpha_1 \cdot w \cdot A \cdot U \tag{2.14}$$

2.5.1 Collision efficiency and MVD

The expression for calculating the collision efficiency is [Makkonen and Stallabrass, 1987]:

$$\alpha_1 = A - 0.028 - C(B - 0.0454) \tag{2.15}$$

Where A, B and C:

$$A = 1.066K^{-0.00616}\exp(-1.103K^{-0.688}) \tag{2.16}$$

$$B = 3.641K^{-0.498}\exp(-1.497K^{-0.694}) \tag{2.17}$$

$$C = 0.00637(\phi - 100)^{0.381} \tag{2.18}$$

Where K is a non-dimensional inertia parameter (Stokes number) and ϕ is the Langmuir parameter [Makkonen and Stallabrass, 1987][Makkonen et al., 2018]:

$$K = \frac{\rho_w U_F d^2}{9\mu D} \tag{2.19}$$

$$\phi = \frac{Re^2}{K} \tag{2.20}$$

Where Re is the droplet Reynolds number [Makkonen et al., 2018]:

$$Re = \frac{\rho_a d U_F}{\mu} \tag{2.21}$$

Where ρ_w is the water density [kg/m^3], ρ_a is the air density [kg/m^3], U_F is the free stream velocity [m/s], d is the water droplet diameter [m], D is the cylinder diameter [m], μ is the absolute viscosity of air [kg/m s] [Makkonen and Stallabrass, 1987].

The collision efficiency mainly depends on air flow speed and relative size of the collecting object and water droplets. This means that each droplet has its unique collision efficiency. However, we can compute the average collision efficiency for a droplet spectrum by using the median volume diameter (MVD) which assumes uniform distribution of droplet diameter [Finstad et al., 1988].

We first need to assume that cloud water follow a generalized gamma distribution [Thompson et al., 2009]:

$$N(D) = N_0 D^{\beta} e^{-\lambda D} \tag{2.22}$$

Number of droplets in equation 2.22 is function for a specified diameter D. N_0 is the intercept parameter, λ is the distribution slope and β is the shape parameter with specified droplet number N_c indicating droplets per cm^3 [Thompson et al., 2009].

$$\beta = min(\frac{1000}{N_c} + 2, 15) \tag{2.23}$$

We find the distribution slope (λ) from integrating equation 2.22 over all diameters with the mass of spherical water drops [Thompson et al., 2009]:

$$\lambda = \left[\frac{\pi}{6}\rho_w \frac{\Gamma(4+\beta)}{\Gamma(1+\beta)}\left(\frac{N_c}{LWC}\right)\right]^{1/3} \tag{2.24}$$

To find MVD of cloud droplets we can use the result of β and λ [Thompson et al., 2009]:

$$MVD = \frac{3.672+\beta}{\lambda} \tag{2.25}$$

The MVD approximation gives good results at the range $0.07 < \alpha_1 < 0.63$ [Makkonen and Stallabrass, 1987].

We can then insert our result for MVD instead of d in equation 2.19, 2.21 and get:

$$K_{MVD} = \frac{\rho_w U_F MVD^2}{2\mu D} \tag{2.26}$$

$$Re_{MVD} = \frac{\rho_a U_F MVD}{\mu} \tag{2.27}$$

The collection efficiency is always less than 1 since particles will be deflected by the air stream and miss the surface. As shown in figure 2.11, large water droplets have higher collision efficiency than smaller droplets. Smaller object will have smaller streamline radius in front when air flows around the object, thus making it more efficient in collecting droplets, since it will be more difficult for water droplets to follow the streamlines. Meaning that two different size object can have vastly different ice accretion under the same conditions [Homola, 2011].

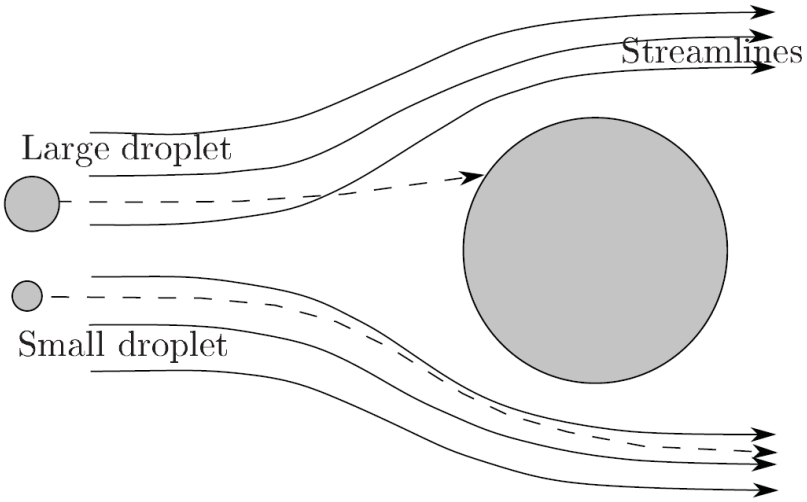

Figure 2.11: Collision efficiency α_1 for large and small droplets [Homola, 2011].

2.6 Numerical weather prediction

Numerical weather predictions (NWP) models has become a central components of weather prediction. The concept of NWP is to solve a set of differential equations that describes the basic conservation laws, including conservation of mass, momentum, energy and water vapor. Since we want to predict the future state of the atmosphere, we would need to integrate them forward. The current atmospheric state will then become the initial state and the integration will provide the future state, making it an initial value problem [Pu and Kalnay, 2018].

There is seven equations with seven unknowns that controls the evolution of the atmosphere. Equation 2.28 is the conservation of momentum and contains three equation for the three velocity components,

$$\frac{d\vec{V}}{dt} = -\alpha\vec{\nabla}p - \vec{\nabla}\Phi + \vec{F} - 2\Omega \times \vec{V} \tag{2.28}$$

$\vec{V} = (u, v, w)$ represents the three velocity components of air [m/s], t is time [s], α is specific volume [m^3/kg], p is pressure [Pa], $\vec{F}$ is friction force [m/s] and Φ is geopotential height [m^2/s^2] . Equation 2.29 is the conservation of mass where ρ is density [kg/m^3] [Pu and Kalnay, 2018],

$$\frac{\partial \rho}{\partial t} = -\vec{\nabla} \cdot (\rho \vec{V}) \tag{2.29}$$

Equation 2.30 describes the ideal gas law where R is the gas constant [J/mol·K] and T is temperature [K], and equation 2.31 refers to the conservation of energy, where Q is heating [J/kg·s] [Pu and Kalnay, 2018],

$$p\alpha = RT \tag{2.30}$$

$$Q = C_p \frac{dT}{dt} - \alpha \frac{dp}{dt} \tag{2.31}$$

where C_p is the specific heat capacity at constant pressure [J/kg·K], and the last equation 2.32 details the conservation of water mass [Pu and Kalnay, 2018],

$$\frac{\partial \rho q}{\partial t} = -\vec{\nabla} \cdot (\rho \vec{V} q) + \rho(E - C) \tag{2.32}$$

here q is water vapor mixing ratio, E and C is the evaporation and condensation, respectively [Pu and Kalnay, 2018].

For a NWP models to work it is necessary to define boundary conditions. For a global atmospheric model top and bottom boundary conditions is needed, where as for a regional model we would need a lateral boundary in addition to top and bottom. The upper boundary is usually at an altitude above meteorological interest, commonly in the stratosphere or above. The bottom boundary is very complicated, as the surface vary greatly. Therefore they are commonly parameterized as thermal diffusion surface models, land surface, ocean surface or surface drag schemes. Lateral boundaries found in regional models, are preferred for weather prediction over global models to reduce model errors through higher horizontal resolution. Regional models are "nested" into coarser models, where the coarser model continuously updates the boundary of the "nested"- regional model [Pu and Kalnay, 2018].

Two major parts are consisted inside an NWP model, "dynamics" indicate the resolved processes and "physics", the processes that must be parameterized. All the physical processes interact with the dynamics and each other, which makes NWP a numerical complicated and computationally expensive. Figure 2.12 show how NWP resolve physical and dynamical processes [Pu and Kalnay, 2018].

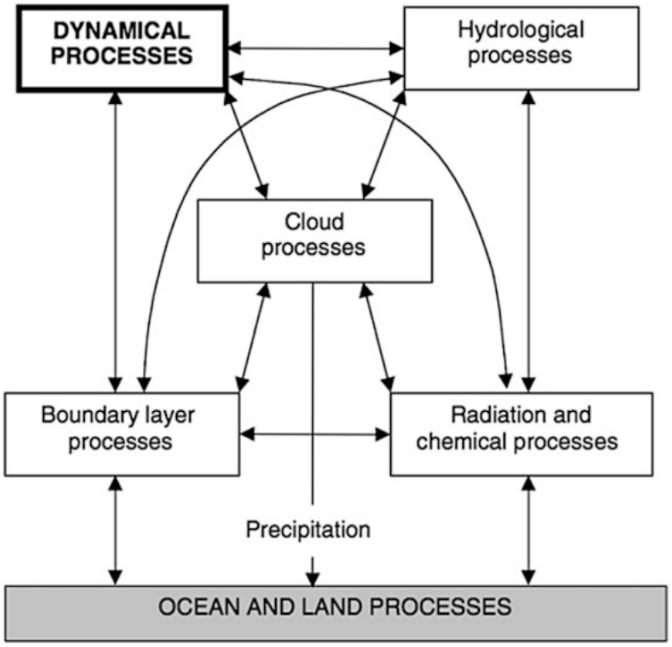

Figure 2.12: Physical and dynamical processes in the atmosphere and their interactions [Pu and Kalnay, 2018]

However, as the model resolution increases so is the data volume expected to grow to over 100 TB per day before 2030, limiting the already limited high performance computers (HPC) capacity [Brotzge et al., 2023].

3 Method

3.1 Site of Davvi wind farm

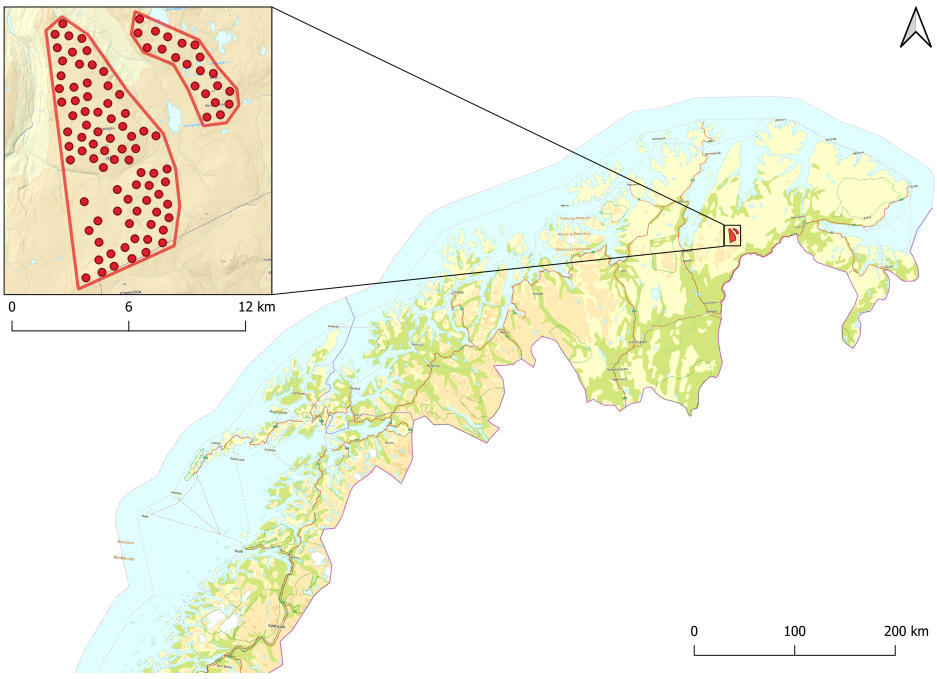

Figure 3.1: Davvi wind farm location. Map created in QGIS with Kartverket N50 Topo map.

The planned area of Davvi wind farm is in Lebesby, county of Finnmark, Norway. The entire area is owned by "Finnmarkseiendommene (FeFo)". Here they plan to build a wind farm with an installed effect of 800 MW in the mountainous area near Vuonjalrášša. The height of the planned area varies from 500-800 meter above sea level [Grenselandet AS, 2022].

The illustration in figure 3.1, show the location and scale of the planned area of Davvi wind farm. The location has a latitude and longitude 70^{o}N and 26^{o}E, and the nearest neighbouring town is Kunes, 24km north. There are two large fjords in the area, "Porsangerfjorden" to the north-west and "Laksefjorden" to the north-east which could channel moist maritime air from the north over the planned area of Davvi.

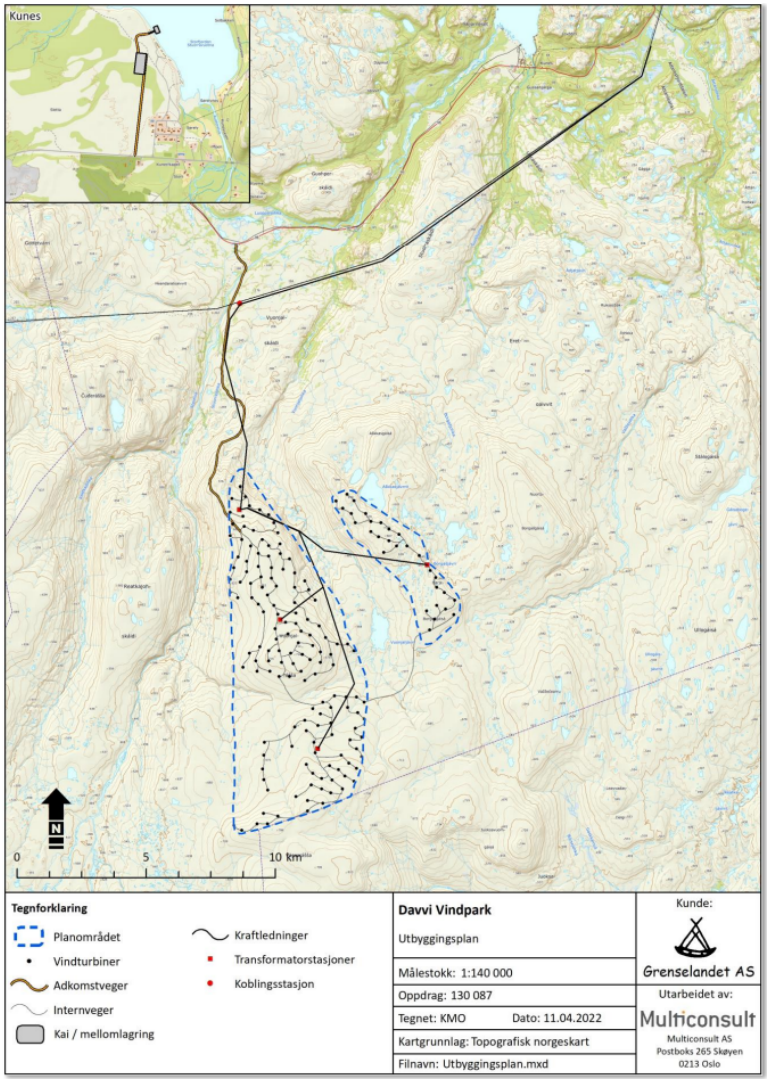

Figure 3.2: Planned Area of Davvi wind farm. [Grenselandet AS, 2022]

The figure 3.2 shows the planned area with the blue dashed line indicating the two main areas where the turbine would be placed. Black dots indicate each wind turbine and thin black line indicate internal roads while the orange thick line show access roads. The map shows a big open hilly area with little in the way of influencing the wind [Grenselandet AS, 2022]. The turbine placements in this figure are outdated, 3.3 show updated turbine locations after conversation with people currently working on the Davvi-project. To get an overview of the varying conditions, we have selected five turbine location marked with a yellow dot.

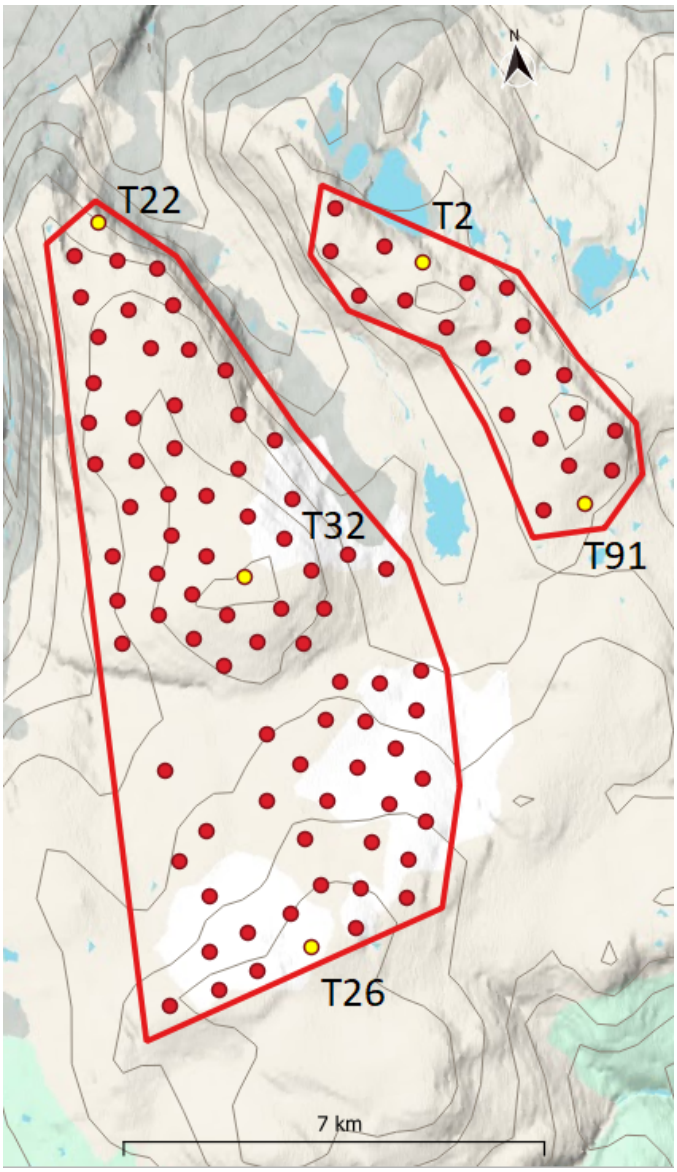

Figure 3.3: Davvi wind farm with turbine T2, T22, T26, T32 and T91 marked.

We have picked the highest location (T26), lowest (T22) and NEWA point (T32) in area west. Highest location (T2) and lowest location (T91) in area east.

3.1.1 Wind turbine

The planned wind turbine type for Davvi wind farm is Vestas V164-8.0, with 8 MW nominal power, hub height of 200m and rotor diameter of 164m. Planned

size of the wind park is 800 MW, which fits 100 of such turbines. Figure 3.4 show the power curve [kW] and thrust coefficient of Vestas V164-8.0.

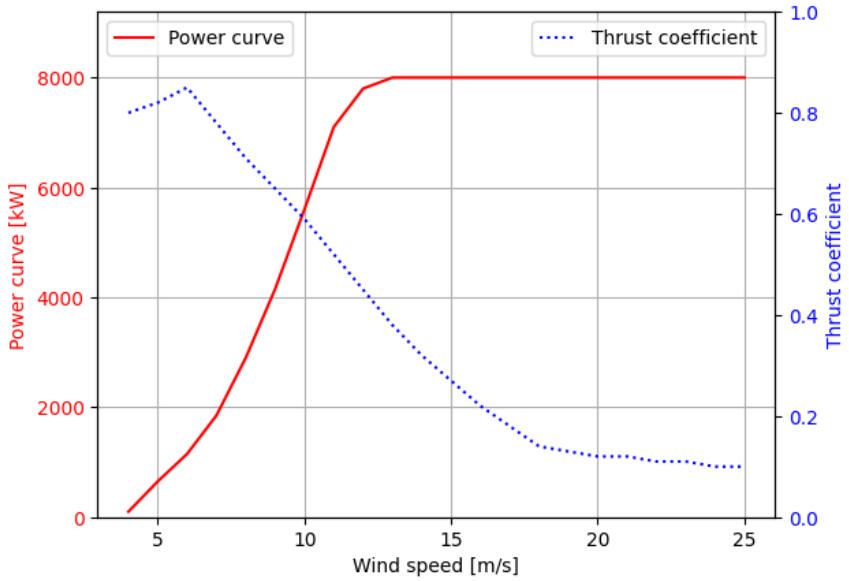

Figure 3.4: Plot showing power curve (red) and thrust coefficient (dotted blue) over wind speed.

3.2 Weather Research and Forecasting model

This thesis utilizes the Weather Research and Forecasting (WRF) model, developed by National Centre for Atmospheric Research (NCAR). WRF is a mesoscale model designed for both research and numerical weather prediction (NWP) which supports multiple physics options that can be combined together. Mesoscale modelling have found multiple application in the wind energy field. Mainly to assess long term wind variability, short term wind energy production forecasting or generating maps of mean wind resources over large areas [Carvalho et al., 2012][Skamarock et al., 2021].

3.2.1 WRF Preprocess System

WRF Preprocessing System (WPS) is a program set to prepare input for simulation, it consist of three programs, each performing one stage of the preparation; geogrid defines model domains and interpolates static geographical data to the grids; ungrib extracts meteorological fields from GRIB-files; and metgrid horizontally interpolates the meteorological fields extracted by ungrib to the model

grids already defined by geogrid. Each of the programs read of a namelist.wps file which defines parameters used by the WPS program, illustrated by figure 3.5 [Wang et al., 2022].

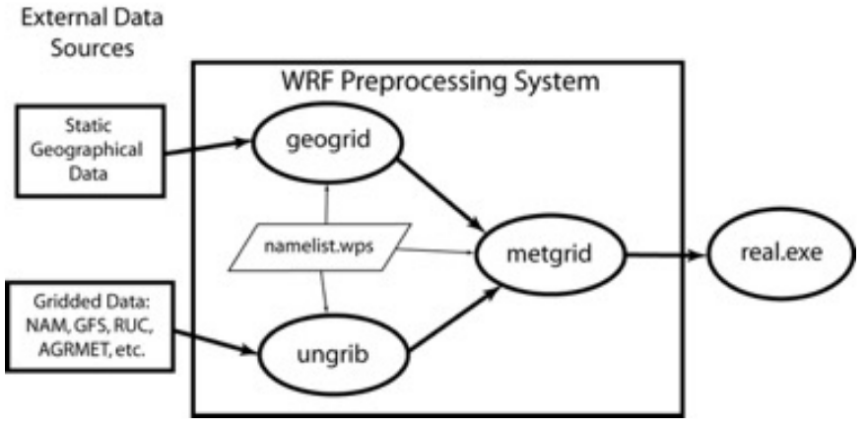

Figure 3.5: Data flow between programs in WPS. [Wang et al., 2022]

Geogrid

Geogrids main task is to define the simulation domains and interpolate terrestrial data to the model grids. Here it will compute latitude and longitude and map scale factors for every grid point, along with interpolating soil categories, land use categories, terrain height, annual mean deep soil temperature, vegetation fraction, albedo, snow albedo and slope category to the model grid. The output is written in the WRF I/O API format, meaning it could be made to write its output in netCDF for easy visualization using other software like ncview or NCL [Wang et al., 2023].

Ungrib

The ungrib program reads GRIB files, "ungribs" and writes the data in a simple format called intermediate format. GRIB files contains time-varying meteorological data, and will typically contain more files than needed to run WRF. The program therefore uses tables of codes, called Vtables (short for "variable tables"), to define which fields to extract from the GRIB file [Wang et al., 2023].

Metgrid

The metgrid program horizontally interpolate the intermediate-format extracted by the ungrib program onto the domains defined in the geogrid program. The dates that will be interpolated are defined in the namelist.wps file and must be specified individually for each domain. METGRID.TBL file provides control over how each meteorological field is interpolated. Like the geogrid program, metgrid output is written in the WRF I/O API format and can therefore be made to write its output in netCDF for easy visualization [Wang et al., 2023].

3.2.2 The Advanced Research WRF model

The Advaned Research WRF model (ARW) is a configuration of the WRF system with a dynamics solver together with other components that produce simulations. ARW also includes physical schemes, numerics/dynamics options, initialization routines and data assimilation packages (WRFDA). In addition to weather prediction, ARW also supports atmospheric chemistry (WRF-Chem), hydrological modelling (WRF-Hydro) and wildfire modelling (WRF-Fire) [Skamarock et al., 2021].

In this thesis we have used Thompson microphysics scheme [Thompson et al., 2008], Mellor-Yamada-Nakanishi-Niino (MYNN) 2.5 level planetary boundary scheme [Nakanishi and Niino, 2009][Olson et al., 2019], the rapid radiation tranfer model for global models (RRTMG) scheme for short/long wave radiation [Iacono et al., 2008], Kain-Fritch cumulus scheme [Kain, 2004], Noah multiparameterization land surface scheme (Noah-MP) [Niu et al., 2011][Yang et al., 2011], Revised MM5 surface layer scheme [Jiménez et al., 2012] and the urban canopy model [Chen et al., 2011].

3.2.3 ERA5

ERA5 is an atmospheric reanalysis produced by the European Center for Medium-Range Weather Forecast (ECMWF). It is the fifth-generation following FGGE, ERA-15, ERA-40 and ERA-Interim. Reanalysis combines observation with model data from all over the globe into a complete global and consistent dataset. ERA5 provides a hourly estimates of surface, atmospheric and oceanic parameter from 1940 to present. The ERA5 data is distributed in GRIB-files that is regridded to latitude and longitude grid with spatial resolution of 0.25^o [Hersbach et al., 2023].

3.2.4 Domain

In this thesis, the model is configured with three one-way nested domains. Nested simulation means that the coarser domain contains one or more finer resolution domain within, one-way means the the information only goes one way, from the coarser domain to the finer domain. The outermost domain D01 has a horizontal resolution of 9 km, D02 3 km and D03 1 km, making it a 1:3:3 domain ratio. The domains are configured with 51 vertical levels up to a boundary at 50 hPa [Wang et al., 2023]. Figure 3.6 is an example of how we can visualize the domains and terrain height. The white boxes represents D02 and D03 inside D01. The green outlay show the location of the planned area of Davvi wind farm, note that the dimensions are not totally correct, this is only to illustrate the position of the park in relation to the domain edges.

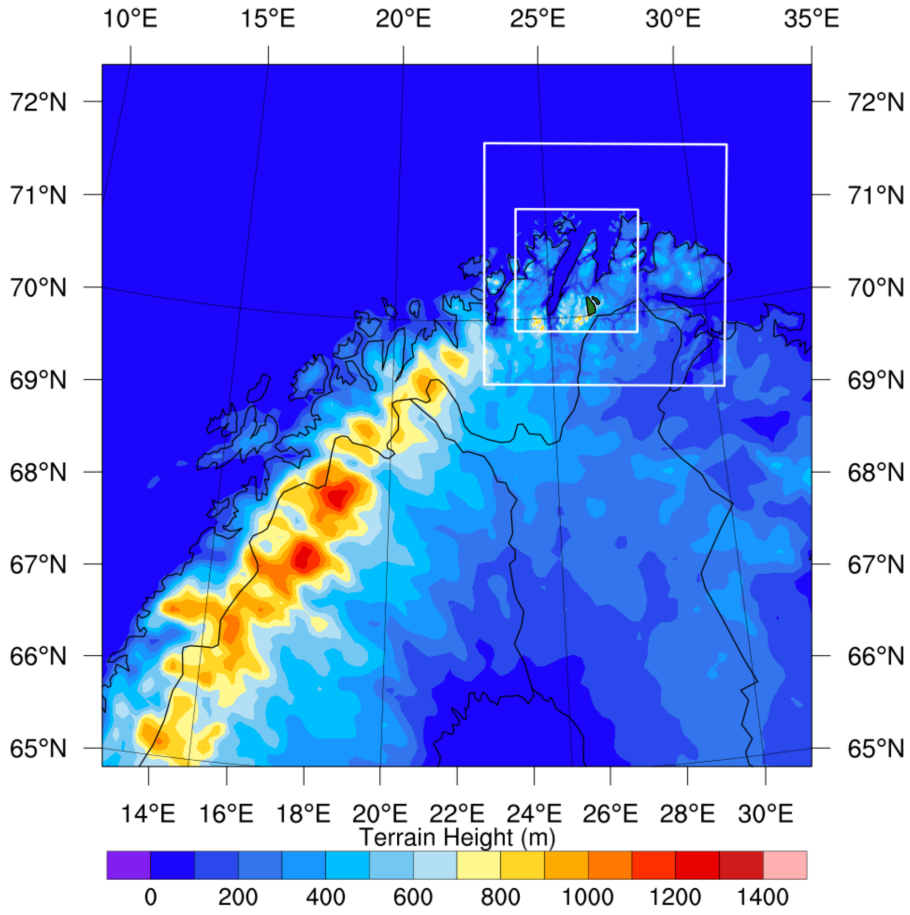

Figure 3.6: Terrain height for all domains. Green outlay show the area of Davvi wind farm

3.2.5 Wind turbine scheme

We have utilized a wind turbine scheme called Fitch-scheme that lets us simulate power production of our wind farm. The kinetic energy extracted is based on the thrust coefficient of the wind turbine, and the turbulence kinetic energy (TKE) is generated as a function of wind speed. [Fitch et al., 2012]

To use the Fitch-scheme we have to set the domain dependent "windfarm_opt" to 1. This tells the WRF to look for a file called "windturbines.txt" which contains the latitude and longitude of every turbine and a turbine type number. The latitude and longitude gets converted into i,j index in the grids. Turbine type number tells WRF to look for a file containing turbine specification, if we have typed turbine type 1, it will look for a file called "wind-turbine-1.tbl". This file will contain a line with hub-height, rotor diameter, standing thrust coefficient and nominal power, as well as power curve and thrust coefficient pairing [Fitch et al., 2012].

In this thesis we have only enabled "windfarm_opt' for the innermost domain. This is due to simulation problems where the model would crash when the option was enabled for domain 1 and 2. We looked extensively for a solution, but found that the only option was to exclude turbines for the two outermost domains. We do not know the reason or a solution for the problem. Contents of windturbines.txt and wind-turbine-1.tbl, can be found in Appendix A and Appendix B respectively.

In order to study the impact of the turbines on our icing and wind results, we have ran a simulation for 2017 without including the turbines. To measure how much the wind turbine scheme affected our results, we took the difference for annual mean wind speed, annual mean temperature, icing hours above 10 g/h and annual mean ice rate.

3.2.6 Post process

After running 365 individual WRF-simulations with 12 hour spin-up time we needed to remove the spin-up time, extract wanted variables. After we used NCO's "ncrcat" function, we are left with 365 files with 24-hours each. The files are still to big to work with so we want to extract data from each turbine location at hub height. For this we used Python code, extracted data for location and height and stored into a new nc-file for each day. By doing this we shrunk the file size down to 693 MB from 1.2 TB for domain 3 and 620 MB from 584 GB for domain 2. We will then have small files that contain just what we want in terms of location and variables, making it more efficient to analyse.

3.2.7 Variables

The variables we extracted from the WRF simulation are listed in table 3.1, with their description and units. Variables with multiple units has an option to choose between the different option, with the first in the list being the standard.

Variable	Description	Units
height_agl	Model height for Mass Grid (AGL)	m, km, dm, ft, mi
lat,lon	Latitude, Longitude	Degrees (decimal)
tk	Temperature	K
U,V	U and V Components of Wind	m/s, km/h, mi/h, kt, ft/s
rh	Relative humidity	%
pres	Full Model Pressure	Pa, hPa, mb, torr, mmhg, atm
QCLOUD	Cloud water mixing ratio	kg/kg
POWER	Power production	W

Table 3.1: Variables, description and units for parameters extracted from WRF.

3.3 New European Wind Atlas

New European Wind Atlas (NEWA) is a wind atlas for several regions in the world to help inform wind energy installations. Mesoscale simulation was ran with WRF model 3.8.1 with Mellor-Yamada-Nakanishi-Niino (MYNN) planetary boundary layer scheme [Dörenkämper et al., 2020]. Additionally, ice accretion was modelled by utilizing the iceBlade model, as clarified by communication with one of the contributors of the model.

Simulation use three nested domains with 3 km grid resolution in the innermost domain and a 1:3 ratio between inner and outer domains. This means that the grid resolution had 27 km : 9 km : 3 km grid resolution for domain 1, domain 2 and domain 3 respectively. Area of simulation was divided into 10 independently computational domains, these 10 domains are the innermost domains who all share the same outermost domain [Dörenkämper et al., 2020]

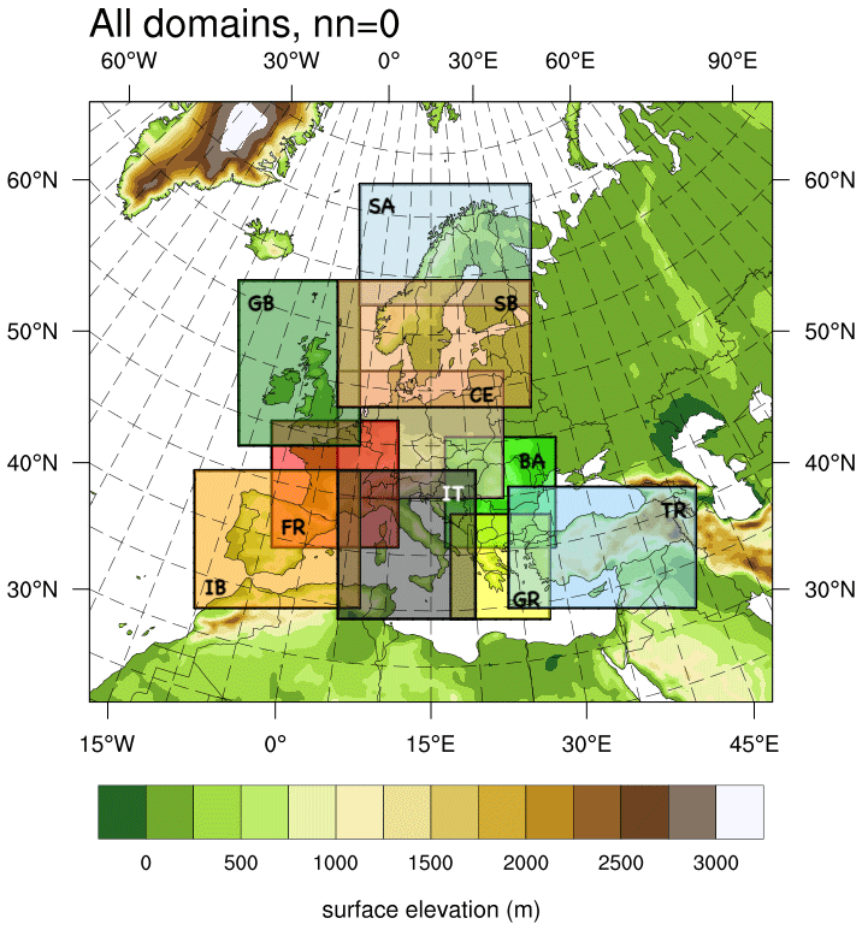

Figure 3.7: 10 innermost WRF model domains [Dörenkämper et al., 2020]

The domains in figure 3.7 needed to cover the areas of interest, this meant that the all European Union members, Norway, Switzerland, the Balkans and Turkey needed to be covered by the innermost domain. Additionally 100 km of offshore coast and the whole North and Balkan sea. Domains also needed to be large enough so that each country would fit inside one domain, Norway, Sweden and Finland being the exception. 30-year mesoscale database was created by running this WRF model simulations between August 2018 and March 2019 [Dörenkämper et al., 2020].

Microscale is generated with a program called Wind Atlas Analysis and Application Program (WAsP). The program takes the WRF output from the mesoscale simulation and downscale it using something they calls WRF-WAsP methodology. This is a methodology where they extrapolate the horizontal and vertical wind data from a nearby measurement point in order to estimate the wind at a

given point. Microscale atlas is then created as a high-resolution atlas with the statistical wind resources in 50-by-50 m grid [Dörenkämper et al., 2020].

IceBlade

The iceBlade model is a ice accretion model that was developed to simulate ice accretion on a wind turbine blade during in-cloud icing. The model uses the Makkonen model described in equation 2.13 and includes term for sublimation, wind erosion and ice shedding. The model also incorporates the relative velocity of the rotational speed of the rotor blade, which is much higher at the blade tip than at the turbine hub. The iceBlade model assumes the blade as a cylinder with the diameter as twice the leading edge radius of the blade, also it only accounts for liquid phase cloud particle, meaning wet snow will not be included in the model [Davis, 2014].

The ice accretion from NEWA is stored as ice load [kg], so in order to convert it to ice rate, we need to take the time derivative. Since the time resolution for NEWA is 30 min, we calculate the difference for two time steps and convert it to rate of mass in gram per hour. Lastly we take the hourly mean, meaning we get ice rate on the form g/h.

3.4 Ice accretion calculation

With the dry ice assumption, we use 2.14 for calculating ice accretion on a standard reference cylinder. We will calculate the collision efficiency (α_1) with equation 2.15 and MVD with equation 2.25. Droplet concentration is typically set according to environment, where $N_c = 100$ cm^{-3} for clean and maritime air and $N_c = 250$ cm^{-3} for polluted and continental air [Nygaard et al., 2011]. In this thesis we will use $N_c = 100$ cm^{-3} due to the close proximity to coastal areas.

3.4.1 Icing period

An active icing period is defined as the moment ice growth rate exceeds the threshold. The period starts when the icing rate exceeds 10 g/h. Passive icing period is defined as when the ice mass exceeds a threshold of 10g, period is ended when the ice mass is falls below the threshold due to melting or shedding. Three common thresholds are described; start of icing: 10g, light icing: 50g and moderate icing: 250g. Moderate icing is the threshold for when geometric ice accretion starts to form and we get "two-horn geometry" where aerodynamically

friction is high [Hämäläinen and Niemelä, 2017]. Threshold for temporary stop of turbine was set at 500g [Turkia et al., 2013]. Ice melting is implemented by decreasing ice load when temperature exceeds a certain threshold. Ice shedding is simplified by stating that if temperature is above 0.5 ^{o}C for 6 consecutive hours, all ice mass lost [Hämäläinen and Niemelä, 2017].

Icing map

When running a model which calculate the ice rate for every grid point for each hour, we can calculate how many hours a given location has an ice intensity over the given recommended amount of 10 g/h. Topography is often smoothed out by the model, therefore [Øyvind Byrkjedal et al., 2009a] have utilized height correction using N50 height data. This means that the data from WRF is extracted for heights corresponding to 80 meters asl for N50 height data and not height from the model itself. From this they have made an icing map which shows the ice frequency for Norway [Øyvind Byrkjedal et al., 2009a].

There are multiple insecurities when it comes to modelling the icing map. [Øyvind Byrkjedal et al., 2009a] explains that earlier validations show that icing in areas ranging between 0 and 500 above sea level could be overestimated. Areas on the inland could also experience an overestimation of icing due the fact that coastal areas have larger water droplets, less amounts of cloud-ice and that the model underestimate the loss of water over forests and high peaks and therefor overestimate the water available for freezing [Øyvind Byrkjedal et al., 2009a].

In the calculation it is used $N_c = 100$ droplets per cm^{-3}, this is a more accurate estimation of coastal areas and is considered large water droplets. Areas further away from the coast will typically have a higher amounts of droplets per cm^{-3}, which means the droplets will be smaller in diameter. Large water droplets will give a higher α_1 collision efficiency and increase icing [Øyvind Byrkjedal et al., 2009a].

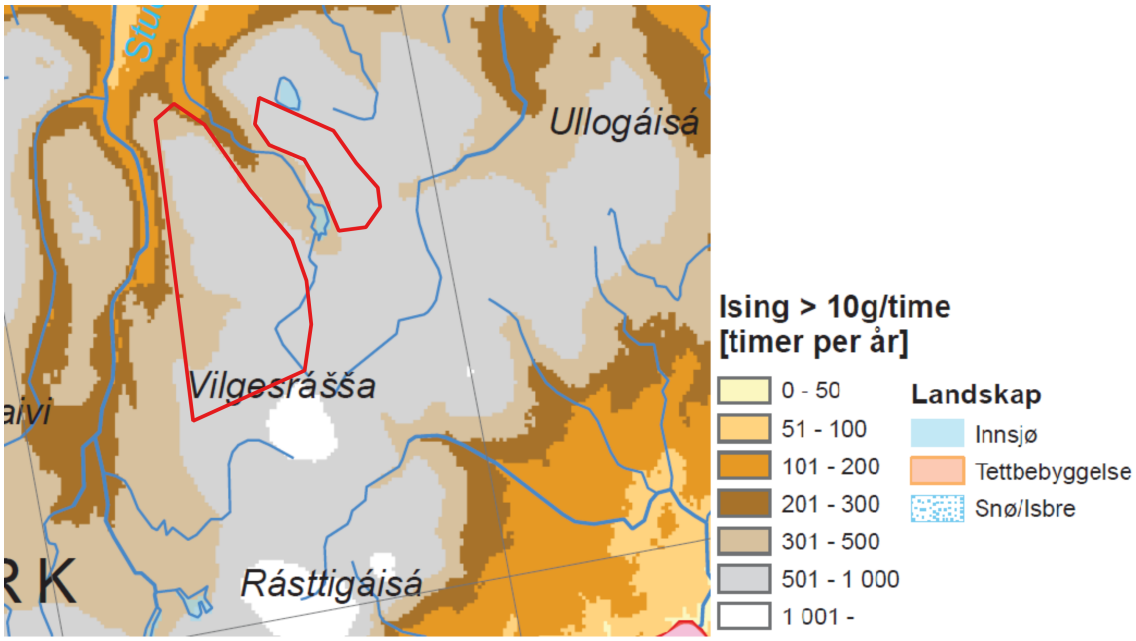

Figure 3.8: Icing map. Red outline show the planned area of Davvi wind farm [Øyvind Byrkjedal et al., 2009b].

From the icing map in figure 3.8 we can see a large section of the area are indicating strong icing with 501-1000 hours of icing ($> 10\ g/h$) during a year. We can see a smaller area south of the planned area with greater icing, this could indicate that the area surrounding are very susceptible to icing.

3.5 Model validation

3.5.1 Banak weather data

For model validation we have collected weather data from Banak weather station located on Banak Airport, Lakselv. We have used 'Norwegian Center for Climate Services (NCCS) - Seklima.met.no' and collected daily mean wind speed and temperature values for the year 2017. We then intend to collect data from our simulation for the same location and use statistical metrics to validate how well the model simulated the yearly wind speed and temperature. Banak weather station is located at 5m height, this is lower than the lowest layer in the model, so we have used 'T2' and 'uvmet10' variable from WRF. 'T2' gives a temperature at 2m height, and 'uvmet10' gives u and v components at 10 meter height. Comparing model to weather data will give us an indication on model performance. Figure 3.9 show the location of Banak weather station,

it is located about 50 km west of Davvi wind farm. The measuring station is located about 5 meter above sea level, on an airport deep in a fjord with high mountains to the west and east.

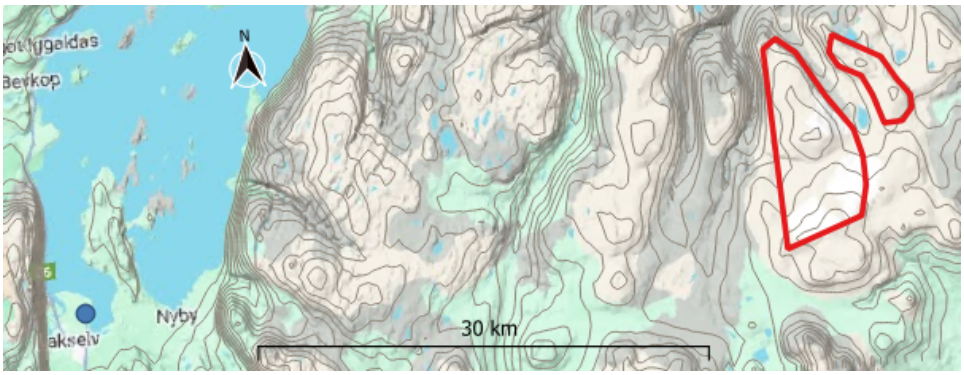

Figure 3.9: Davvi wind farm indicated by red outline and Banak weather station indicated by blue dot

3.5.2 Statistics

For evaluating the performance of the model we will use different statistical metrics. We will use mean ($\bar{x}$), standard deviation (σ), bias (d), Root-Mean Square Error ($RMSE$) and correlation coefficient (ρ). For $i = 1, 2.., N$ points of data, the mean and standard deviation of x_i is described as,

$$\bar{x} = \frac{1}{N}\sum_{i=1}^{N} x_i \tag{3.1}$$

$$\sigma = \sqrt{\frac{1}{N}\sum_{i=1}^{N}(x_i - \bar{x})^2} \tag{3.2}$$

where σ is the measure of deviation of values in the data [Solbakken et al., 2021]. $RMSE$ is a measure of the deviation between observed values and simulated values and can be describes as,

$$RMSE = \sqrt{\frac{1}{N}\sum_{i=1}^{N}(\Theta_i)^2} \tag{3.3}$$

where $\Theta_i = x_i - y_i$ represents the deviation in each value in the dataset. For measuring the tendency in the data we evaluate the bias,

$$d = \frac{1}{N}\sum_{i=1}^{N}\Theta_i \tag{3.4}$$

if the value is positive it indicate an overestimation of the simulated values, and an underestimation for negative values [Carvalho et al., 2012].

Centered root-mean-square error ($CRMSE$) calculates the difference between observed and simulated values without the tendency (d) [Solbakken et al., 2021].

$$CRMSE = \sqrt{\frac{1}{N}\sum_{i=1}^{N}[(x_i - \bar{x}) - (y_i - \bar{y})]^2} \tag{3.5}$$

To indicate a linear relationship between the simulated and observed values, we use a correlation coefficient,

$$\rho = \frac{\frac{1}{N}\sum_{i=1}^{N}(x_i - \bar{x})(y_i - \bar{y})}{\sigma_x \sigma_y} \tag{3.6}$$

where σ_x,σ_y is the standard deviation of the datasets. For ρ equals 1, the pattern of the two dataset is exactly identical, if ρ equal 0, there is no correlation [Solbakken et al., 2021].

Taylor diagram

Taylor diagram is a diagram showing a statistical summary of how well a model pattern match by use of correlation, centered root-mean-square error (*CRMSE*) and ratio of variance. This is a tool that is especially useful in evaluating complex models, such as geophysical models [Taylor, 2001].

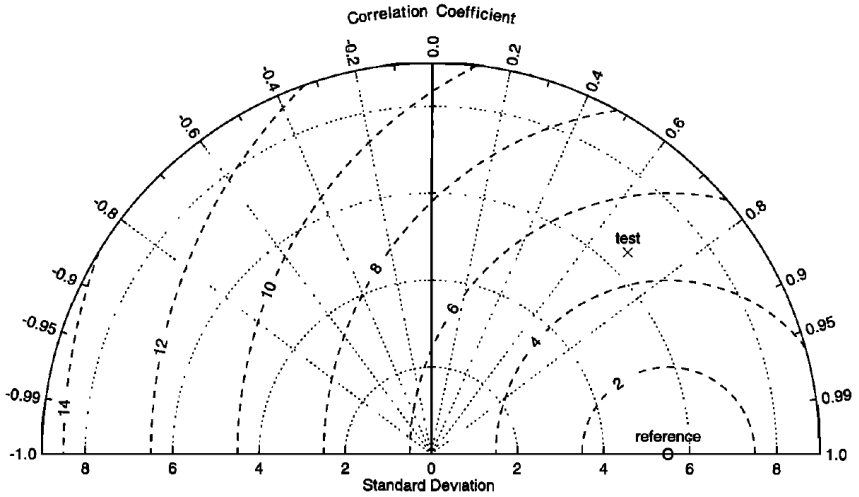

Figure 3.10: Example of a Taylor diagram [Taylor, 2001].

The example Taylor diagram shown in figure 3.10 shows a statistical pattern. The radial shows the standard deviation, the azimuth shows the correlation and the centered root-mean-square error is shown by the distance between the reference and the model.

3.5.3 Wind rose

Wind rose is a circular histogram showing the frequency of wind direction for a specific location. In figure 3.11 we see an example wind rose, where the bars radius indicate the amount of registered wind from that given direction, the section of the bar indicate the wind direction in degrees, 0^o being North, 90^o East, 180^o South and 270^o West. Coloring or shading of the bar show wind speed. This is a good way of showing wind direction and wind speed tendency over a period of time for specific location.

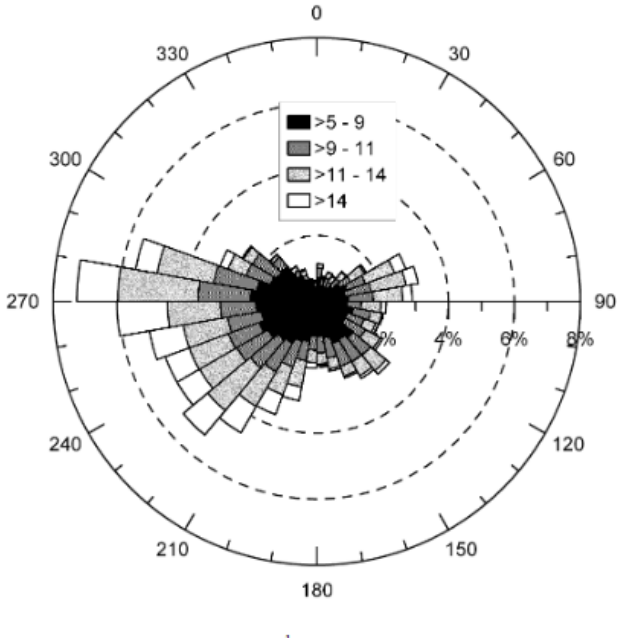

Figure 3.11: Example wind rose showing wind direction distribution and wind speed by shading [Barthelmie and Jensen, 2010].

3.5.4 Production loss

IEA Task 19 made an icing climate site classification which show an estimated reduced annual production based on yearly icing amount. In figure 3.12 we can see the table which connects meteorological icing and reduced production. Meteorological icing means icing where the meteorological conditions are met for ice accretion (temperature, wind speed, liquid water content), while instrumental icing is icing which are visible/present on a structure [Davis et al., 2018]. We will focus on meteorological icing in this thesis.

IEA Ice Class	Meteorological Icing	Instrumental Icing	Reduced Production
	% of year	% of year	% of annual production
5	>10	>20	> 20
4	5-10	10-30	10-25
3	3-5	6-15	3-12
2	0.5-3	1-9	0.5-5
1	0-0.5	<1.5	0 - 0.5

Figure 3.12: IEA Icing Climate site classification [Davis et al., 2018]

Power production of a wind turbine is proportional to the wind speed that causes the blades to rotate. [Lamraoui et al., 2014] explains that the blade near the rotation center produce around 4% of the production, while the last 20% produce the most with around 36% of the production. They approximate that the last 60% of the blade produce around 86% of the production. This is problematic since the tip of the blade experience the highest velocities and are where the icing is most likely to form.

[Lamraoui et al., 2014] conclude that the maximum power loss is when freezing fraction is equal 0.88, which correspond to a "double horn ice shape" formation which creates the most aerodynamically friction. They then calculate that this freezing fraction for different liquid water contents and temperatures, especially LWC = 0.2 g/m^3 which has a maximum power loss at T = -12 ^{o}C.

Power curve in figure 3.13 shows the estimated power output under normal and icing conditions, where LWC = 0.2 g/m^3 and T = -12 ^{o}C in red and T = -13,5 ^{o}C in black. Note that the black line has a higher production than the red line even though the temperature is lower. [Homola et al., 2011] used model based computational fluid dynamics and compared it to observations on Nygårdsfjellet Wind farm which is installed in Narvik, Norway. During simulation parameter LWC = 0.22 g/m^3 and T = -10 ^{o}C was used. Figure 3.14 show that the power loss for ice conditions was 27% in control region two.

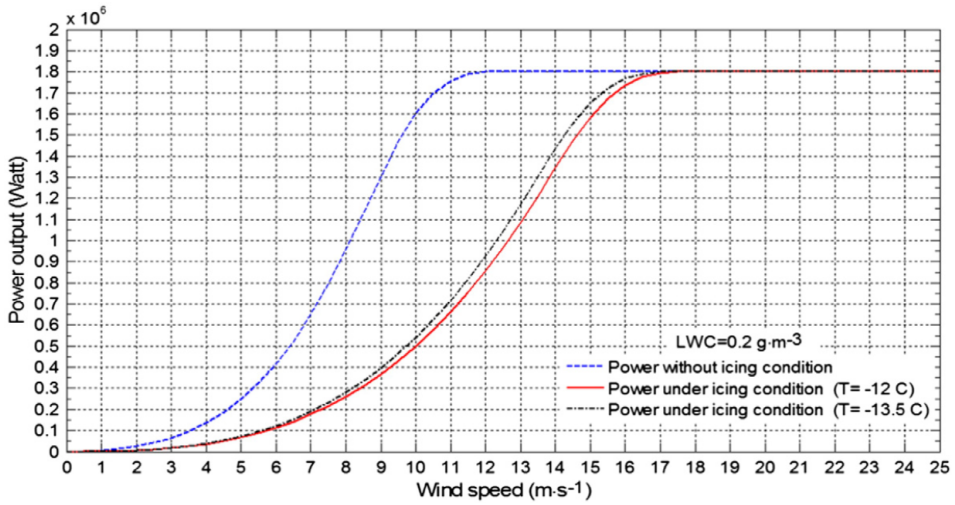

Figure 3.13: Power Curve with icing conditions. [Lamraoui et al., 2014]

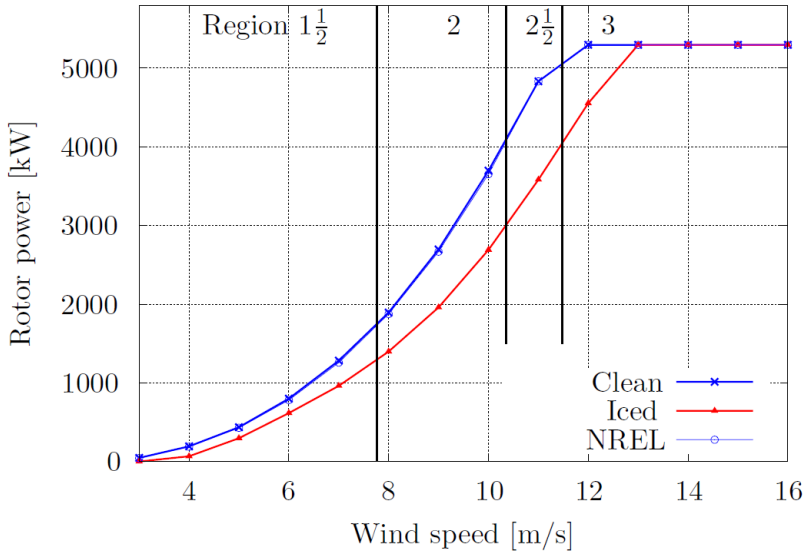

Figure 3.14: Power curve for Control (NREL), normal (Clean) and ice (Iced) conditions [Homola et al., 2011]

.

During an icing event at night on the January 8, 2009 we can see from figure 3.15 that the production was well below the modelled estimation. We can see the production jumps in production output at 8 m/s, this could be shedding of the ice on the blade. Note that the wind turbine needed 20% higher wind speed to reach rated wind speed [Homola et al., 2011].

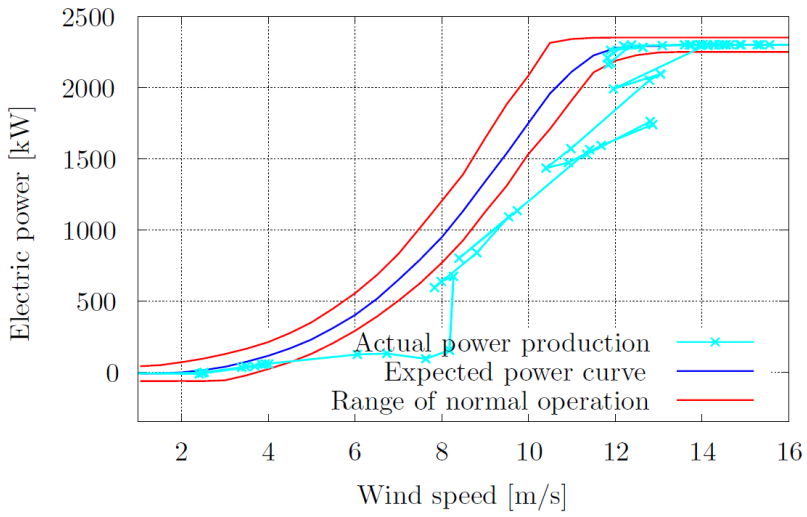

Figure 3.15: Power production measurement during icing event on Nygårdsfjellet Wind farm 08.01.09 [Homola et al., 2011].

Wind speed	Icing case		
[m/s]	Start of icing	Light icing	Moderate icing
4	31 %	33 %	36 %
5	20 %	22 %	26 %
6	17 %	18 %	24 %
7	17 %	18 %	24 %
8	17 %	18 %	24 %
9	17 %	18 %	24 %
10	18 %	19 %	25 %
11	17 %	18 %	26 %
12	17 %	19 %	28 %
13	14 %	17 %	29 %
14	4 %	8 %	23 %
15	0 %	0 %	15,2 %
16	0 %	0 %	8,7 %
17	0 %	0 %	4,6 %
18	0 %	0 %	0 %
19	0 %	0 %	0 %
20	0 %	0 %	0 %
21	0 %	0 %	0 %
22	0 %	0 %	0 %
23	0 %	0 %	0 %
24	0 %	0 %	0 %
25	0 %	0 %	0 %

Figure 3.16: Production loss as percentages for start of icing (10 g), light icing (50 g) and moderate icing (250 g) when compared to normal conditions [Turkia et al., 2013].

Power curve for icing condition were simulated by [Turkia et al., 2013] for the three icing threshold mentioned by [Hämäläinen and Niemelä, 2017]. The simulation was used for a 3 MW turbine with a 90 meter rotor diameter, however due to lack of rotor geometry, rotor geometry for a NREL 5 MW was scaled down to fit the turbine in question. Interestingly they noticed that the production dropped already early in the icing phase, due the increase drag of rough surface on the blade. The result of this simulation is shown in figure 3.16.

Applying these percentages on our Vesta V164-8.0 power curve we get power curves for each threshold ice loads. Due to difference in rated wind speed for the turbine used by [Turkia et al., 2013] and Vesta164-8.0, we had to edit the values. Figure 3.17 show a large drop in production already from normal to light icing condition, indicating the impact in the early stages of icing. We see a slight drop in power between loads of 10 g and 50 g, and a significant drop in production for ice load exceeding 250 g.

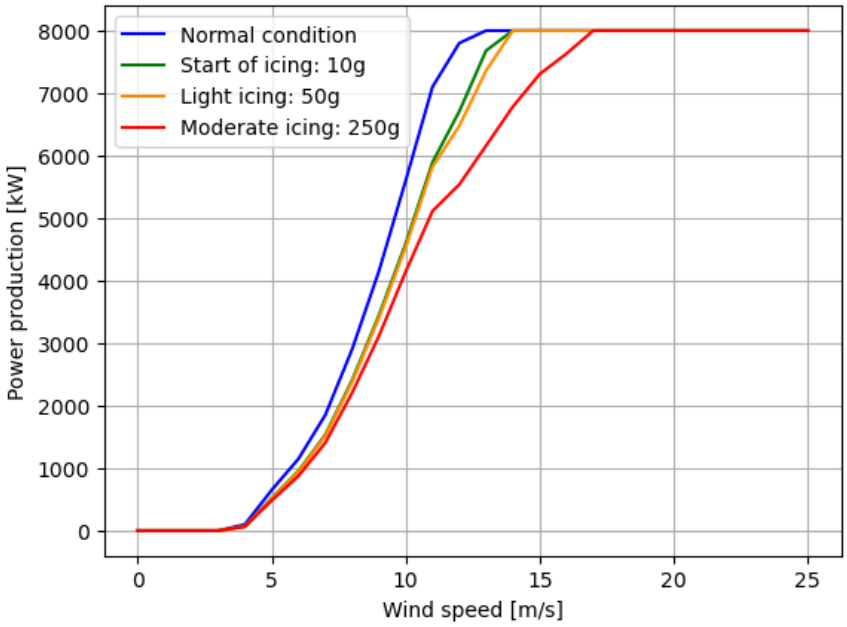

Figure 3.17: Power curve for normal condition (blue), start of icing (green), light icing (orange) and moderate icing (red).

In this thesis we will use the ice loads thresholds of 10 g, 50 g, 250 g and 500 g for estimating production loss. Where load of 10 g, 50 g, and 250 g will follow the decrease in production from figure 3.17 and for loads above 500 g will result in no production.

Site ice index

From the EUMETNET/SWS II Report a site ice index is introduced as a parameter used to determined how severe the ice accretion is expected at a given location by looking at icing frequency, duration and intensity [Fikke et al., 2007].

Site icing index	Days with meteorological icing / year	Duration of meteorological icing %/year	Intensity of icing g/100 cm^2/h (typical)	Icing severity
S5	> 60	> 20	> 50	Heavy
S4	31-60	10-20	25	Strong
S3	11-30	5-10	10	Moderate
S2	3-10	< 5	5	Light
S1	0-2	0-0.5	0-5	Occasional

Figure 3.18: Site ice index for frequency, duration and intensity of ice conditions [Fikke et al., 2007].

4

Result

4.1 Model terrain height

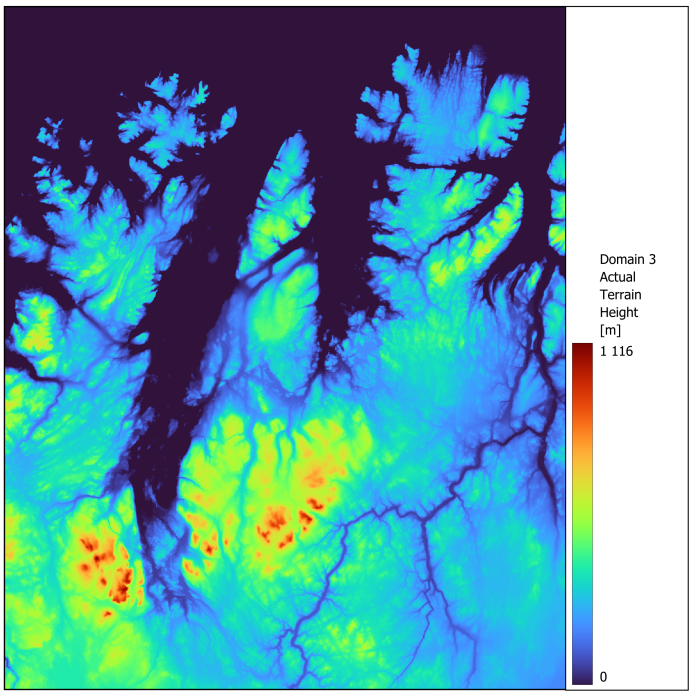

Figure 4.1: Actual terrain height in the innermost domain, color determines the height. Figure made with QGIS using 'høydedata' DTM10 map.

The map shown in figure 4.1 show the actual terrain height for domain 3. However, the model will 'simplify' the terrain in order to spare computational time. We will therefore expect to see difference wind climate for the different domains.

The grid resolution determines the amount of smoothing of terrain. To get an idea of how the terrain height is in the different domains, we have plotted the model terrain with five turbine location at its terrain height. Complex terrain increase surface roughness and has an influence on how the wind moves, and is therefore important to look at how the terrain is smoothed for the different domains.

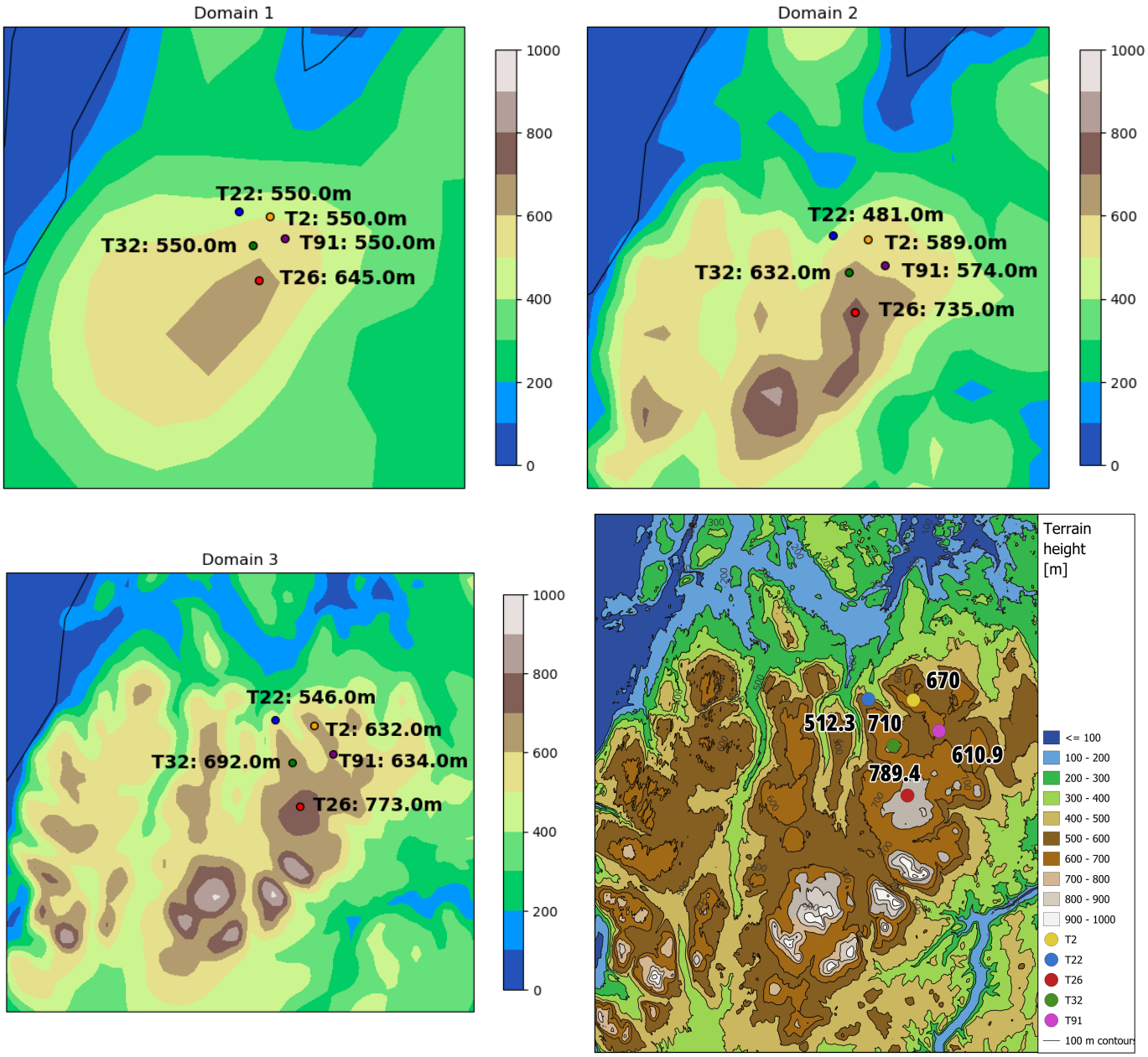

Figure 4.2: Model terrain with color coded turbine location and terrain height, T22: blue, T2: orange, T91: purple, T32: green, T26: red. Map color show terrain height. Top left: Model terrain for domain 1. Top right: Model terrain for domain 2. Bottom left: Model terrain for domain 3. Buttom right: Actual terrain made with QGIS using 'høydedata' DTM10.

The maps in figure 4.2 shows the terrain height for the the three different

domains and one for the actual terrain. We can see that domain 1, where the smoothing is the heaviest, four out of five location have the same terrain height. This could be because the height is gathered from the nearest grid point, since it is low resolution they could all share the same point, therefore the height of the point and the coloring of the map is not consistent. To get a better idea of how the terrain changes for the domain, we have taken the model terrain height and subtracted it to the actual terrain height. Figure 4.3 show the difference in terrain height for domain 2 and domain 3. We can see that the model underestimates the terrain height for every location in domain 2. In domain 3 we can see that the two location with the lowest terrain height are overestimated, and underestimates all other locations. We can easily see that domain 3 are much closer to the actual terrain height than domain 2.

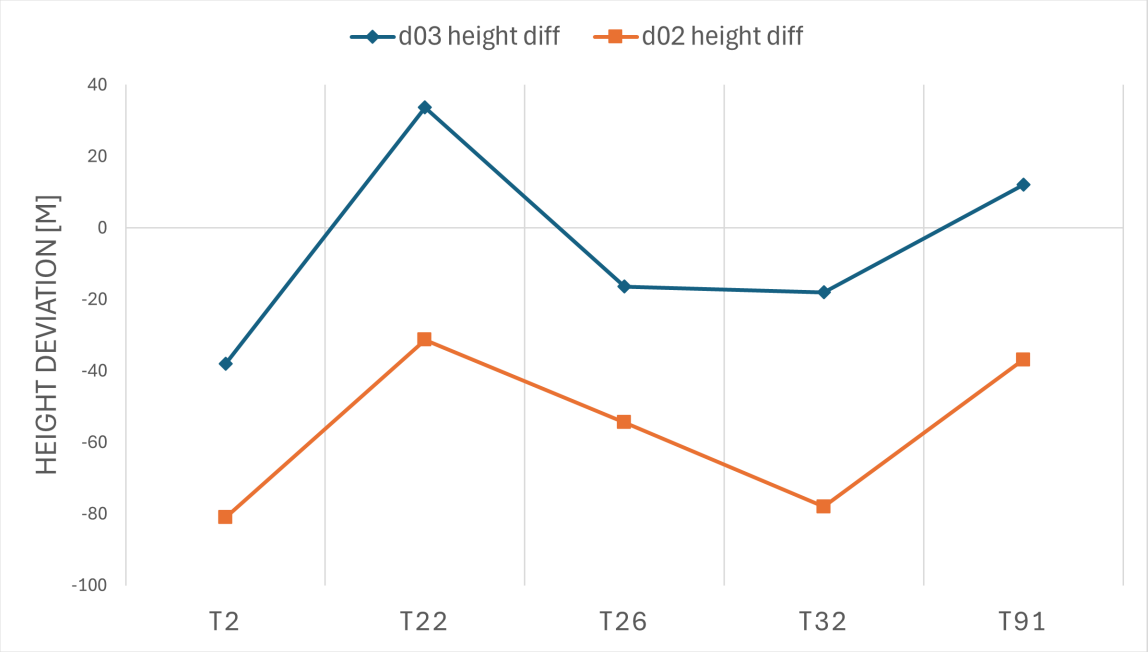

Figure 4.3: Difference in terrain height for the different locations for domain 2 (orange) and domain 3 (blue).

4.2 Banak weather comparison

The data from NCCS was stored as daily mean (24h), which meant we had to convert our dataset to the same format in order to compare. In figure 4.4 we have plotted observed (blue) and simulated (red) values using WRF for the innermost domain.

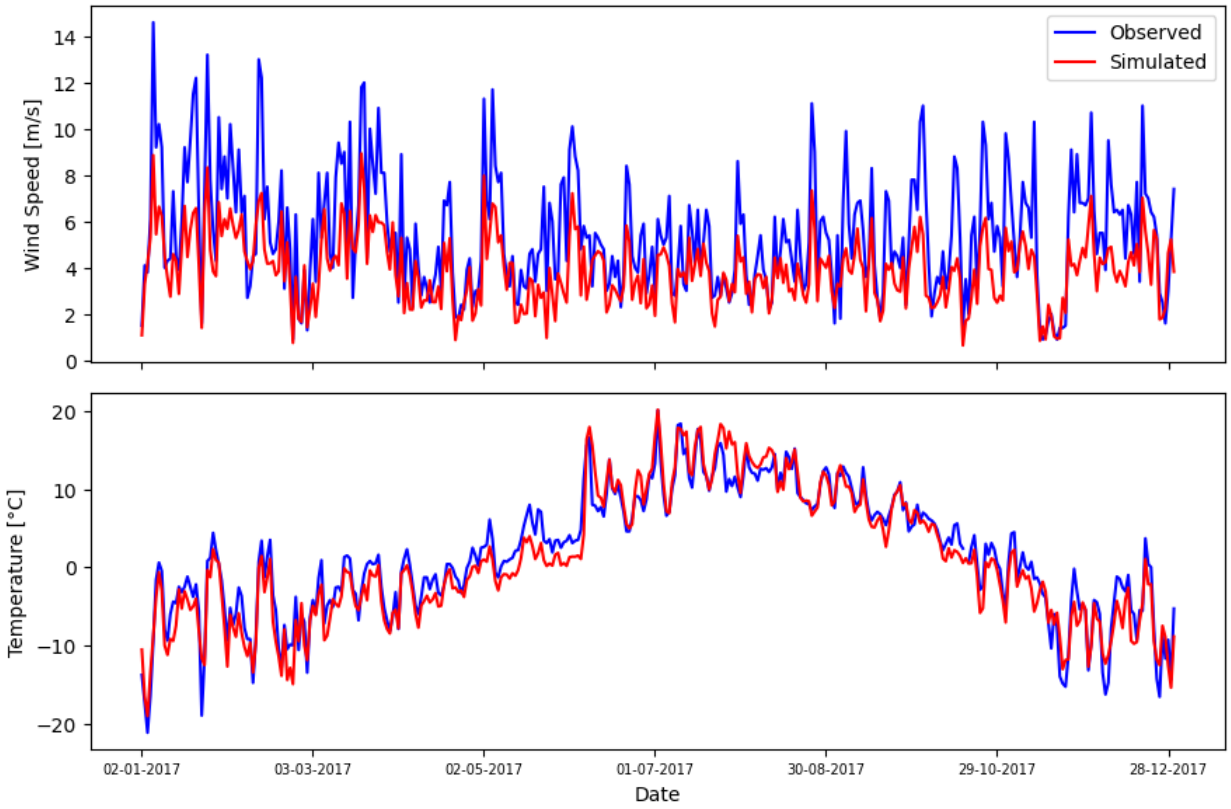

Figure 4.4: Daily mean wind speed (first row) and temperature (second row). Observed (blue) and simulated (red) values for the year 2017

We can see from the first row in figure 4.4 that the observed wind speed are consistently higher than the simulated values. We can see that they share the same pattern for wind values, especially shown in the sudden low wind speed period around the 16.11.2017. The second row show the evolution of temperature during the year 2017. Here we can see that the simulation predicts the observed temperatures with great accuracy.

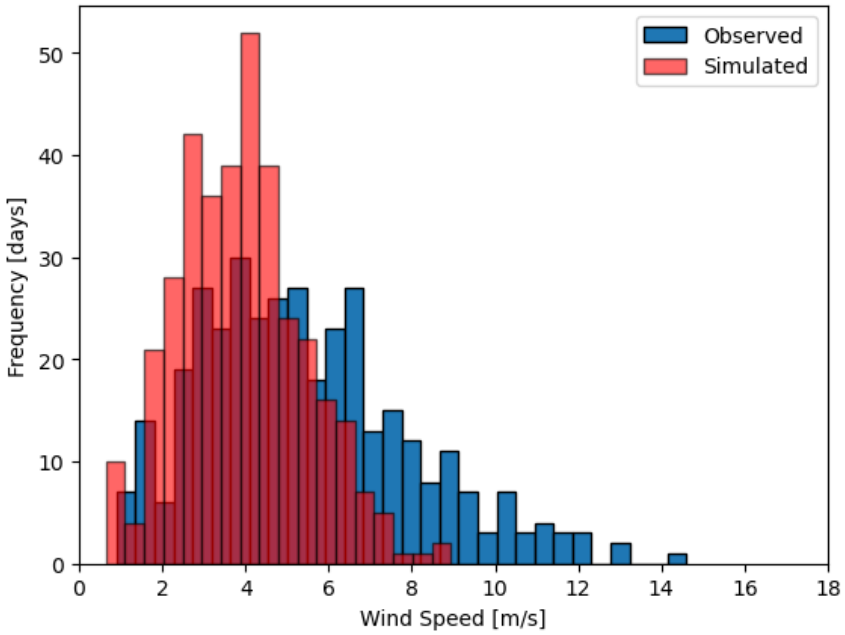

Figure 4.5: Histogram for wind speed. Observed (blue) and simulated (red)

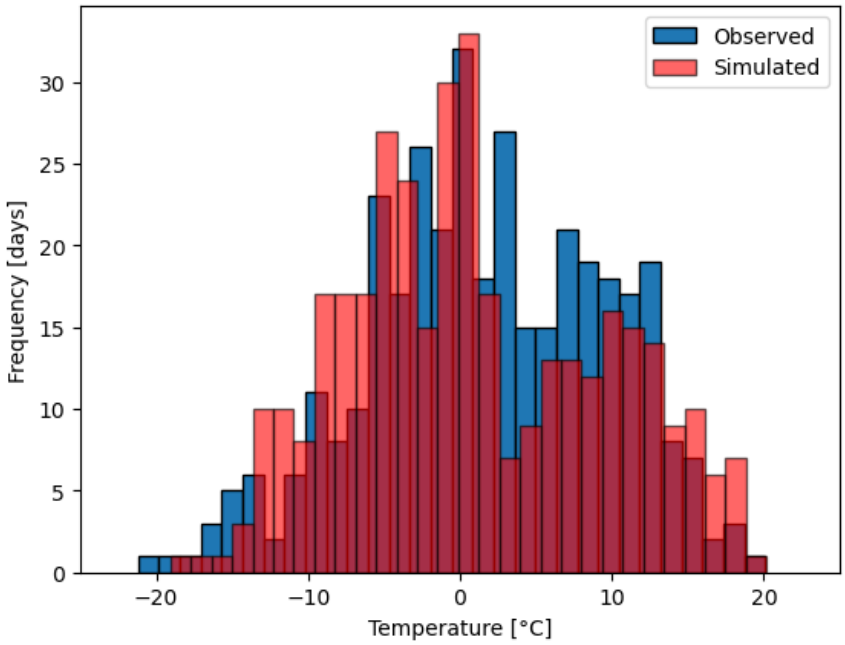

Figure 4.6: Histogram for temperature. Observed (blue) and simulated (red)

The histogram in figure 4.5 and 4.6 gives a better indication of how well

the model predicted temperature and wind speed. Here we can see that the model failed to replicate the higher wind speed that the measurement shows. The complexity of the terrain around the measuring station could impact the models tendency for low wind speed. While the temperature histogram show that the simulation predict less temperature in region about 4-12 ^{o}C, and more temperatures in region with - 12^{o}C and - 8^{o}C.

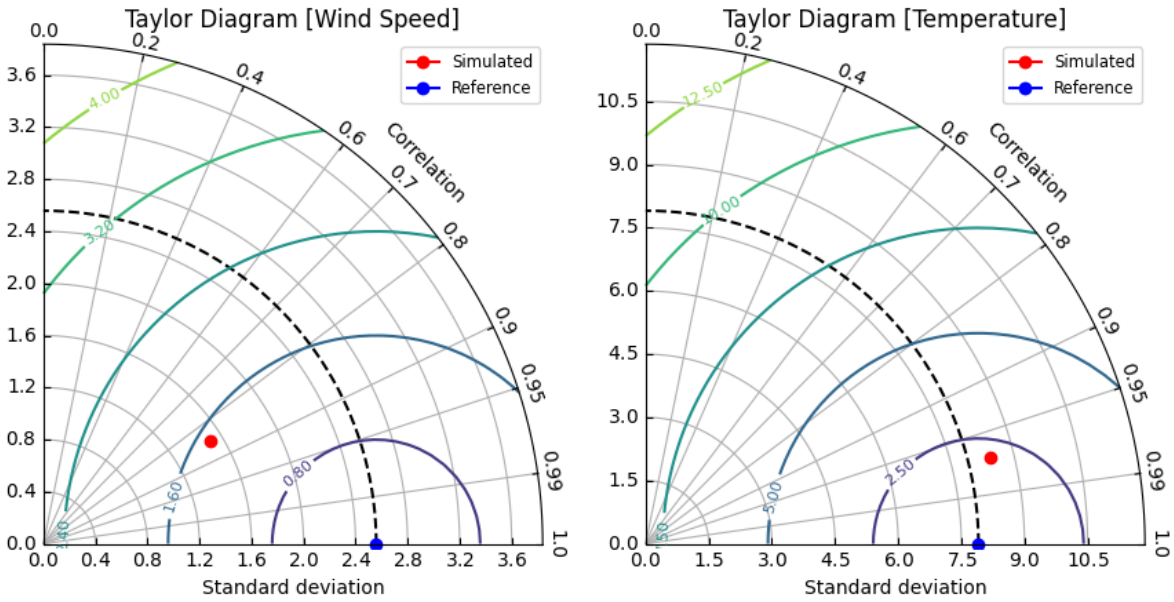

Figure 4.7: Left: Taylor diagram for wind speed. Right: Taylor diagram for temperature. Blue dot indicate the reference value (observed value) and red dot indicate simulated value. Standard deviation on the radial axis, correlation coefficient on the azimuth axis and constant centered root-mean-square error on the contours.

Taylor diagram in figure 4.7 show a strong correlation coefficient (ρ) between model and observed data for temperature. Here we can observe that the simulated wind speed is less varied while also show less correlation than the simulated temperature. All the statistical metrics are shown in table 4.1.

Parameters	$\bar{x}_{Sim}$	$\bar{x}_{Obs}$	σ_{Sim}	σ_{Obs}	$RMSE$	$CRMSE$	ρ
Wind Speed	3.91	5.45	1.50	2.56	2.15	1.50	0.85
Temperature	0.96	1.73	8.43	7.91	2.21	2.07	0.97

Table 4.1: Statistical metrics for the simulated and observed dataset. Mean ($\bar{x}$), standard deviation (σ), root-mean-square error ($RMSE$), centered root-mean-square error ($CRMSE$) and correlation coefficient (ρ).

4.3 NEWA result

To compare the NEWA result with domain 2 result we choose the location of a central turbine to extract data. The NEWA data is extracted at latitude 70.14142 N and longitude 26.27545 E at height 200m, which correspond to hub height at turbine location T32 shown in figure 3.3.

The data for the year 2014 was excluded due to missing values. We decided to do this in order to to ensure that the data presented was correct. It is desired to include all available data, but we want to avoid the introduction of inaccuracies.

From the figures 4.8 we can see a trend towards a slight decrease in yearly mean wind speed, with mean wind speed of 10.08 m/s in 2017. The trend of the yearly mean temperatures shown in figure 4.9 is increasing. The mean temperature for 2005 is -1.55^{o}C, while the mean for 2018 is -0.75^{o}C.

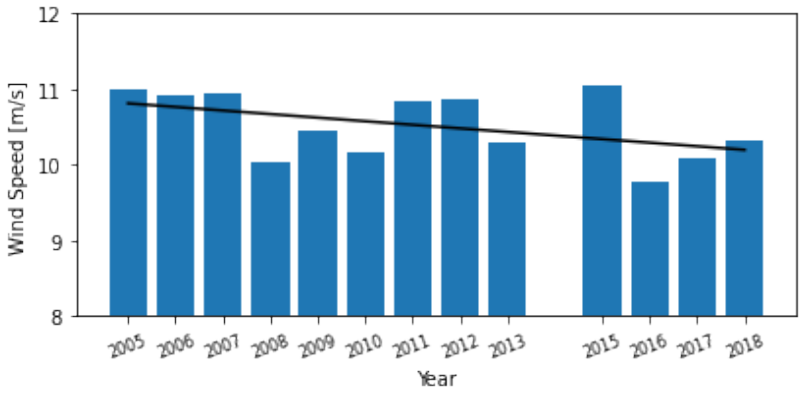

Figure 4.8: Mean wind speed from 2005 - 2018

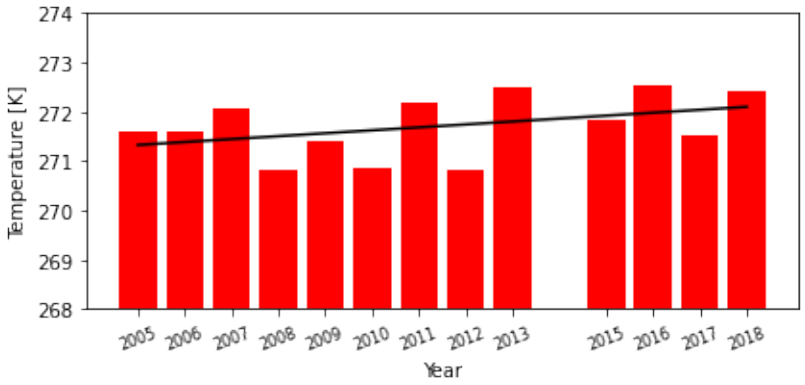

Figure 4.9: Mean temperatures from 2005 - 2018 shown in Kelvin

Since NEWA gives us ice load, we need to convert it to ice rate in order for us to compare it to the WRF result. To show how the load and rate are related, we have plotted ice load and ice rate for a week in 2017 in figure 4.10. Here we can see that since NEWA's iceBlade model includes both ice accretion, sublimation, wind erosion and ice shedding, we get both positive and negative ice rates.

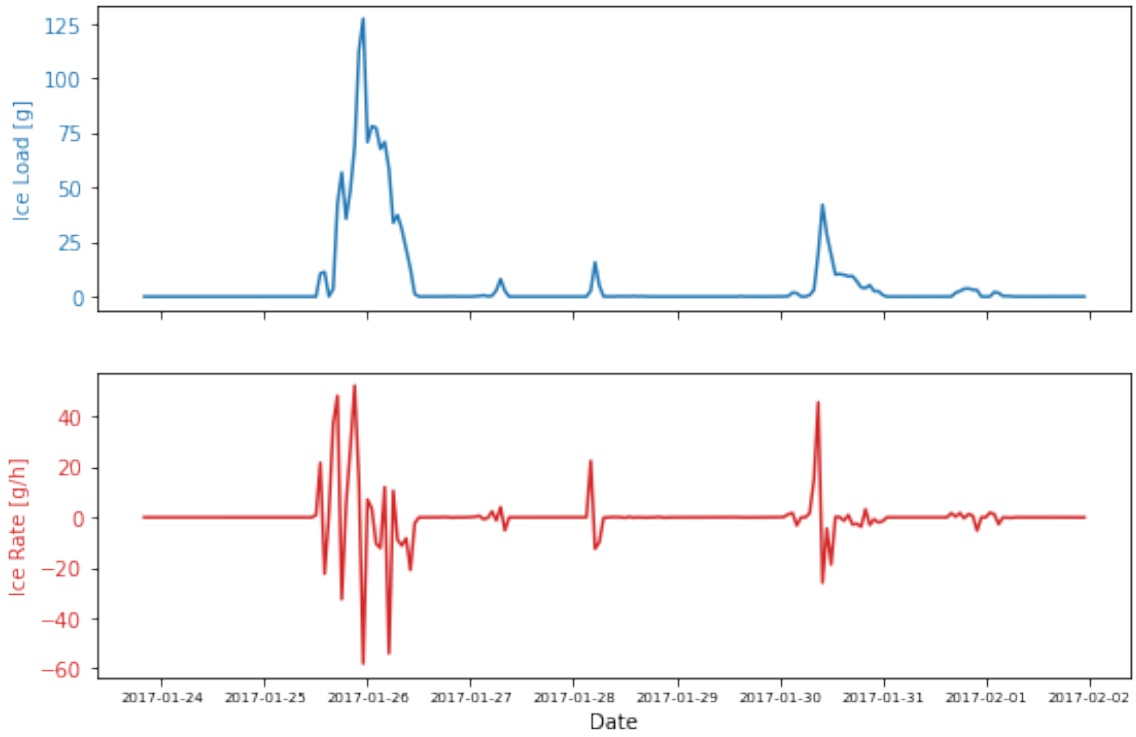

Figure 4.10: Ice load [g] (upper plot) and ice rate [g/h] (lower plot) for a week in 2017.

Hours with icing rates above 10 g/h is highly variable for the time period, from figure 4.11 we see that the lowest amount of icing hours is in 2013 with 84 icing hours, while the highest is in 2017 with 156 icing hours above 10 g/h. We can observe the trend for time period is slightly decreasing.

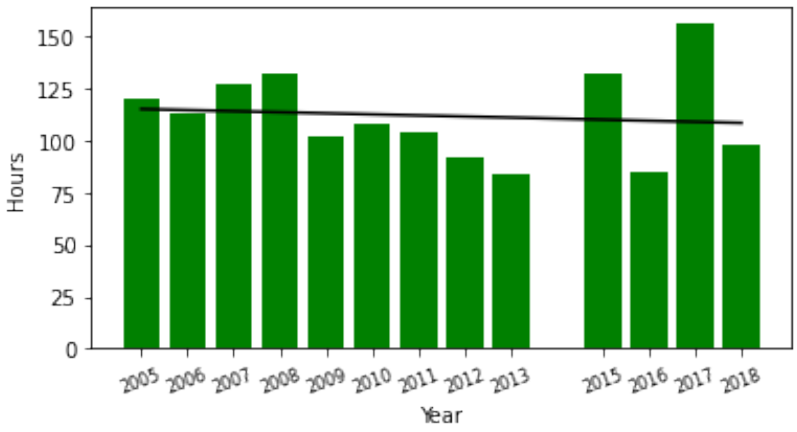

Figure 4.11: Hours with icing above 10 g/h

The variability is also showing in figure 4.12, with the lowest in 2008, 2010 and 2011 with 5 icing hours and the highest in 2005 with 16 icing hours. For this dataset we can see that the trend is decreasing.

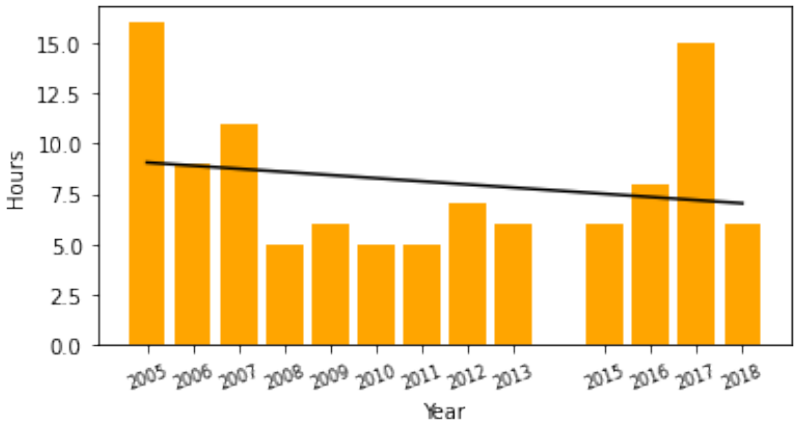

Figure 4.12: Hours with icing above 50 g/h

Table 4.2 contains parameters for the WRF simulation in second domain and NEWA simulation in year 2017. NEWA is predicting higher mean wind speed and higher mean temperature, while the terrain height is 8 m lower than the WRF simulation. The two simulation have the same grid resolution, but NEWA have larger outer domain which could impact the results. However, we can see from the icing hours above 10 g/h, iceBlade model is 82% less than WRF do2.

The trend plots show how the mean values varies for the time period, and give a picture of what values we could expect. For 2017, the predicted wind speed and temperature was lower than the trend, however the icing was far above the trend for each threshold.

Parameters	NEWA	WRF do2	WRF do3	WRF do3*
Terrain height [m]	624	632	692	692
Mean Wind Speed [m/s]	10.08	9.92	10.02	8.69
Mean Temperature [K]	271.52	271.26	270.81	270.74
Ice > 10 g/h [h]	156	887	1212	1136
Ice > 50 g/h [h]	15	400	626	541
Ice > 250 g/h [h]	0	62	87	72

Table 4.2: Comparison between NEWA and WRF (do2, do3 and do3*) parameters for year 2017. do3* includes wind turbines.

4.4 Annual data analysis

In order to look at the annual weather development for Davvi wind farm, we have calculated average value of the weather parameters for all turbine locations for each 10-minute time step. The average values are calculated from the WRF result on the innermost domain with turbines included. This way we can get a picture of how the general weather conditions was during our 2017 simulation. The values collected are gathered from Vesta V164.8.0 hub height, 200 meter above ground level.

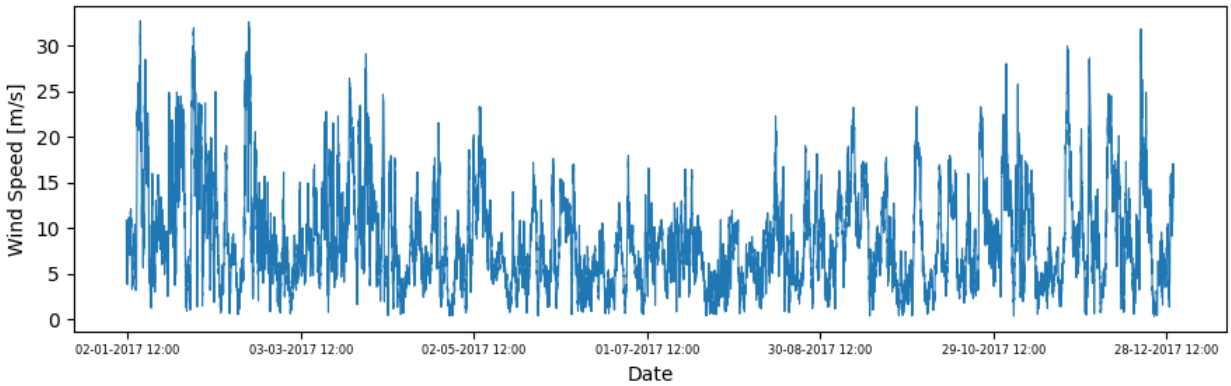

Figure 4.13: Mean wind speed for all turbines.

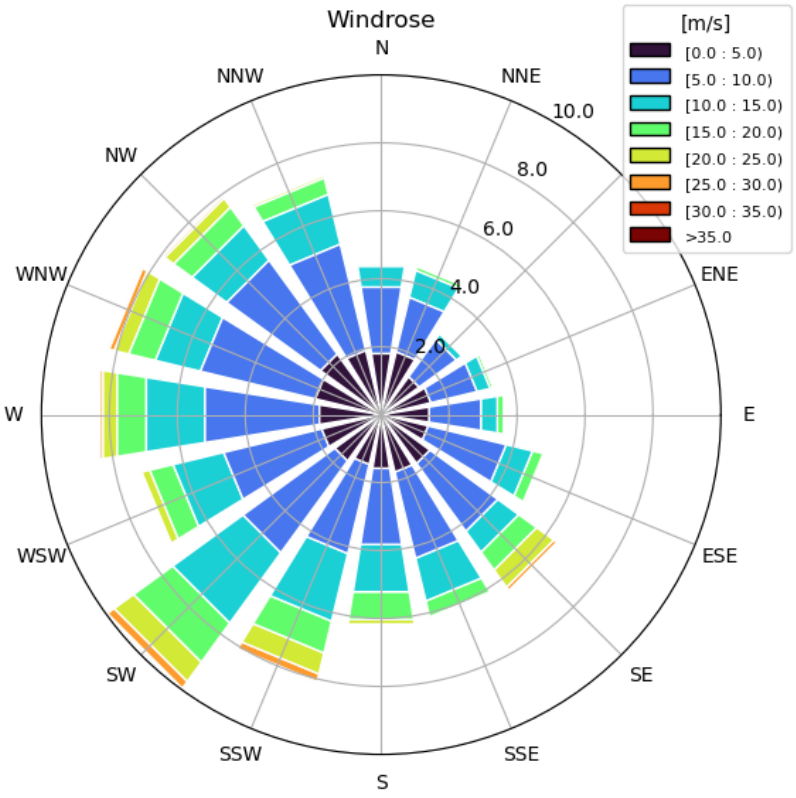

Figure 4.14: Windrose for the average wind direction and wind speed for all turbines.

The mean wind speed for all the turbines is shown in figure 4.13. We can spot that the average wind speed are greater in the winter months, which will contribute to the icing conditions. The overall mean wind speed is 8.72 m/s, which indicate good wind resource. Windrose in figure 4.14 show the annual mean wind direction with the radius indicating percentages. We can see that most of the wind is coming from south-west (SW) direction with a frequency of about 10%. The color indicate the wind speed, high wind speeds comes most often from south-west and south-south-west.

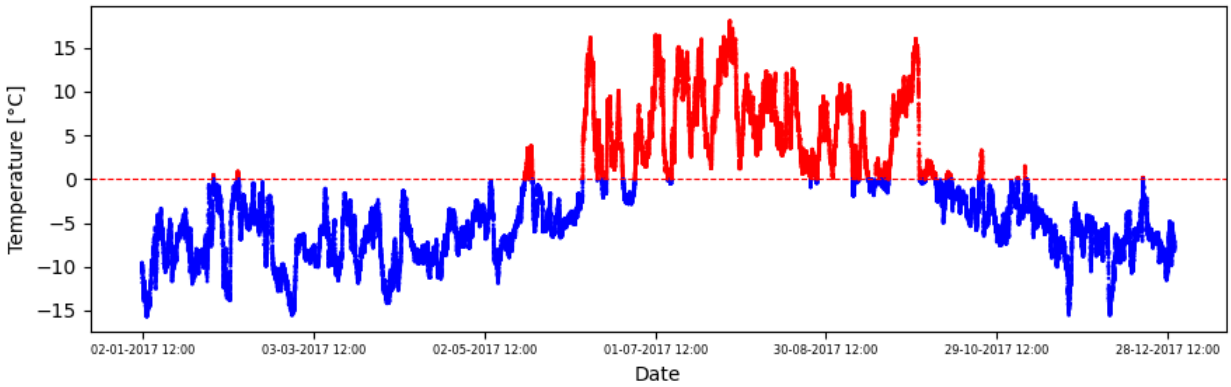

Figure 4.15: Mean temperature for all turbines. Blue is indicating values below freezing and red above freezing.

The mean temperature plotted in figure 4.15 show the temperature for the simulated period. Temperature is a very important part of icing, as we assume no icing when temperature is above o^{o}C. We can see two short section of positive values in January/February, however the consistent positive values starts in June and last until about October. This means that about 8 out of 12 months is consistently under freezing temperatures. If we isolate the months with mostly positive values; June, July, August and September, the mean temperature $\bar{x}_{summer}$ = 5.71 ^{o}C and for winter months $\bar{x}_{winter}$ = -6.02 ^{o}C. Temperatures below freezing is occurring 67.89% of the time with the annual mean temperature of -2.07 ^{o}C.

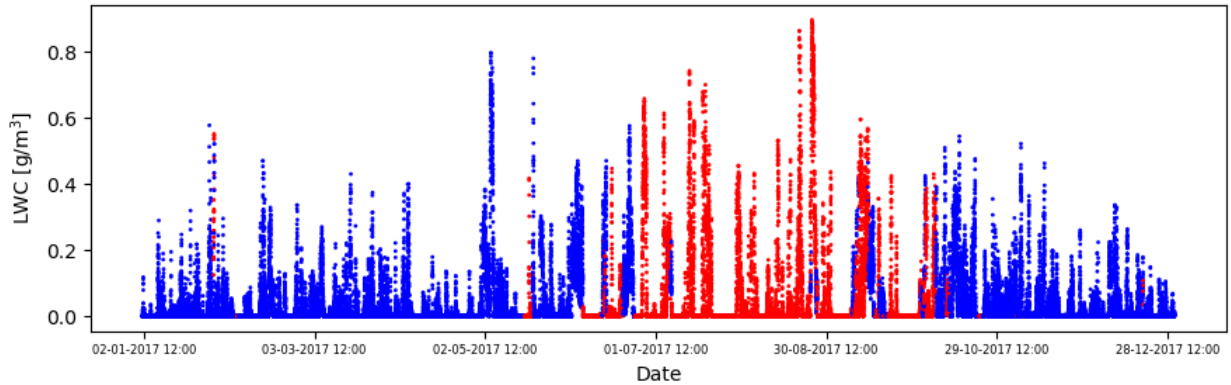

Figure 4.16: Mean liquid water content for all turbines. Blue indicate LWC when T < o^{o}C and red when T > o^{o}C.

The amount of liquid water in the air is an important component for ice

accretion as it indicate the amount of available liquid water in the cloud to form supercooled droplets. In figure 4.16 we can see the mean liquid water content for all the turbines. The blue indicate LWC for temperatures below freezing, and red for LWC above freezing. Since we assume dry icing we can see that icing is expected throughout the whole of January to May, and sporadically in June and September, then again from October to December.

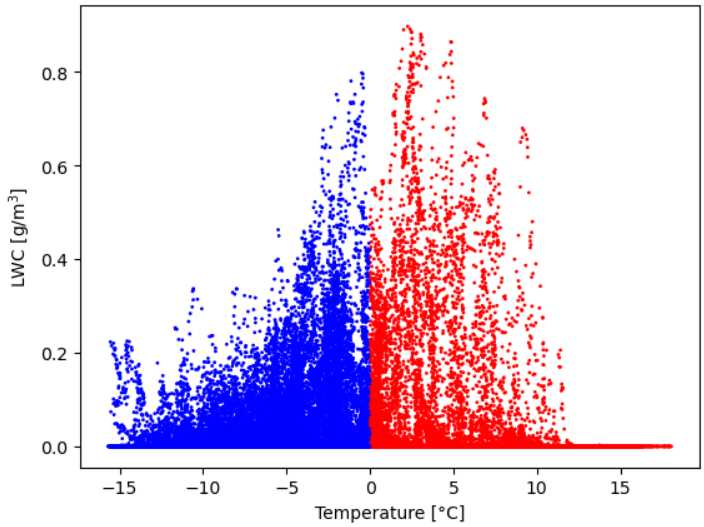

Figure 4.17: Liquid water content and temperature. Blue indicate LWC when T < o^{o}C and red when T > o^{o}C.

In figure 4.17 we can see the relation between LWC and temperature. Air can hold more liquid water for warmer temperatures than for colder temperatures. This shows us that we can expect more severe icing events when the negative temperatures are close up to o^{o}C.

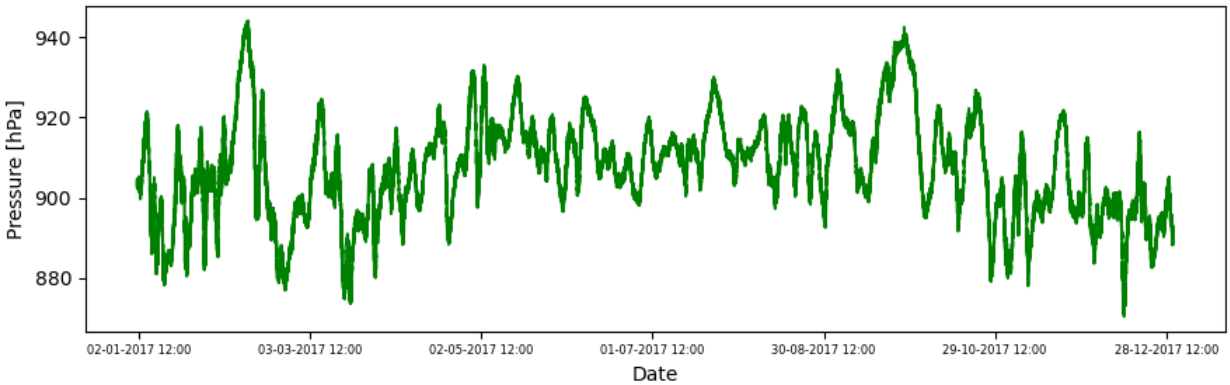

Figure 4.18: Mean air pressure for all turbines.

Air pressure dictates the movements of air masses, where air will move from high pressure areas to low pressure areas. Strong air pressure gradient, will create strong winds. Figure 4.18 show the mean air pressure for each location at hub height. If we isolate the summer months, we can observe a greater variability in mean air pressure during winter months by estimating the standard deviation for each period. For summer months $\sigma_{summer} = 928$, while the winter months $\sigma_{winter} = 1248$. This is consistent with figure 2.4 showing that mean sea level pressure gradient is steeper during winter months, implying fast change in air pressure, leading to greater variability.

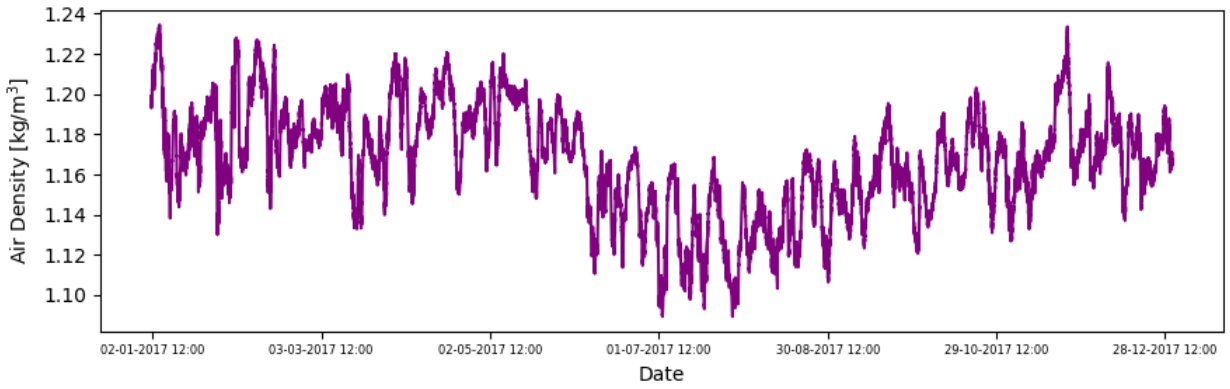

Figure 4.19: Mean air pressure for all turbines.

Air density is an important factor in wind power production, as shown in equation 2.7. Density is dependent on pressure and temperature, in figure 4.19 we can see that when temperature rises, the mean density drops and is lowest in the summer months. The annual mean density is 1.17 kg/m^3. If we now use equation 2.8 for wind power density, we can input annual mean wind speed and annual mean air density and get the annual mean power density. If we insert wind speed and air density, it tells us that Davvi wind farm had an annual mean power density of 387.89 W/m^2 for 2017.

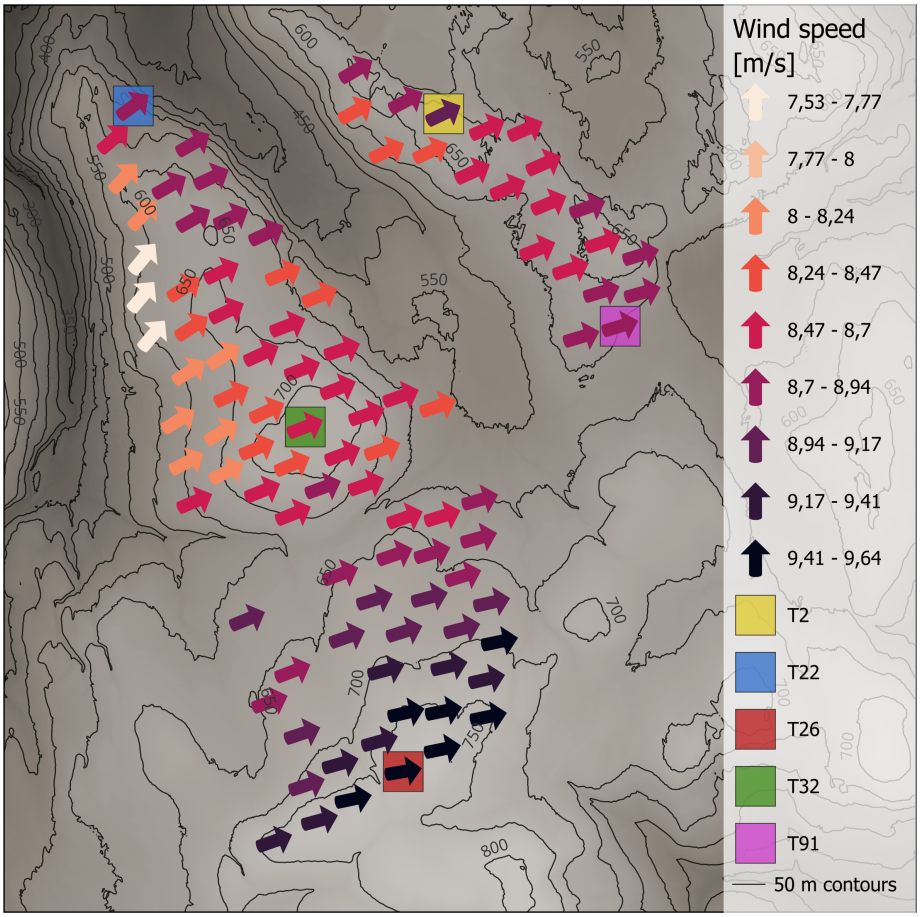

Figure 4.20: Average wind speed and wind direction for every turbine location. Average wind speed are indicated by color and average wind direction is shown by arrow.

Annual average wind speed and wind direction are shown in figure 4.20, arrow show annual mean wind direction and arrow color indicate annual average wind speed. The colored square shows the position of the five chosen turbines previously mentioned, those being T2 (yellow), T22 (blue), T26 (red), T32 (green) and T91 (purple). We can observe that T26 has the strongest mean wind speed of these five locations with mean wind directed easterly, while T22 has the lowest mean wind speed and directed more north-east.

4.5 Ice accretion analysis

4.5.1 Icing hours

We have estimated the annual icing hours where the icing rate exceeds icing thresholds of 10 g/h, 50 g/h and 250 g/h. This is estimated at the each turbine location at 200 meter above ground level and will indicate ice intensity at hub height.

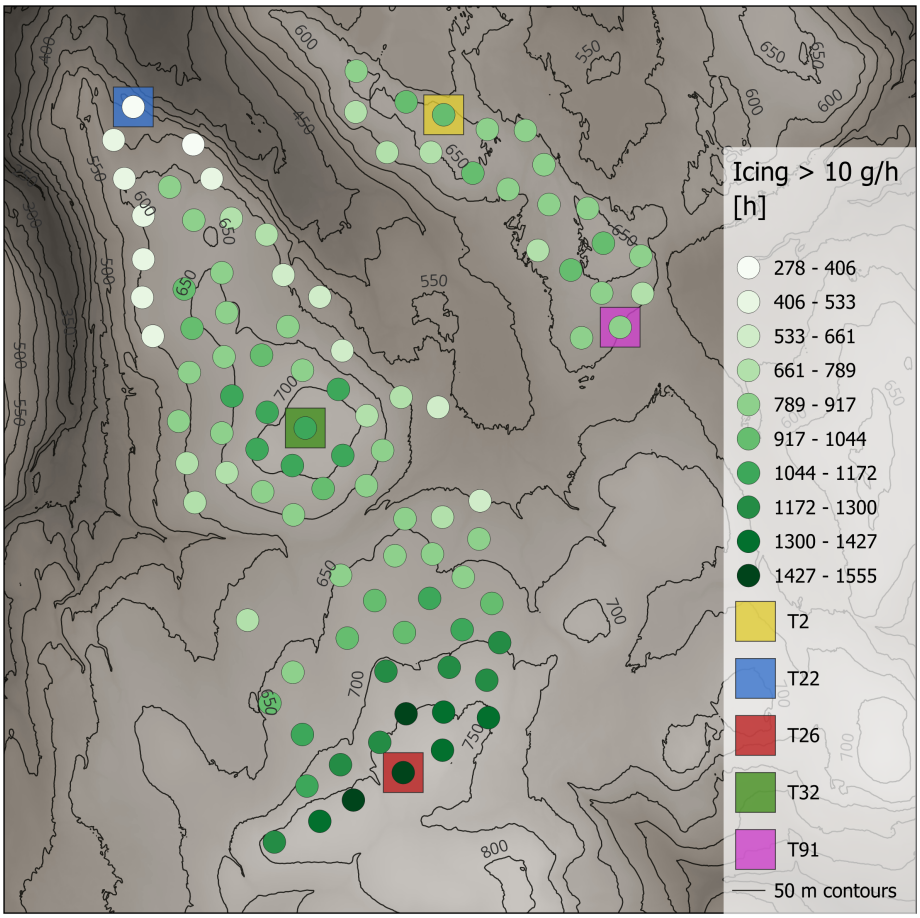

Figure 4.21: Annual icing hours for icing rates > 10 g/h. Color indicate amount of icing hours.

In figure 4.21 we observe the icing hours for icing rate > 10 g/h and indicate the start of icing event. We can observe that the turbine with the highest terrain elevation in the south experience the most amount of icing. Turbine T26 is located at model terrain elevation 773 meter and experience 1555 hours with

an icing rate > 10 g/h, this is 1277 hours more than T22, at an elevation of 546 meter which experience 278 hours with icing rates > 10 g/h.

The next threshold is ice rate > 50 g/h and indicate light icing. In figure 4.22 we can see the icing hours for ice rate > 50 g/h. We see that it follows the same trend as in figure 4.21, turbines with the highest terrain elevation in the south experience the most amount of icing. Turbine T26 again show the most amount of icing with 855 hours above 50 g/h, and T22 the least with 111 hours.

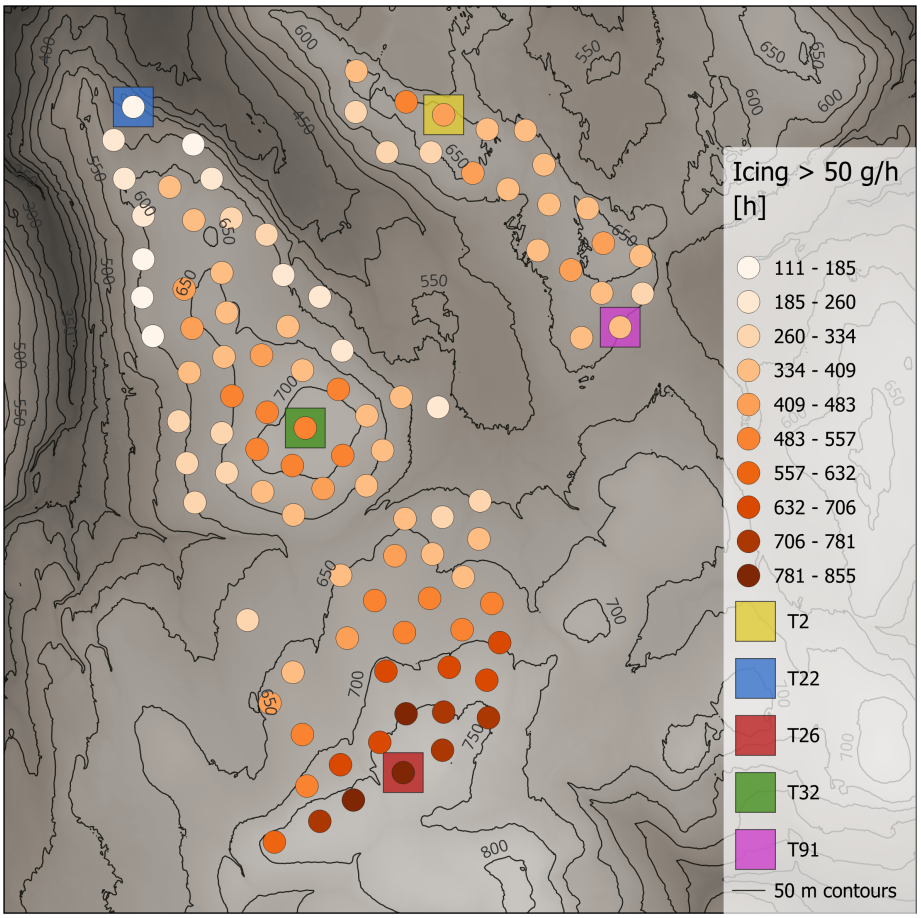

Figure 4.22: Annual icing hours for icing rates > 50 g/h. Color indicate amount of icing hours.

Final threshold we look at is ice rate > 250 g/h, which indicate moderate icing. Figure 4.23 show icing hours with icing rates above 250g/h. We see again that T26 has the highest amount of icing with 171 hours, and T22 the least with 12 hours.

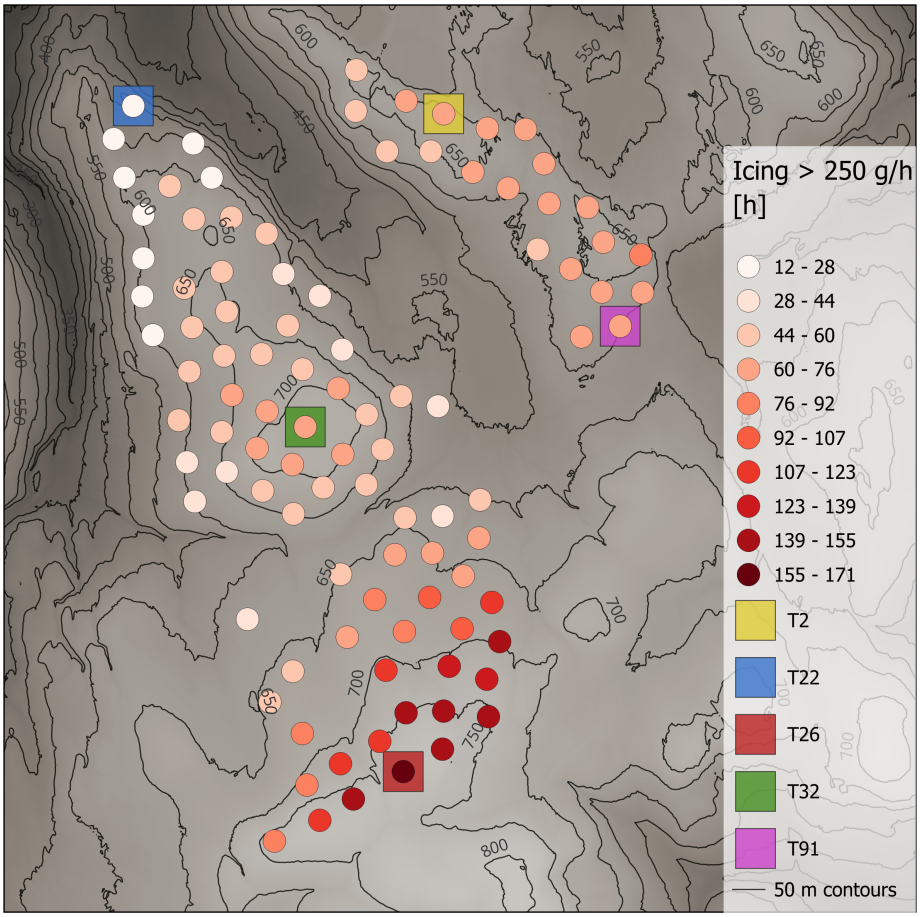

Figure 4.23: Annual icing hours for icing rates > 250 g/h. Color indicate amount of icing hours.

From all three of the icing hours figures we can observe a relation between terrain height and icing hours. In figure 4.24, the annual icing hours for the different icings thresholds is shown as a scatter plot against the model terrain for the turbine locations. The figure show clear relation between terrain height and icing.

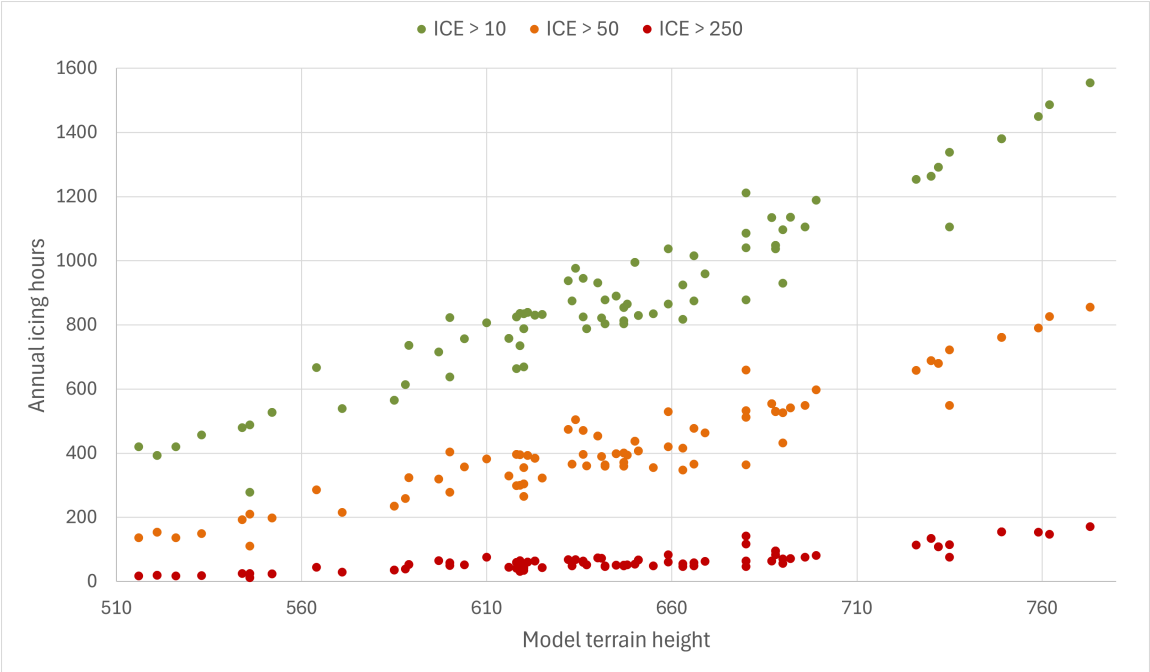

Figure 4.24: Scatter plot showing the relation between model terrain height and icing hours. Color indicate the different icing threshold.

In figure 4.25, we see the annual icing hours over 10 g/h and wind speed over the model terrain as a scatter plot. Here the blue dot indicate the annual mean wind speed and green dot show the annual icing hours.

Visually we can see a stronger linear relations ship between icing and height than wind speed and height. To confirm this we calculated the correlation, $\rho_{ice} = 0.96$ and $\rho_{wind} = 0.71$, confirming that icing has a stronger correlation with model terrain height than the annual mean wind speed. Higher correlation coefficient indicate that the data point are clustered tighter around the linear trend line. Wind speed is affected by a number of factors, like air pressure, surface roughness, complex terrain and wind direction, which could be a reason why we see a lower correlation.

Temperature tends to decrease with height and have a impact the icing, figure 4.26 show a scatter plot with icing hours above 10 g/h and annual mean temperature (with increasing negative degrees on y-axis). Here we can see clear linear relationship between temperature and model terrain height, calculation reveals a correlation of $\rho_{temp} = 0.98$. This shows a stronger correlation then ρ_{ice}, this is mostly because ice is affected by different factors, like we discussed in chapter 2.

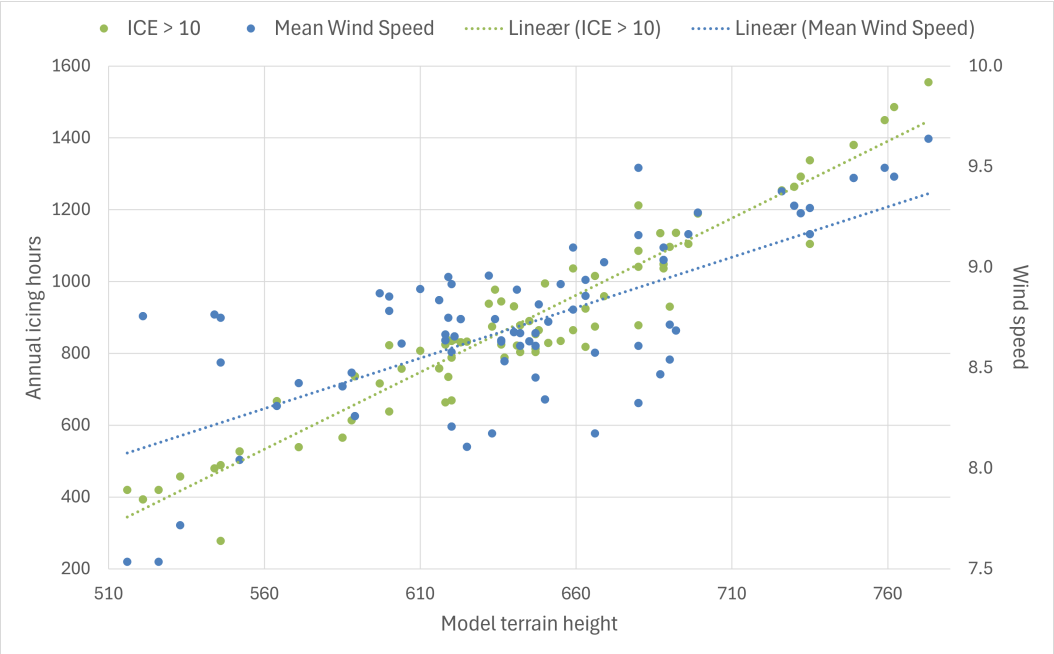

Figure 4.25: Scatter plots and linear trend lines of annual icing hours (over 10 g/h) and annual mean wind speed over model terrain height.

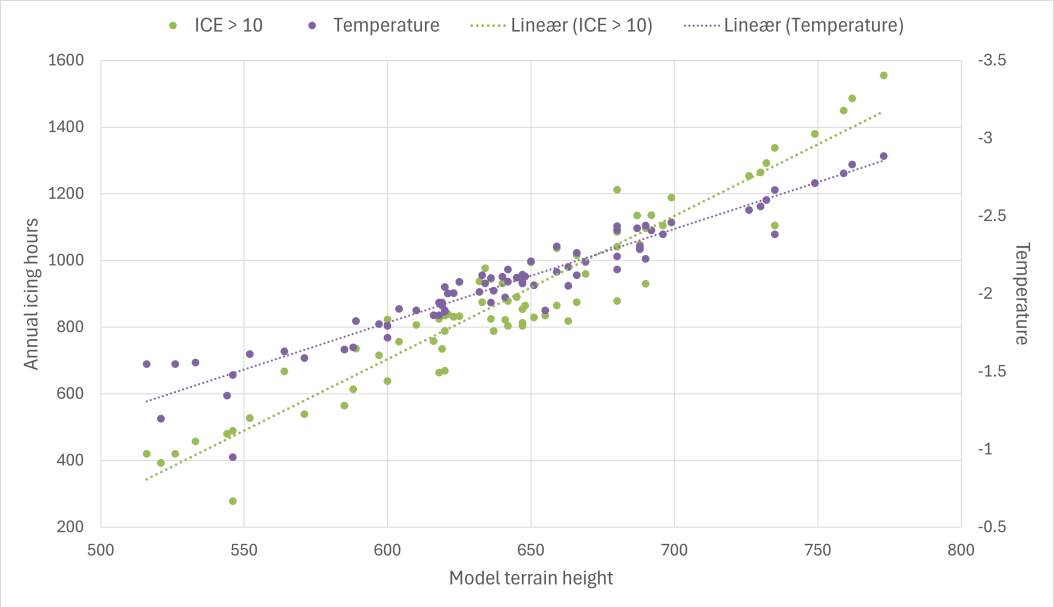

Figure 4.26: Scatter plots and linear trend lines of annual icing hours (over 10 g/h) and annual mean temperature over model terrain height.

Icing map comparison

For comparing WRF icing results with the icing map in figure 4.28, we extracted values for 80 meter above ground level and calculated ice accretion and icing hours. In order to more easily compare the values, we have used the same icing hours classifications as NVE. We observe the same pattern in figure 4.27, where we see stronger icing in location with greater terrain height.

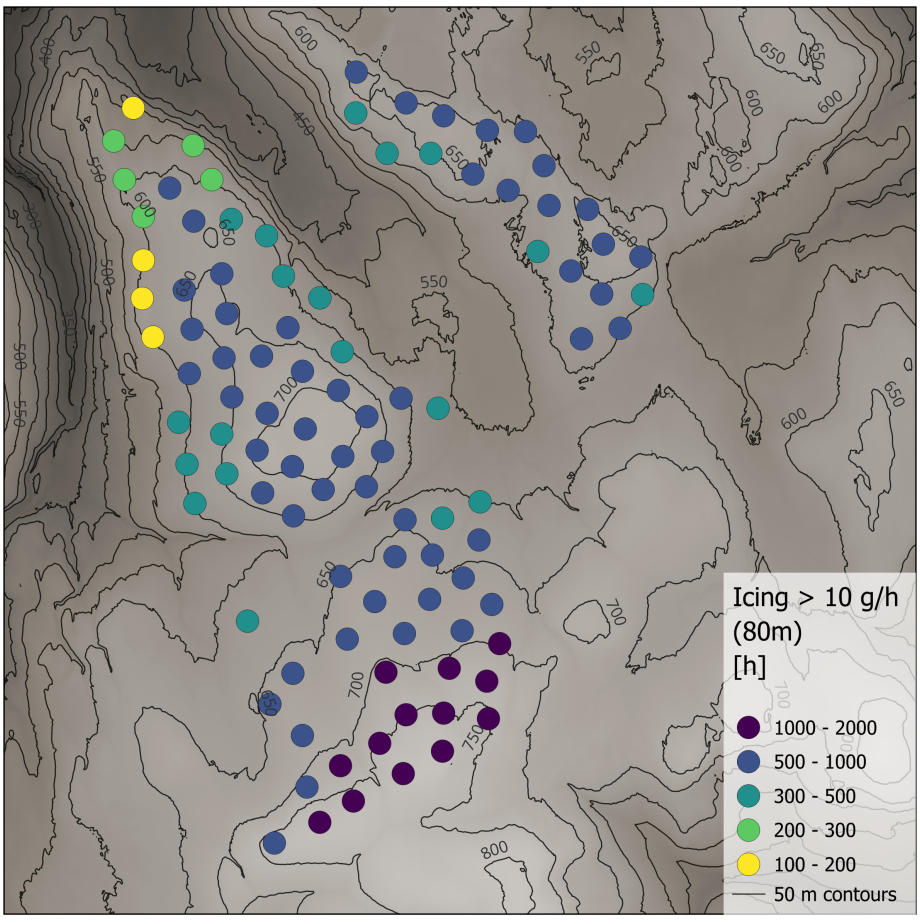

Figure 4.27: Annual icing hours for icing rates > 10 g/h for 80 meter above ground level. Color indicate amount of icing hours.

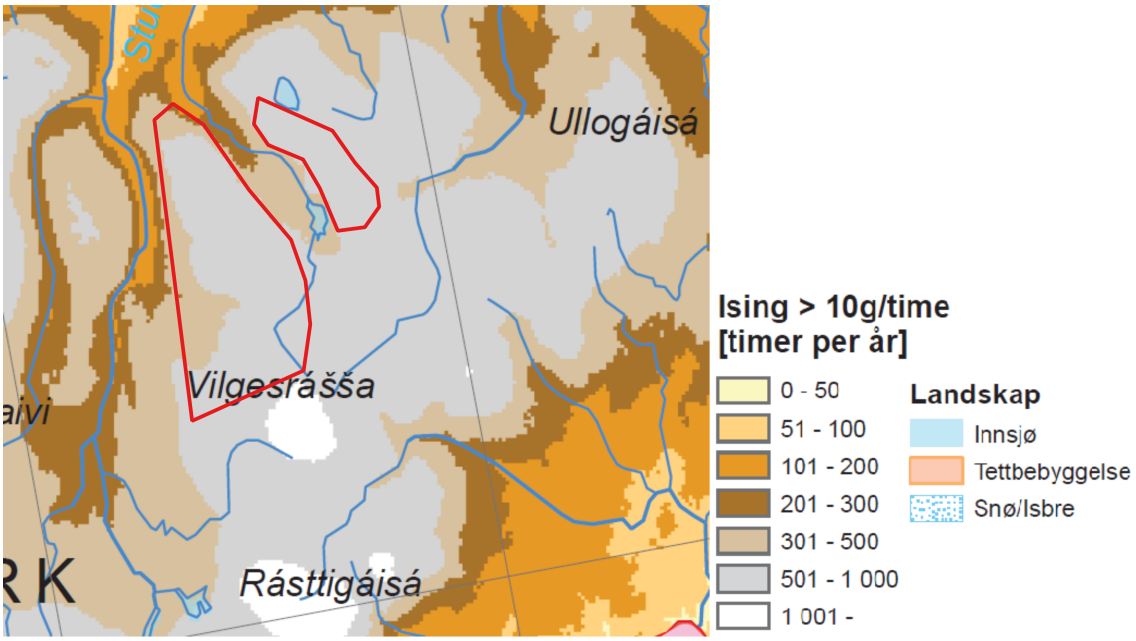

Figure 4.28: Icing map. Red outline show the planned area of Davvi wind farm [Øyvind Byrkjedal et al., 2009b].

Icing map in figure 4.28 show that most of the planned area of Davvi wind farm experienced 501-1000 hours with icing rate above 10 g/h, and a small region in the west and north with 301-500 hours. We can see the same pattern in figure 4.27, where areas with low icing around the edge of the area, likely because the edge has lower terrain height. When looking at the WRF result we can see the icing hours range from about 150 to 1500 with the main value being between 500-1000 hours.

4.5.2 Icing events

Since we assume dry icing, we have excluded ice rates where temperatures are above freezing. Figure 4.29 show the ice rate for turbine T26, which is the turbine with estimated highest total accumulated icing of 182 kg for the entire period. While figure 4.30 show the ice rate for T22, which is the turbine with the lowest estimated total accumulated icing of only 20 kg.

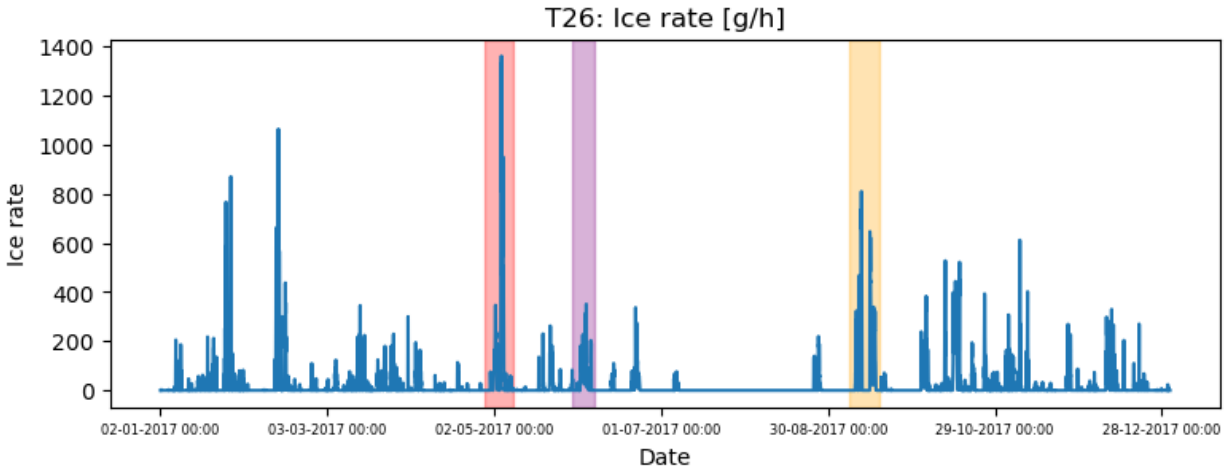

Figure 4.29: Ice rate for turbine T26 during the entire simulation period.

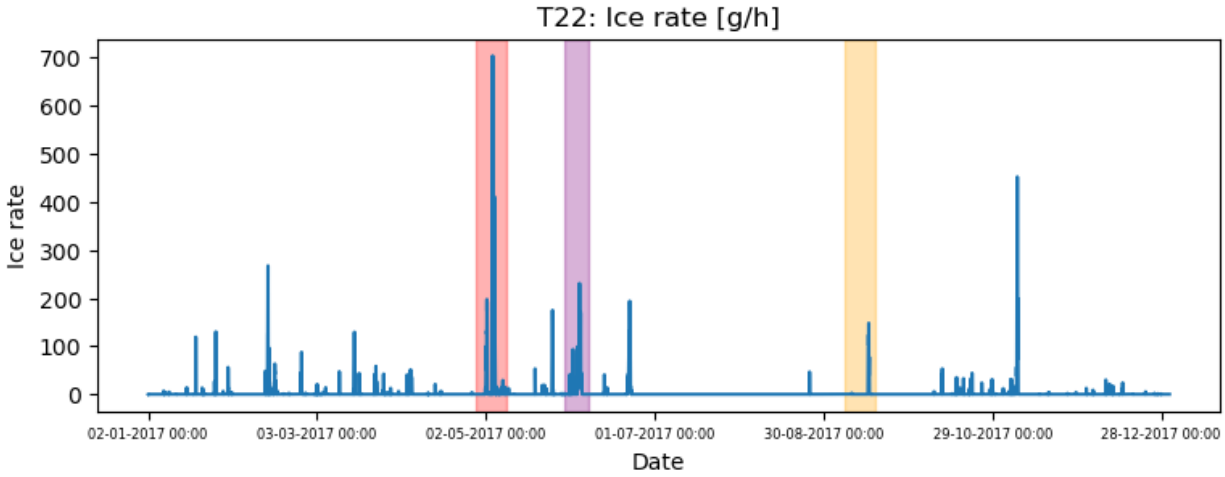

Figure 4.30: Ice rate for turbine T22 during the entire simulation period.

We can see several spikes where the ice rate are high, the highest ice rate shown with a red background and is occurring at 04.05.2017. Purple background is showing the longest continuous icing event of 80 consecutive hours where the ice rate never dropped to zero, and the yellow background showing the only icing event where the wind park experienced icing while wind was coming from south-east.

We will go deeper into each icing event for each of these two turbine to understand what occurred, and look at why there is a large difference in total accumulated ice.

Icing event: Red (01.05.2017 - 06.05.2017)

The icing rate for turbine T22 and T26 during the icing event that occurred from 01.05.2017 - 06.05.2017 is plotted in figure 4.31. Peak icing rate for both turbines occurs on the 04.05.2017, with T26 reaching its peak 14 o'clock and T22 10 o'clock. The vertical dotted grey line indicate the time of the peak icing on turbine T26.

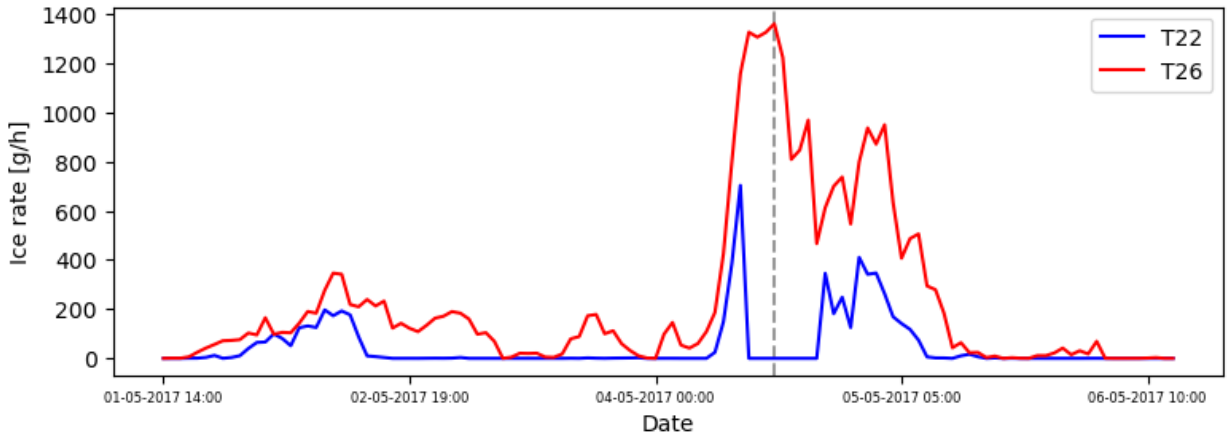

Figure 4.31: Icerate for turbine T22 (blue) and T26 (red) during the ice event.

In the first row of figure 4.32 we can see that the LWC is rapidly increasing during the morning of 04.05.2017, around 07:00, peaking at 0.97 g/m^3 for T26 and 0.66 g/m^3 for T22. For T26 we can see that before this rapid rise in ice rate, the LWC was varying from 0.20 - 0.40 g/m^3 between 01.05.2017 - 03.05.2017, and between 0.0 - 0.35 g/m^3 between 03.05.2017 - 04.05.2017. However for T22 we can see that the LWC was varying between 0.0 - 0.25 g/m^3 between 01.05.2017 and 02.05.2017, before it stayed low until the rapid increase. This is reflected on the ice rate in figure 4.31, where it varies for T26 in the time before the rapid increase, on the 4th of May at 07:00, while for T22 the ice rate is only non-zero between the 01.05.2017 and 02.05.2017, until the increase on the morning of the 4th of May.

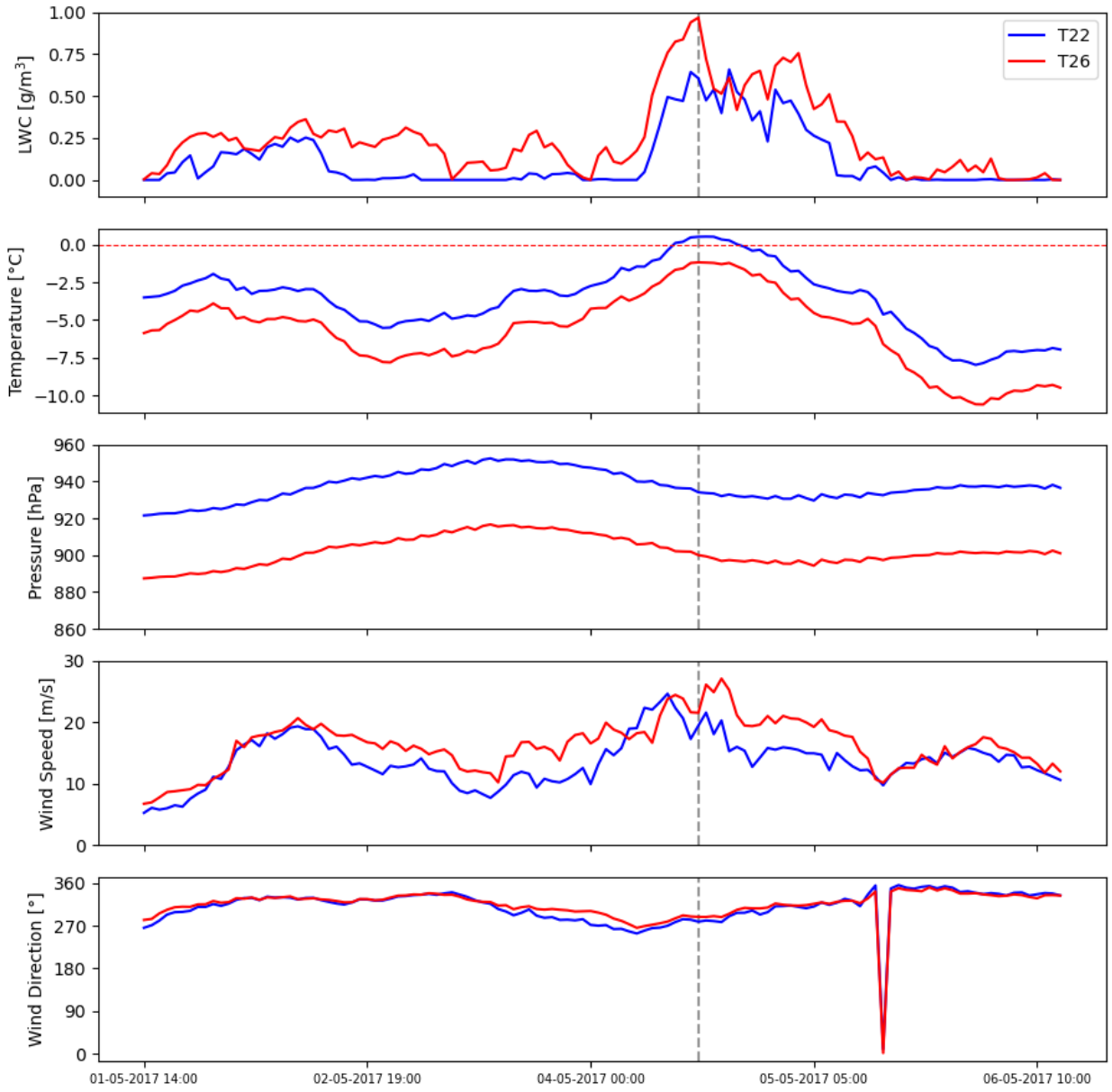

Figure 4.32: Wind speed, LWC, temperature and pressure for turbine T22 (blue) and T26 (red) during ice event 'Red'

The temperature is shown in the second row, we can see it is steadily increasing from the 02.05.2017 - 05.05.2017 for both turbines, however for turbine T22 it exceeds 0°C, and again we can see that reflected by the sudden dump in icing rate.

Third row show the air pressure, unsurprisingly the location with the greatest altitude have the lowest pressure. The pressure varies slightly and is highest before and decreases during the event.

Fourth row is showing wind speed and fifth row wind direction, we can see high wind already from the 02.05.2017 and onwards with winds reaching 27 m/s during the active icing event. Wind direction consistently coming from north-east, with small periods from west-north-west and north-north-west. For identify which direction the ice is originating from, figure 4.33 is showing icing rates and wind direction of periods when ice rates exceeds 10 g/h. We can observe that the greatest icing rates originates from west-north-west for turbine T26 and west for turbine T22. This is understandable as there is coastal areas to the west and north of the planned area. The wind could collect moist marine air and send it inland towards the park.

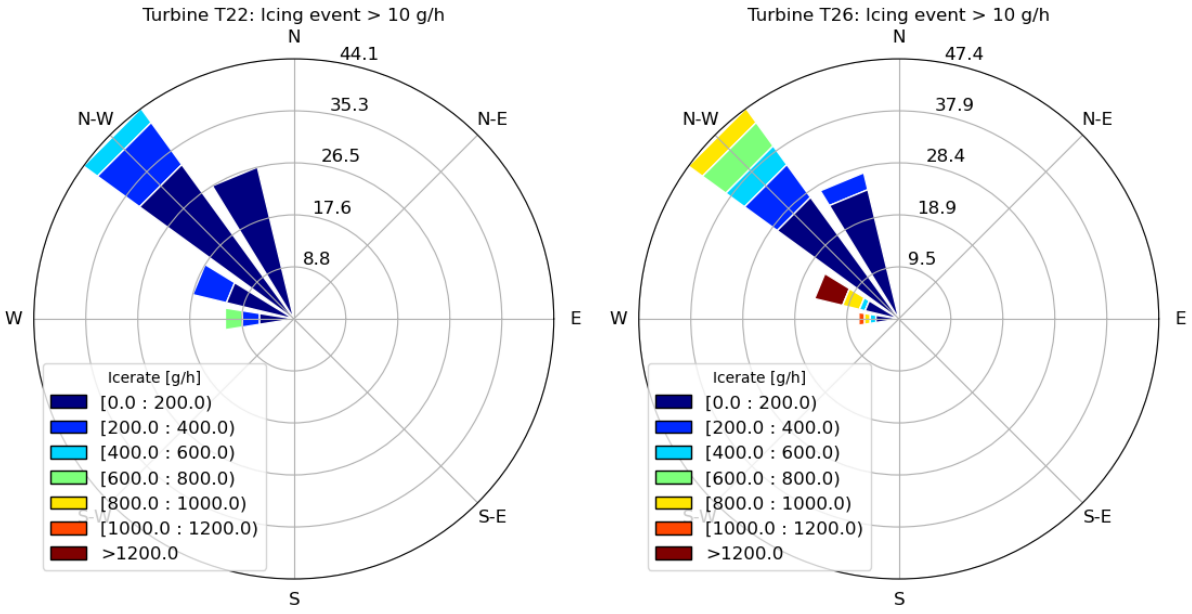

Figure 4.33: Wind rose showing wind direction and icing rates for period when icing rates are above 10g/h. Left: Turbine T22. Right: Turbine T26.

04.05.2017 14:00

Figure 4.34 shows the results inside domain 3 at the time of the peak of icing rate for turbine T26, as indicated by the vertical line in figure 4.31 and 4.32. This occurs at 14:00, on the May 4th, and by looking at the ice rate on the top left we can see that T26 have almost 1400 g/h, while T22 has none. This can be explained by looking at the figure in the bottom left, where color is showing LWC and red contour lines show temperature. Here we can see that T22 have above o^{o} C, and is therefore experiencing no icing.

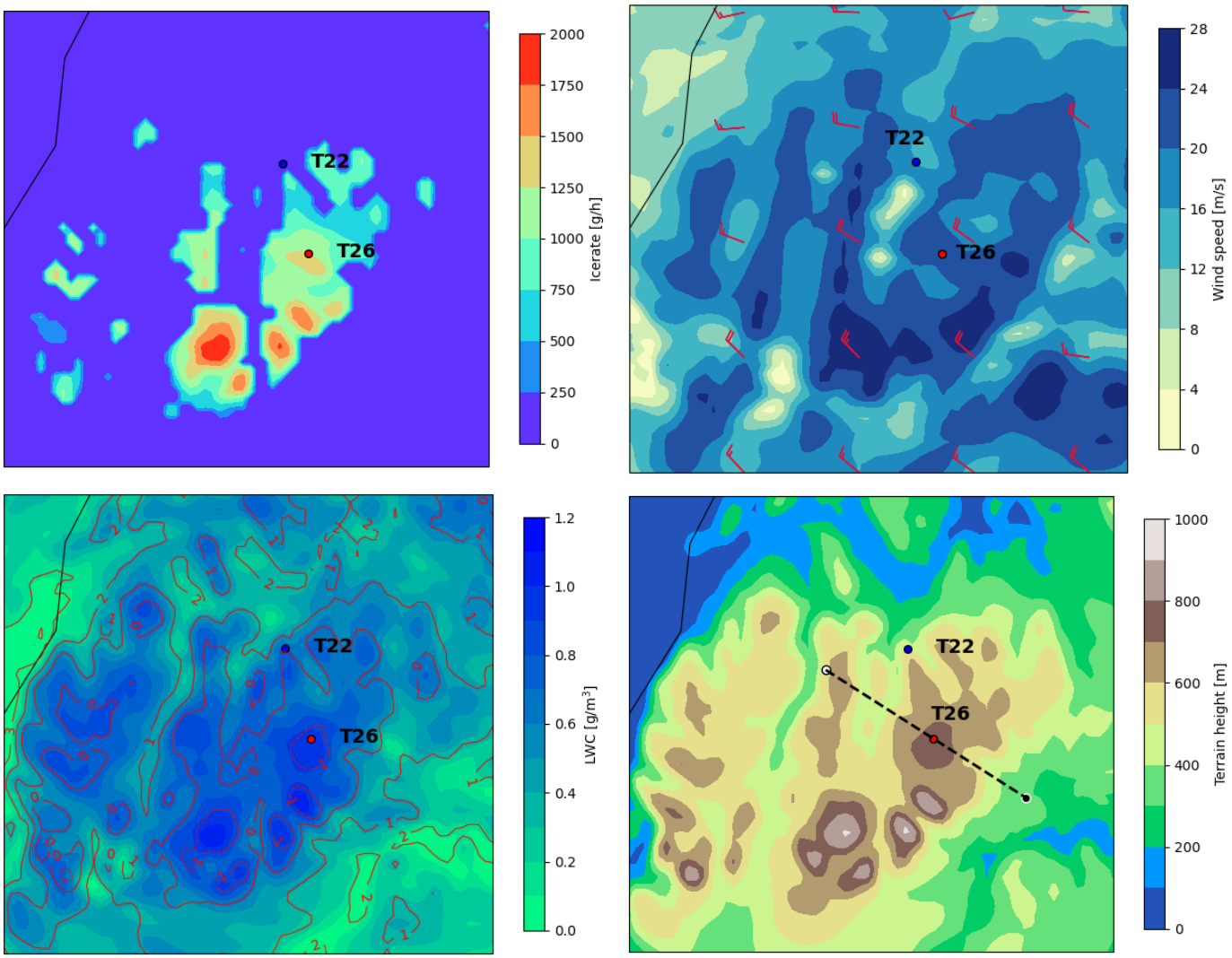

Figure 4.34: Map showing ice rate (top left), wind speed (top right), LWC (bottom left) and cross-section map (bottom right) over the area at the time 04.05.2017 10:00.

Top right figure is showing wind speed indicated by the colors and wind direction shown by the red wind barbs. Here we can see strong wind speed of between 20-24 m/s for T26 and between 16-20 m/s for T22 from north west direction. Bottom right show the terrain height and a dotted line which indicate the cross section of the vertical plot in figure 4.35, with the start indicating by white dot and end point indicated by a black dot. To be able to see how the wind affect the icing event, the cross section goes along the wind direction.

In figure 4.35 the LWC is indicated by the background color and has its highest value close to the surface. Going upwards in altitude, we can see that LWC goes to zero and relative humidity indicated by the yellow line goes from 90% around 1200 amsl to 30% around 2000 amsl. Temperature shown by the red line contour line show cold air in the upper part of figure, and then we see some pockets of warmer air in the mid altitudes before it is colder at the surface.

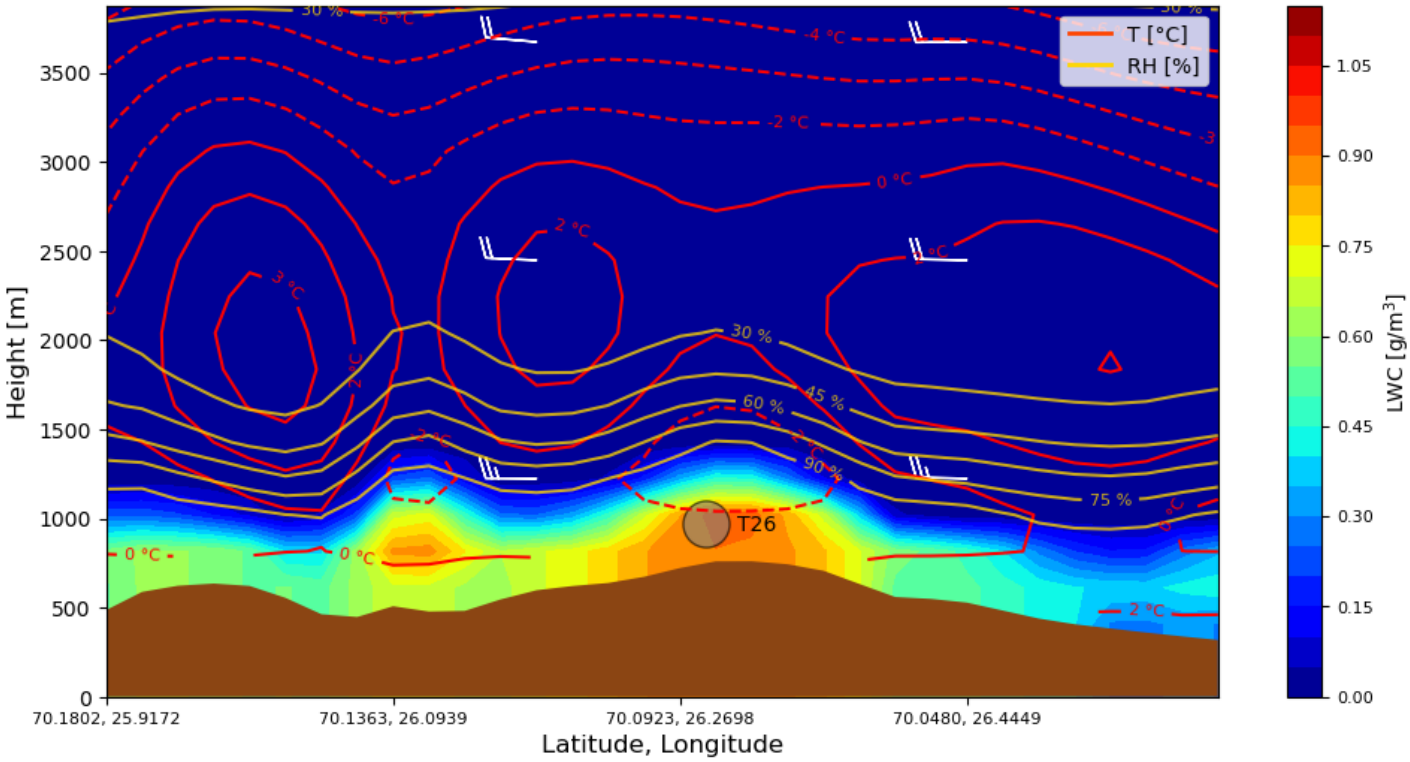

Figure 4.35: Vertical plot showing LWC (background color), relative humidity (RH, yellow), temperature (T, red) and wind (white barbs).

The circle is indicating the position and size of the spinning rotor blade for T26, here we can see that it is just high enough in the terrain so that the temperature

is below freezing, and is located in a very humid area, with LWC close to 1 g/m^3. The high LWC could explains the extreme icing we can see for this time step. However, small changes in temperature will have great impact on the icing, since it is so close the freezing point.

Synoptic chart

Synoptic charts showing surface pressure can be used to identify large weather patterns. Figure 4.36 show the synoptic chart for 04.05.2017 on the left and for 05.05.2017 on the right. Letter H and L indicate high pressure systems and low pressure systems respectively, with the contour lines showing the constant pressure. Black lines with half circles showing warm weather fronts and lines with triangles show cold weather fronts, lines with both half circles and triangles show occluded front, meaning cold weather front has catches up with a slower moving warm weather front and pushed the warm weather up.

On 04.04.2017 the high pressure system is centered at the coast of Norway, it is located between two low pressure systems, one off the coast of Greenland and the other in central Europe. Due to the clockwise rotation for high pressure systems, air is moved from the Norwegian Sea to the coast of Norway. A warm weather front is moving from west towards east towards the coast of Norway. On the 05.05.2017 the high pressure system moves west into the Norwegian Sea, and we can see a higher pressure gradient over the coast of northern Norway. The warm weather front is followed by a cold weather front and passes Davvi wind farm. This could explain the rapid rise in LWC we see between the 04.05.2017-05.05.2017.

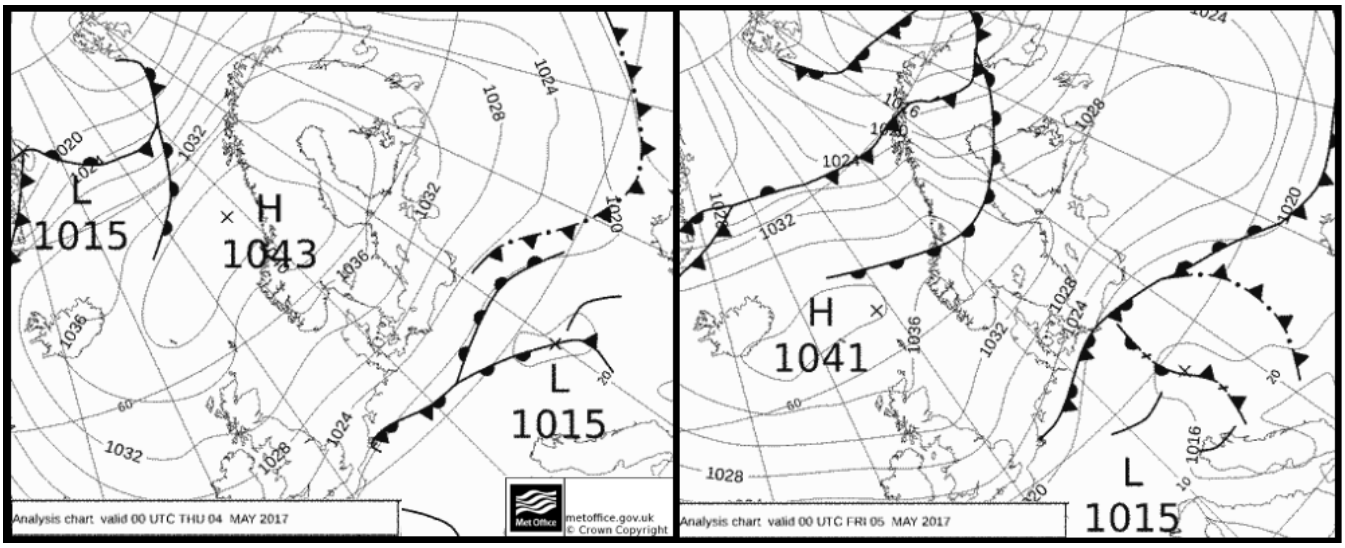

Figure 4.36: Synoptic chart over northern Europe for the ice event. Left: chart for 04.05.2017. Right: chart for 05.05.2017 [Wetterzentrale, 2024].

Icing event: Purple (01.06.2017 - 05.06.2017)

Ice event purple is the longest continuous event where the icing rate were non-zero. While this event didn't see the highest of ice rates, it is an interesting event as ice load can build up over time. Figure 4.37 show the ice rate for T26 (red) and T22 (blue). Here we can see that the ice rate was non-zero in 86 continuous hours for turbine T26, going from 01.06.2017 16:00 to 05.06.2017 06:00, and 62 hours for T22, from 02.06.2017 15:00 to 05.06.2017 05:00.

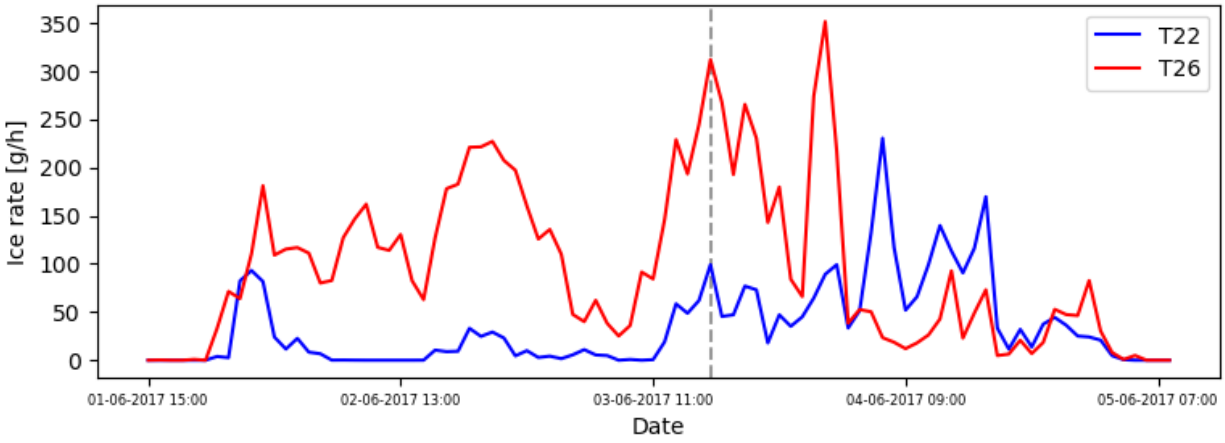

Figure 4.37: Ice rate for turbine T22 (blue) and T26 (red) during the ice event.

The LWC in the first row in figure 4.38 showcase a continuous moist weather pattern for the entire period, we can see that turbine T22 experience a period of dry air passing on the 02.06.2017, which explains the shortened ice event compared to T26.

In the second row we can see the temperature are fairly stable for the first half of the event, before the temperature increase about 3 degrees, then decrease again. We can see that the pressure shown in the third row is stable during the event, this could indicate stable weather and could explain why this icing event went on for so long as it did.

Fourth row show the wind speed, here we can observe a steady wind speed around 13-15 m/s for long period of the event, at the end we can see a the wind speed slow down. Looking at wind direction in the last row, we can see that the drop of in wind speed could relate to the fact that the wind direction change. For most of the period the winds come from the northern direction, before changing to more westerly winds between the 04.06.2017 and 05.06.2017. This icing event does not contain a single time step that is of more interest, the

interesting thing about this event is the duration and stability of the event. But we will look further into time indicated by the grey dotted line, time step at 03.06.2017 16:00.

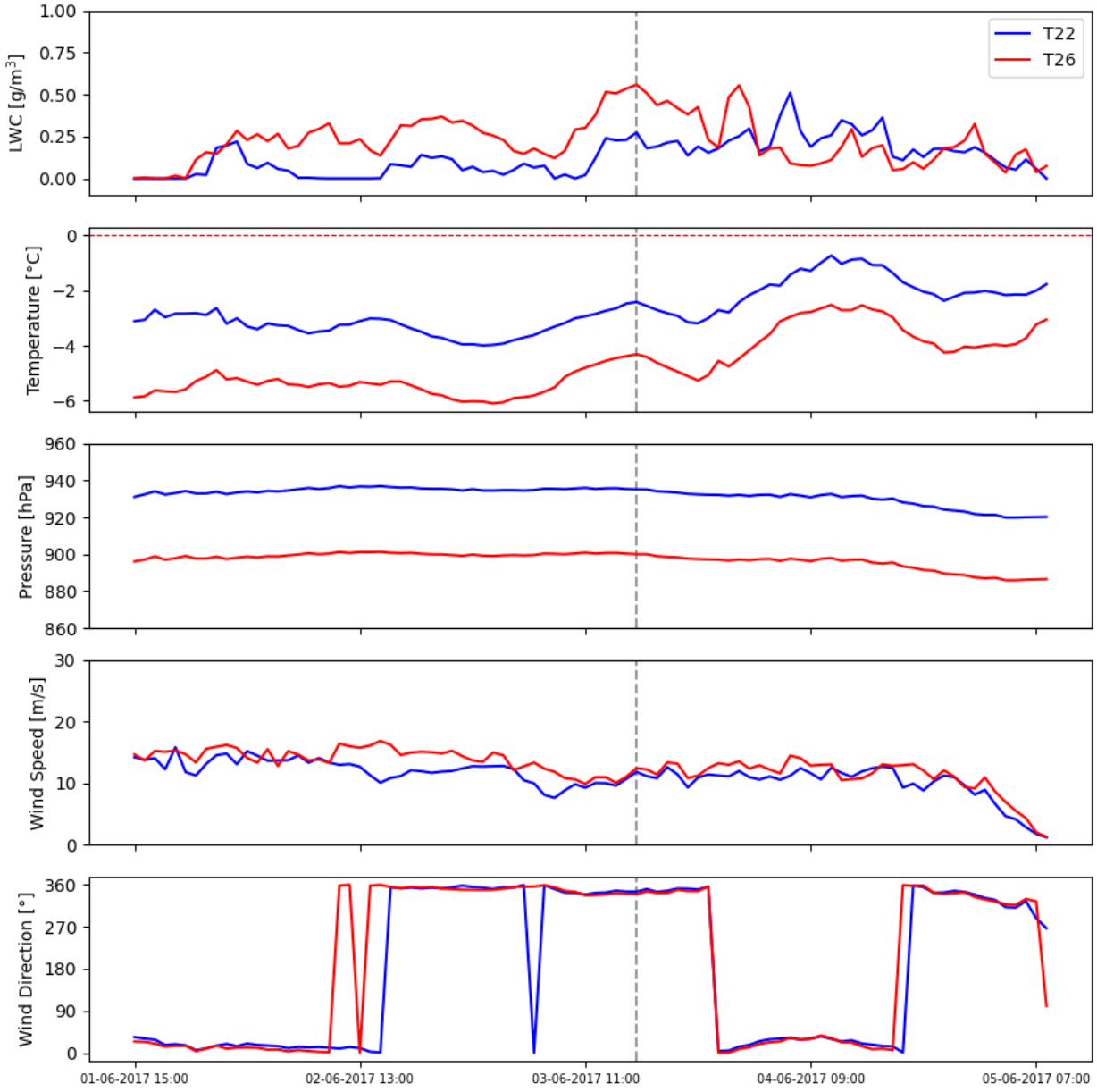

Figure 4.38: Wind speed, wind direction, LWC, temperature and pressure for turbine T22 (blue) and T26 (red) during ice event 'Purple'

The wind roses in figure 4.39 show that T26 is experiencing the greatest icing

rate from north, while T22 have the highest icing rate from the north-north-east direction. We can observe this when looking at ice rate in figure 4.37 and wind direction plot in figure 4.38. T26 have the highest amount of icing and ice rate when the wind originates from north, while T22 have high icing on the 04.06.2017 when the wind comes from north-north-east.

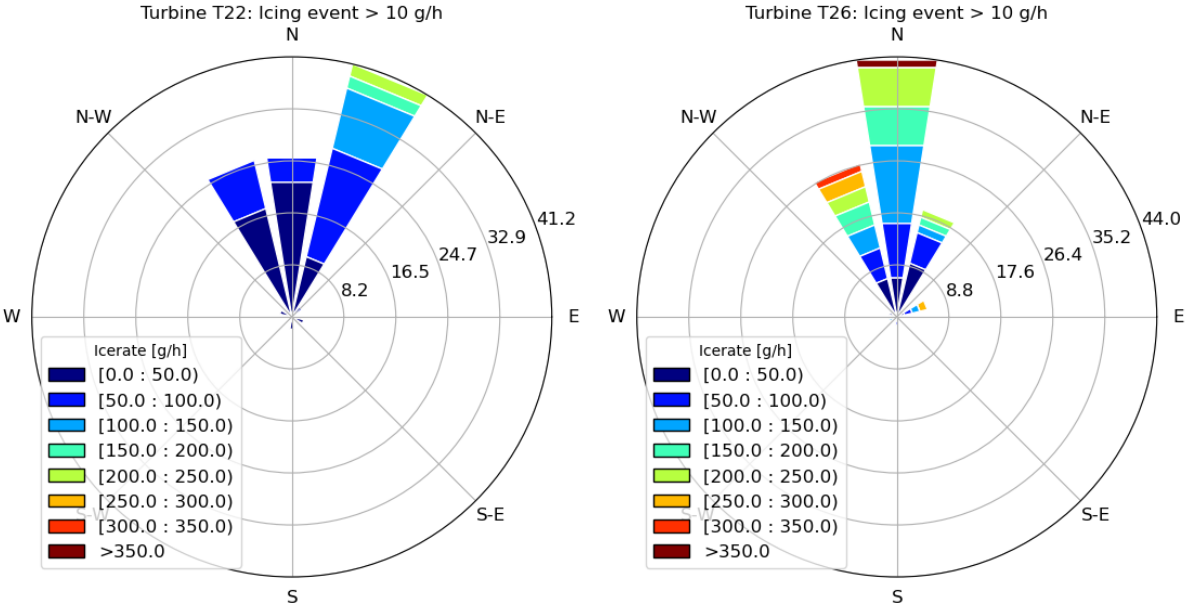

Figure 4.39: Wind rose showing wind direction and icing rates for period when icing rates are above 10g/h. Left: Turbine T22. Right: Turbine T26.

03.06.2017 16:00

This event is the longest continuous ice event, we have therefore chosen a time step near the middle of the event with high ice rates for both locations to get an idea of what occurred. The ice rate for the time 03.06.2017 16:00 is shown top left in figure 4.40, here we can see that both locations experience icing, with T26 about 300 g/h and T22 about 100 g/h.

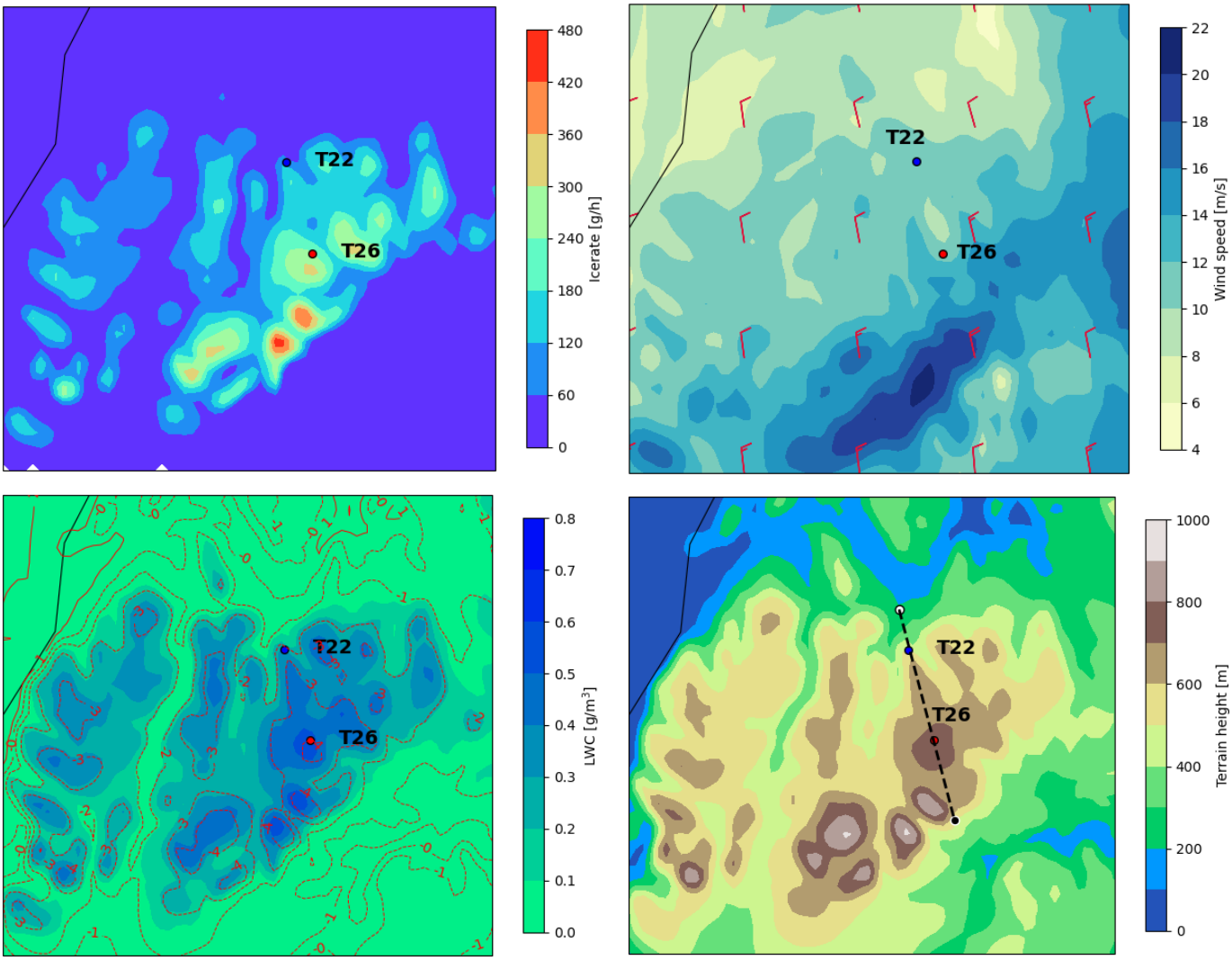

Figure 4.40: Map showing ice rate (top left), wind speed (top right), LWC (bottom left) and cross-section map (bottom right) over the area at the time over the area at the time 03.06.2017 16:00

From the wind speed and direction, shown in upper right plot, we see a

relative low wind speed for both locations, with about 12 m/s coming from the north-north-west indicated by the wind barbs. Bottom left show the LWC and temperature, we can clearly see that the moist air follow the terrain, where terrain high in altitude experience more LWC than lower terrain. This is also true for our two locations, T26 has a LWC around 0.6 g/m^3 while T22 only have about 0.25 g/m^3. Cross section plot in the bottom right show that we get a line through both locations when wind direction comes from north-north-west.

The white wind barbs in the vertical plot in figure 4.41 show that the wind goes along the cross sections line. The red dotted lines show the constant temperature for different heights, here we can see a clear temperature gradient, going from warmest near the surface to coldest in the high altitudes. Interestingly we can follow the contour lines for -4^o C, it holds relative constant height of about 1000m from left to the start of the lee side of the mountain, where it jumps to about 1700m, this could indicate that the air are warming on the lee side of the mountain.

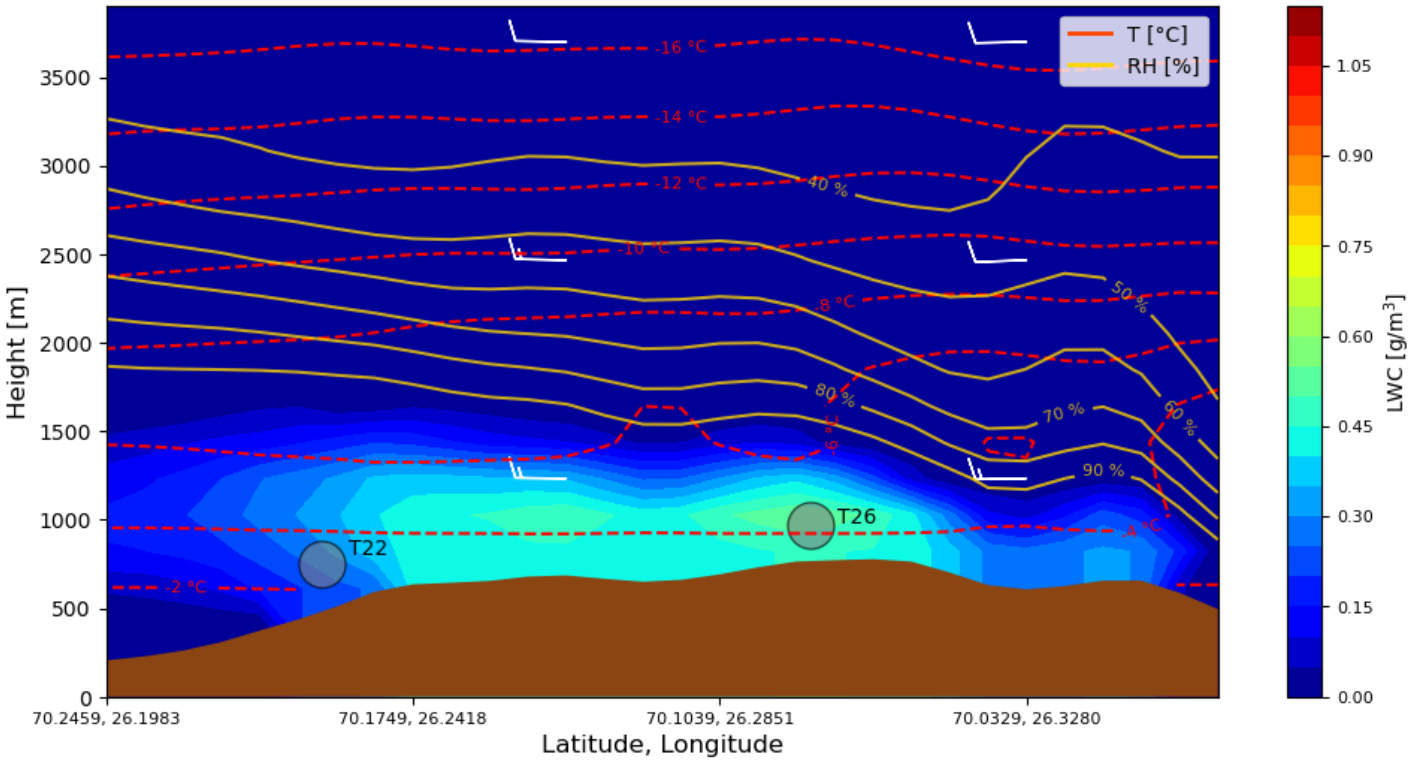

Figure 4.41: Vertical plot showing LWC (background color), relative humidity (RH, yellow), temperature (T, red) and wind (white barbs).

The yellow lines indicate the relative humidity, here we can see to the left in the plot that the constant relative humidity is much higher than to the right. About the same location where the air temperature rises, we can see a fall of in terms of relative humidity, which also could indicate warming of air on the lee side of the mountain. The circles are indicating the location and spinning rotor size of turbine T22 and T26. T22 experience higher temperatures than T26, since it is located at lower altitude. T26 also has a higher LWC due to its location in the terrain.

Synoptic chart

When looking at the left chart in figure 4.42, we can see two high pressure and two low pressure systems on the 02.06.2017. One low pressure system is located in the western part of Russia and the other in the middle of the North-Atlantic. While the high pressure systems is of the coast of northern Norway and eastern Europe. The clock-wise direction for high pressure system is consistent with the northern wind direction we can see over the Davvi-area. Right chart show the synoptic chart for 04.06.2017, and we can see that the high pressure system in eastern Europe is moving north east and a low pressure system is now sitting in eastern Europe. While the low pressure and high pressure system in the North Atlantic and the Norwegian Ocean are still in the same area. We can see an occlusion front coming from north-east, which is consistent with the increase in temperature during this time in the simulation.

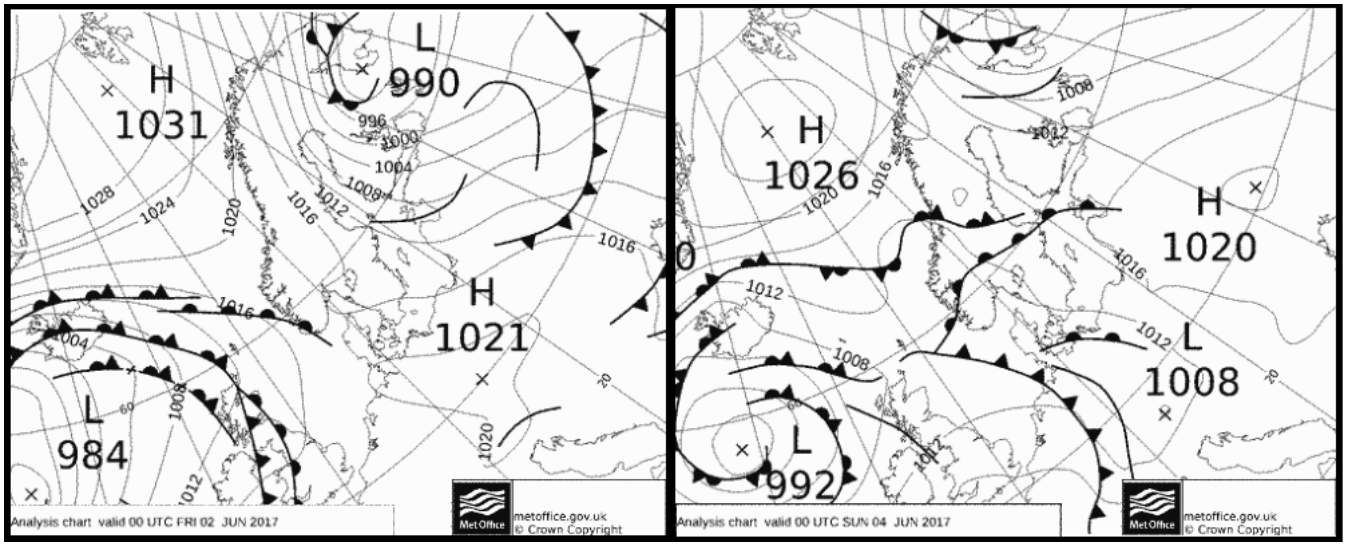

Figure 4.42: Synaptic chart over northern Europe for the ice event. Left: chart for 02.06.2017. Right: chart for 04.06.2017 [Wetterzentrale, 2024].

Icing event: Yellow (08.09.2017 - 16.09.2017)

Icerate for icing event during 08.09.2017 - 16.09.2017 is plotted in figure 4.43 for turbine T26 (red) and T22 (blue). We can see that T26 has three icing rate peaks before the 12th of September, while T22 only have one peak on the 14th of September. This icing event is interesting as the wind direction during icing event is different from the two other events.

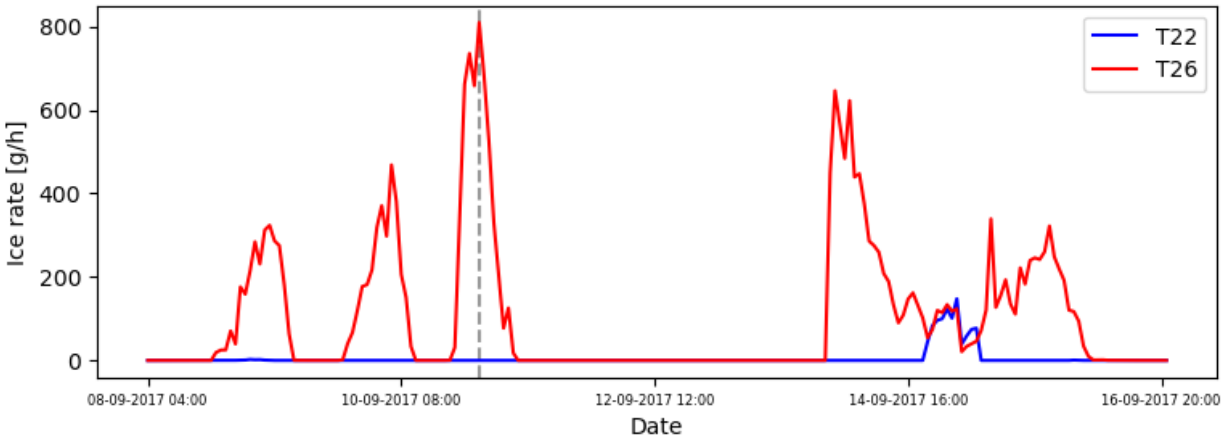

Figure 4.43: Icerate for turbine T22 (blue) and T26 (red) during the ice event.

LWC is plotted in the first row of figure 4.44, we can see almost cyclonic periods with humid air for turbine T26, while T22 experience somewhat more dry air, especially during the first section of the event. For T26 we can see that the first three LWC spikes is consistent with the same period of heavy icing, while the last spike before 12.09.2017 is occurring while the temperature is above 0^{o}C, and therefore no icing.

In the second row we can observe the temperature for the ice event, here we can see large variation where the temperatures dips below zero and up again multiple times for turbine T26, however for T22 it is above 0 ^{o}C for large period of the event, dipping under in only three occasions. For turbine T22 we can see that the first and last times the temperature falls below freezing, not enough humid air is present to start icing, while during the second period in 14.09.2017 it drops below freezing while humid air i present, and icing occurred.

Third row of figure show the air pressure for both turbines, we can observe fairly steady pressures about 900 hPa and 930 hPa for T26 and T22 respectively.

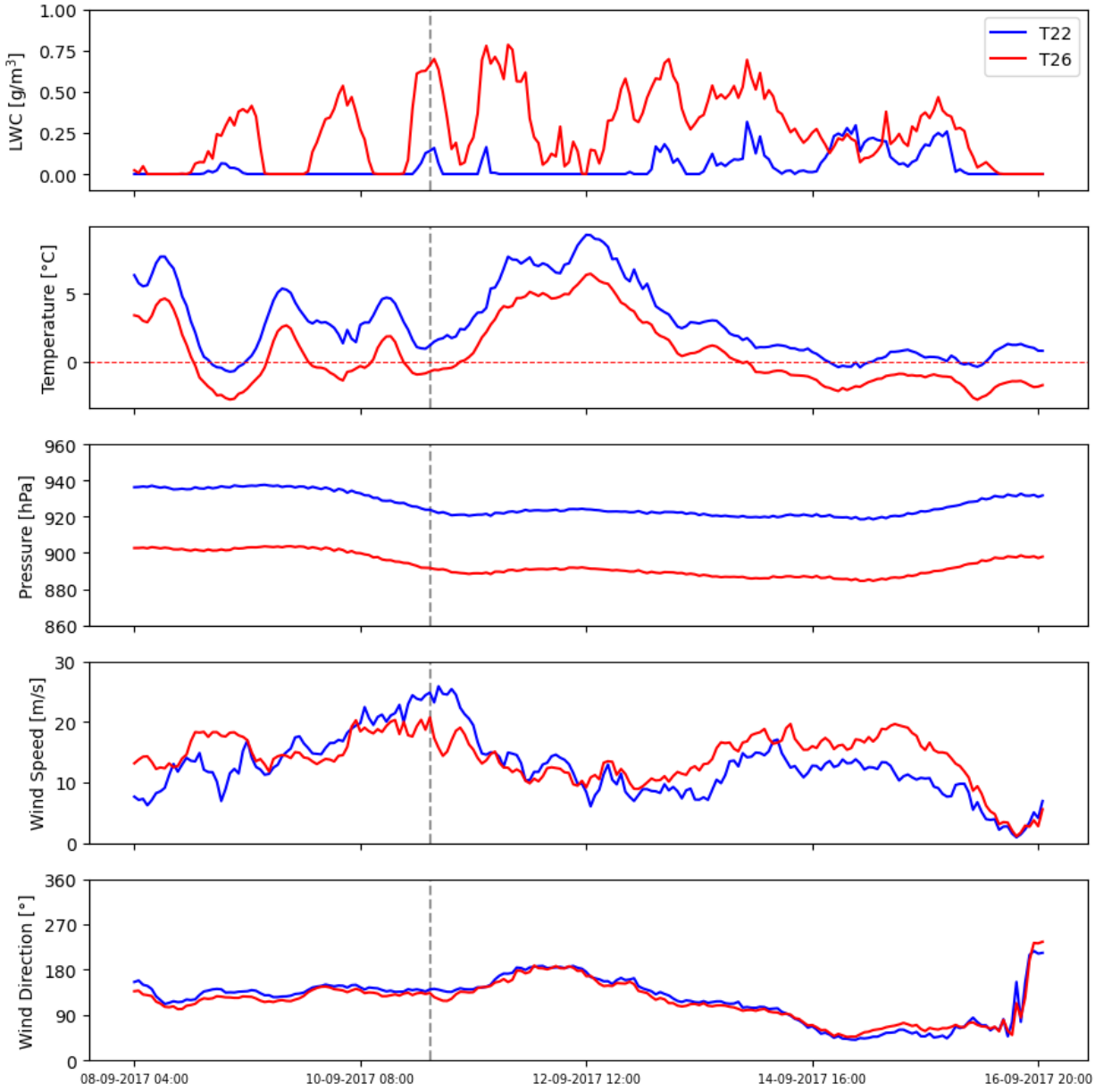

Figure 4.44: Wind speed, wind direction, LWC, temperature and pressure for turbine T26 (red) and T22 (blue) during ice event 'Yellow'.

Fourth row show wind speed and fifth row show wind direction, blue lines for T22 and red for T26. We can see that the period experiences strong winds up to about 25.9 m/s at the most. The direction of the wind is coming from south-east in the first half of the period, for the second half it changes gradual to a north-east direction.

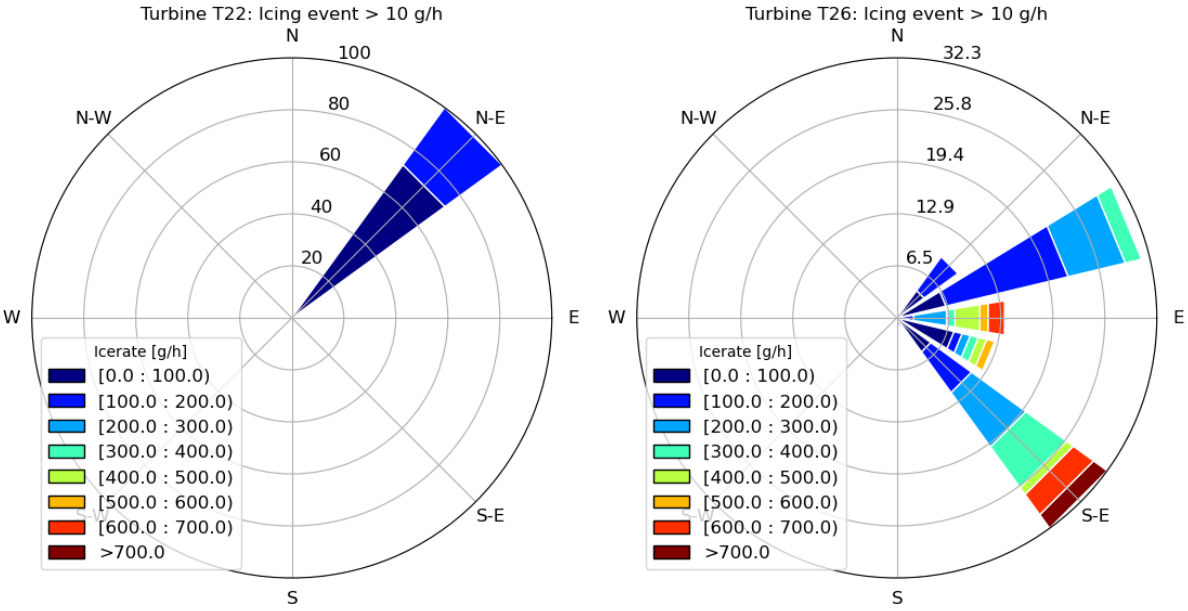

Figure 4.45: Wind rose showing wind direction and icing rates for period when icing rates are above 10g/h. Left: Turbine T22. Right: Turbine T26..

Wind roses shown in 4.45 show that T26 experienced heavy icing from south-east and east and some lighter icing from north-east, while T22 only experienced icing from north-east during this icing event. This illustrates that two locations in relative close proximity to each other can experience the same event very differently.

11.09.2017 00:00

This icing event was chosen because of the wind direction from south-east, we will take a closer look on a time step where wind comes from south-east and with peak icing rate, which occurred 11.09.2017 00:00. Looking at the ice rate map, top left in figure 4.46, we can see that T26 experience around 800 g/h, while T22 has no icing.

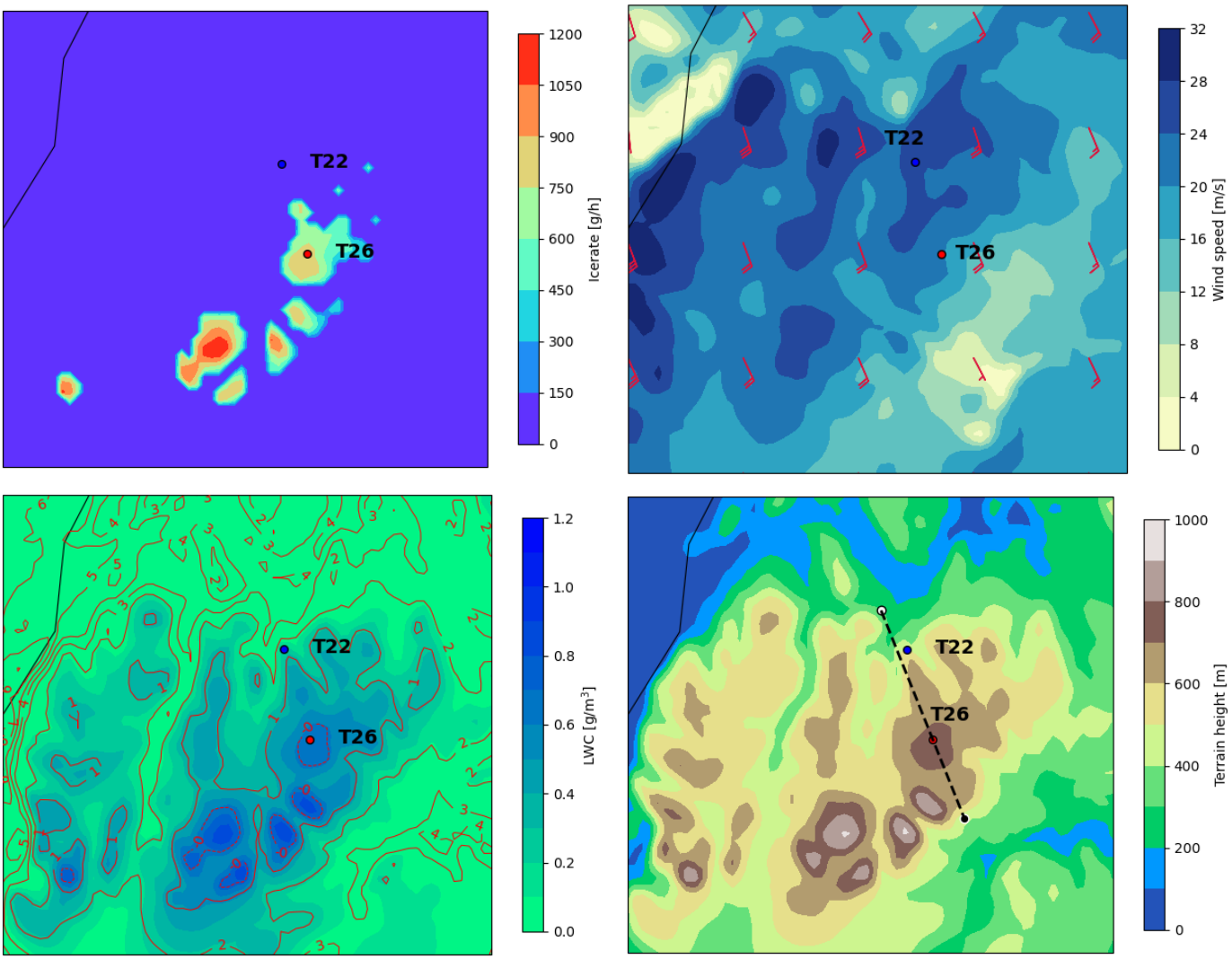

Figure 4.46: Map showing ice rate (top left), wind speed (top right), LWC (bottom left) and cross-section map (bottom right) over the area at the time over the area at the time 15.09.2017 02:00

This time step is similar to the time step for ice event 'Red', in the sense that

T26 has high icing and T22 has no icing because of temperature difference in the terrain. Bottom left show LWC and temperature, here we can see that T26 has below freezing temperatures, while T22 has 2 ^{o}C.

Top right show wind speed and direction, here we can see the wind coming from south-east with speeds around 20 m/s for T26 and 25 m/s for T22. With wind direction from south-east, T22 is on the lee-side of the mountain, which could explain the higher wind speed further down in the terrain. Bottom right we can see the cross-section line goes through the location of T26 against the wind speed.

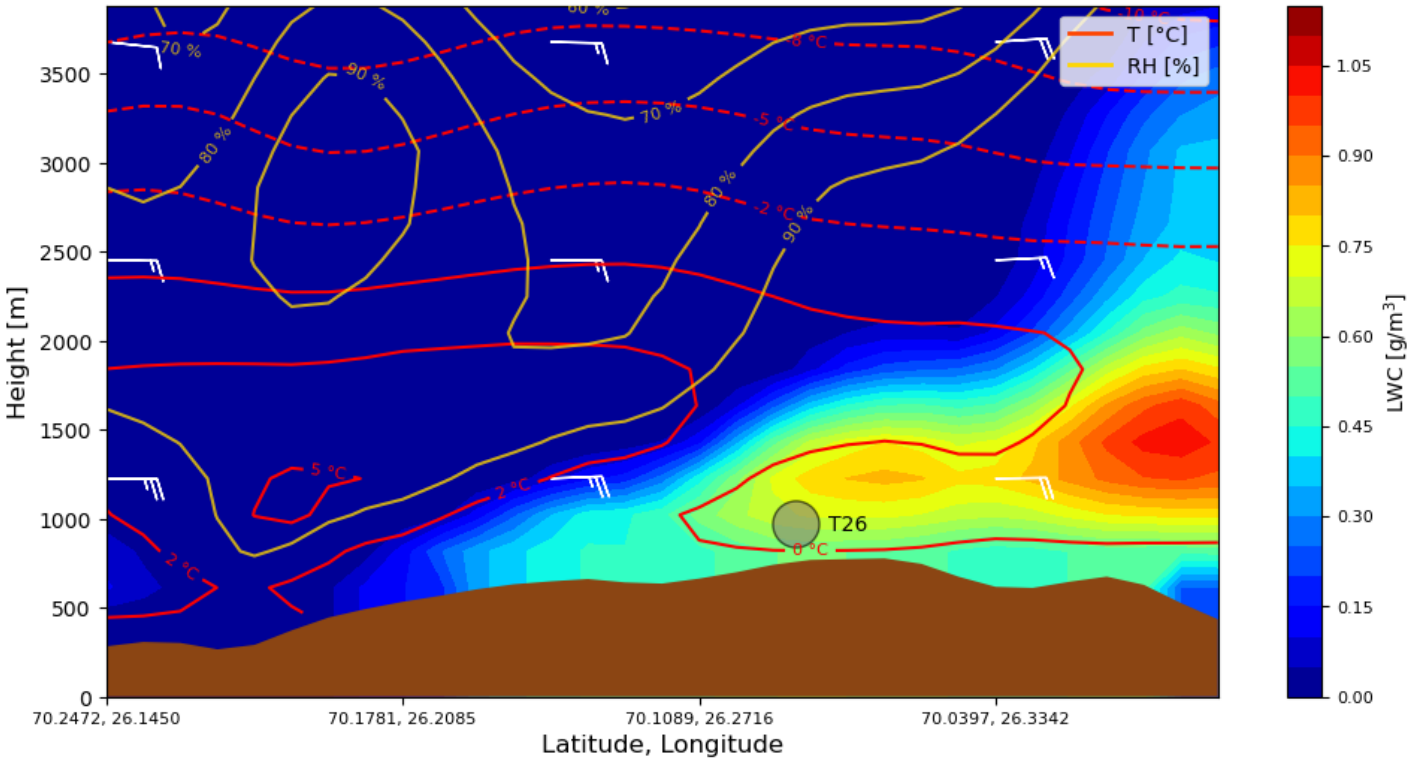

Figure 4.47: Vertical plot showing LWC (background color), relative humidity (RH, yellow), temperature (T, red) and wind (white barbs).

Vertical plot in figure 4.47 show very moist air being transported by the wind from the right towards the left. Yellow line indicating relative humidity, show that turbine T26 is inside the 90% contour line. Red line show the constant temperature contour, here we can see that the location for T26 is just above the terrain threshold for where the temperature switches from positive to negative degrees. The white wind barbs show that the wind accelerate as it moves down the terrain.

Interesting part of this event is that the high elevation of the moist air to the right in the plot. This could be explain by orographic lifting, where air masses are forced upwards because of topography of the terrain.

Synoptic chart

To the left in figure 4.48 is the synoptic chart for 10.09.2017, we can see two low pressure systems, one of coast of Norway and one on the boarder between Norway and Sweden while we can see two high pressure systems to the east, one in Russia and the other in the Balkans. We observe an occluded front, followed by two other fronts, an occluded front and a warm front, all moving north west. All the different front can explain the cyclonic pattern of temperature and moisture we can see over the area. On the 14.09.2017 we can see both low pressure systems have moved east, one in the western part of Russia and the other in one of the Baltic states. This movement has created a large pressure gradient from the coast of northern Norway going north. The anti-clockwise direction for low pressure system is driving air from the Barents Sea to the coast of Norway.

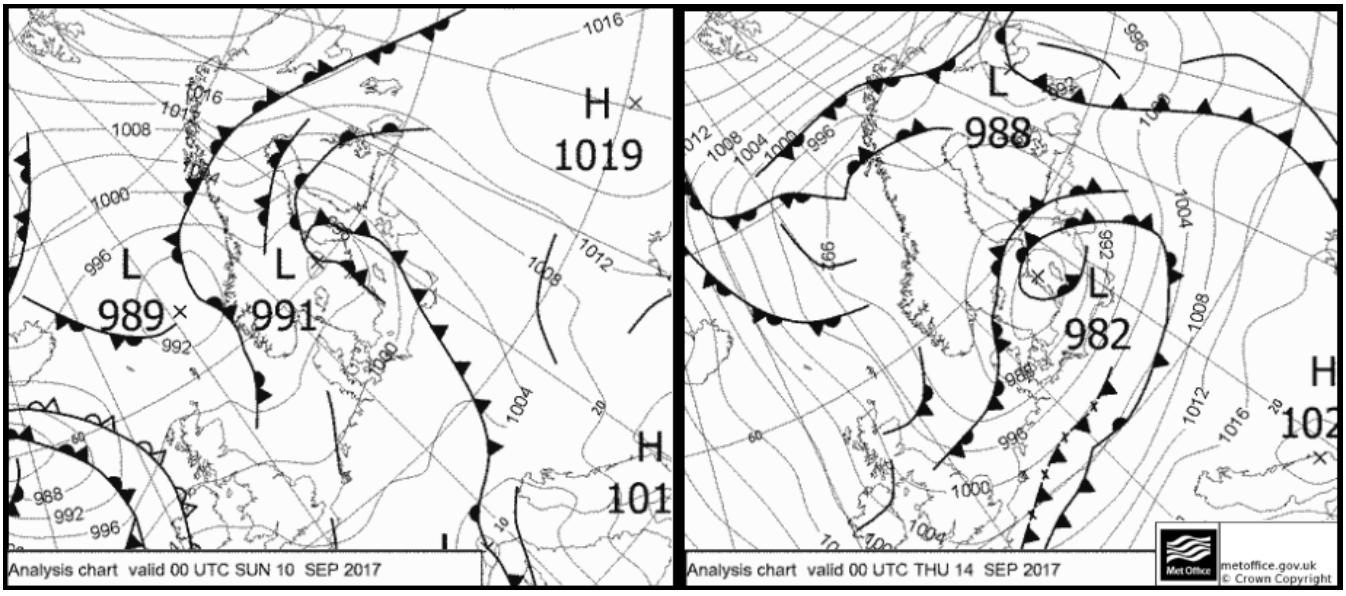

Figure 4.48: Synaptic chart over northern Europe for the ice event. Left: chart for 10.09.2017. Right: chart for 14.09.2017 [Wetterzentrale, 2024].

4.6 Wind turbine scheme impact

The difference is calculated by subtracting the value for the data without wind turbines with the value for the data with wind turbines included. Meaning positive values indicate lower values for the dataset with wind turbines included. In figure 4.49 we can see on the annual mean wind speed difference on the top left. The darker the color to bigger the difference between a simulation with turbine and without turbine. What we see is that the turbine on the outer edge of the wind park is seeing a smaller annual difference than the ones in the middle of the wind farm.

Top right we see the annual mean temperature difference, here we can see the same pattern. Turbines on the outer row see less difference than turbines in the middle. However, we can see that the difference is very small and would not make a serious impact on icing.

Bottom left is the difference in icing hours above the ice rate threshold of 10 g/h, we can see a clear relation between wind speed difference and icing hours difference. Turbines on the outer edge see far less difference than turbines in the middle, where the largest difference is 113 hours. Turbine location T32, indicated by green square, has a positive difference of 76 hours with icing rates above 10 g/h, this correspond to about 6.27% reduction in icing hours by including wind turbine scheme for this location. We can also see that turbine location to the far south-west, indicated with blue color, actually see 1 hour less without turbines.

Bottom right show the difference in icing hours above 250 g/h, where we can see that the turbines in the middle and some in the south experience greater amount of icing hours without turbines in the simulation. We can see that some location show negative values, indicating that some location have greater icing hours with wind turbines included.

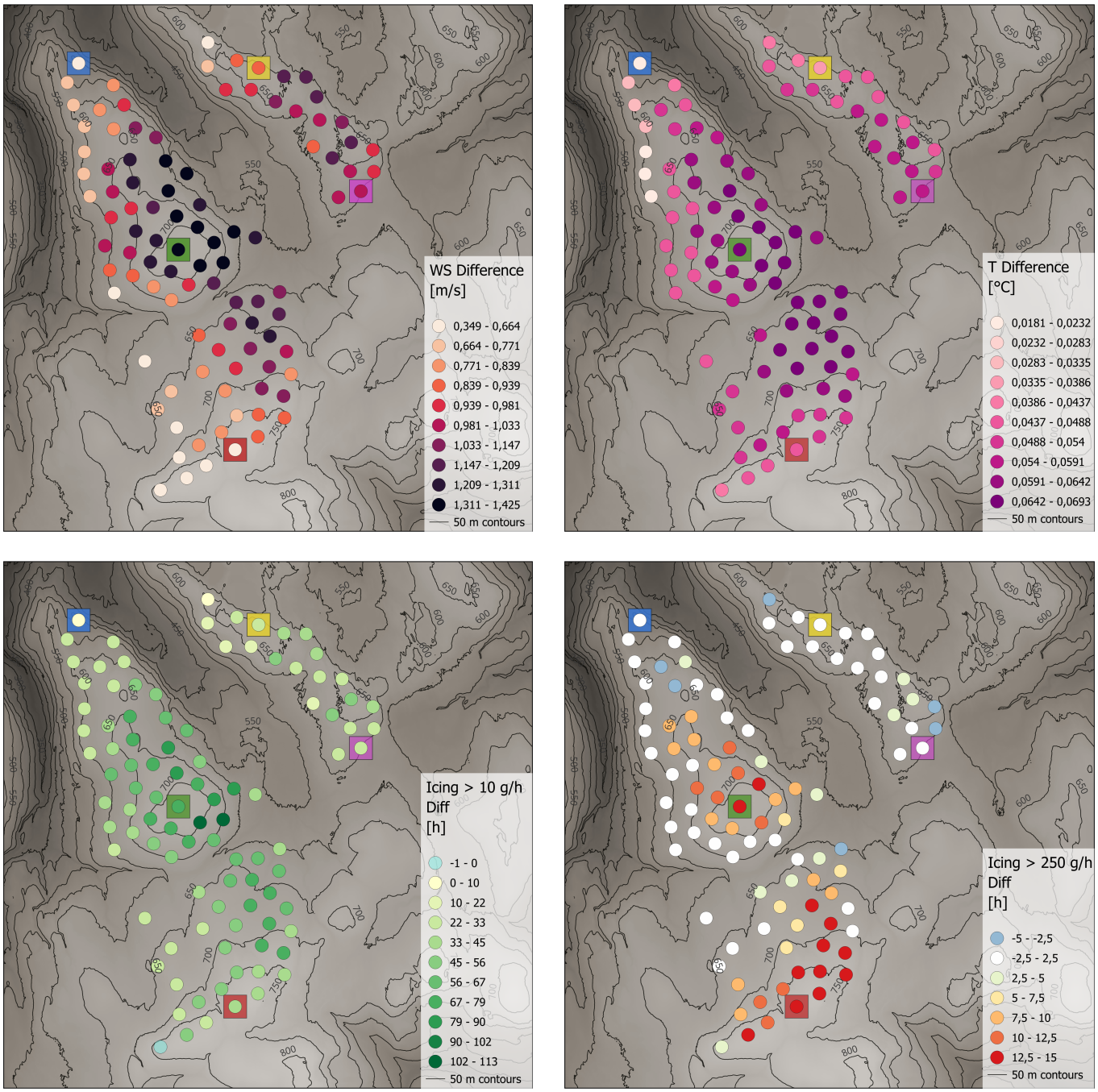

Figure 4.49: Top left: Annual mean wind speed difference. Top right: Annual mean temperature difference. Bottom left: Icing hours > 10 g/h difference. Bottom right: Icing hours > 250 g/h difference.

To show the impact of wind turbines, we have plotted the deviation in wind speed and ice rate between the simulation without and with wind turbines. Time step of 3rd of June, 2017 at 16:00 is chosen because the wind is going through the entire length of the park, and could show the wind shadowing effect. We have taken the results without the wind turbine scheme and subtracted the results using the wind turbine scheme. Thus, a positive value indicate higher value for simulation without the scheme.

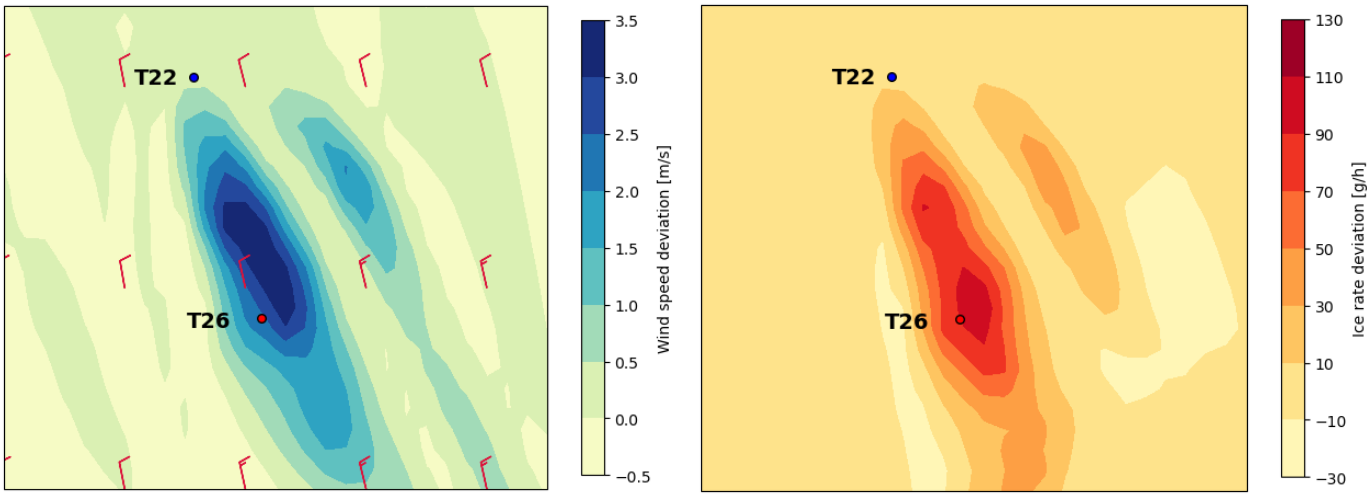

Figure 4.50: Left: Color bar showing wind speed deviation, red windbarbs showing wind direction. Right: color bar showing ice rate deviation.

The results for wind speed is shown to the left of figure 4.50. Here we can see that the area south-east of T22 is experiencing a greater difference in wind speed. This indicate the the wind speed is lower in that area for the simulation including wind turbine. To the right we can see the difference in icing rate, here we can see that the same area is showing a positive deviation in the area where the turines are located. This again indicate that the ice rate is lower in the simulation including wind turbine.

4.7 Production loss

Calculating power production based on ice load is difficult to model accurately due to the stochastic nature of ice shedding. Without ice shedding and melting the ice load would build up to unrealistic dimensions, therefore we have implemented an experimental method where we only look at ice build up during an ongoing icing period. In practice this means that for consecutive

time steps where icing rate is above zero, ice will build up and production will be reduced based on ice load. However, when the icing rate fall to zero, we 'reset' the ice load back to zero to simulate a total ice shedding. This way we can model a production based on ice load without introducing stochastic features to the method.

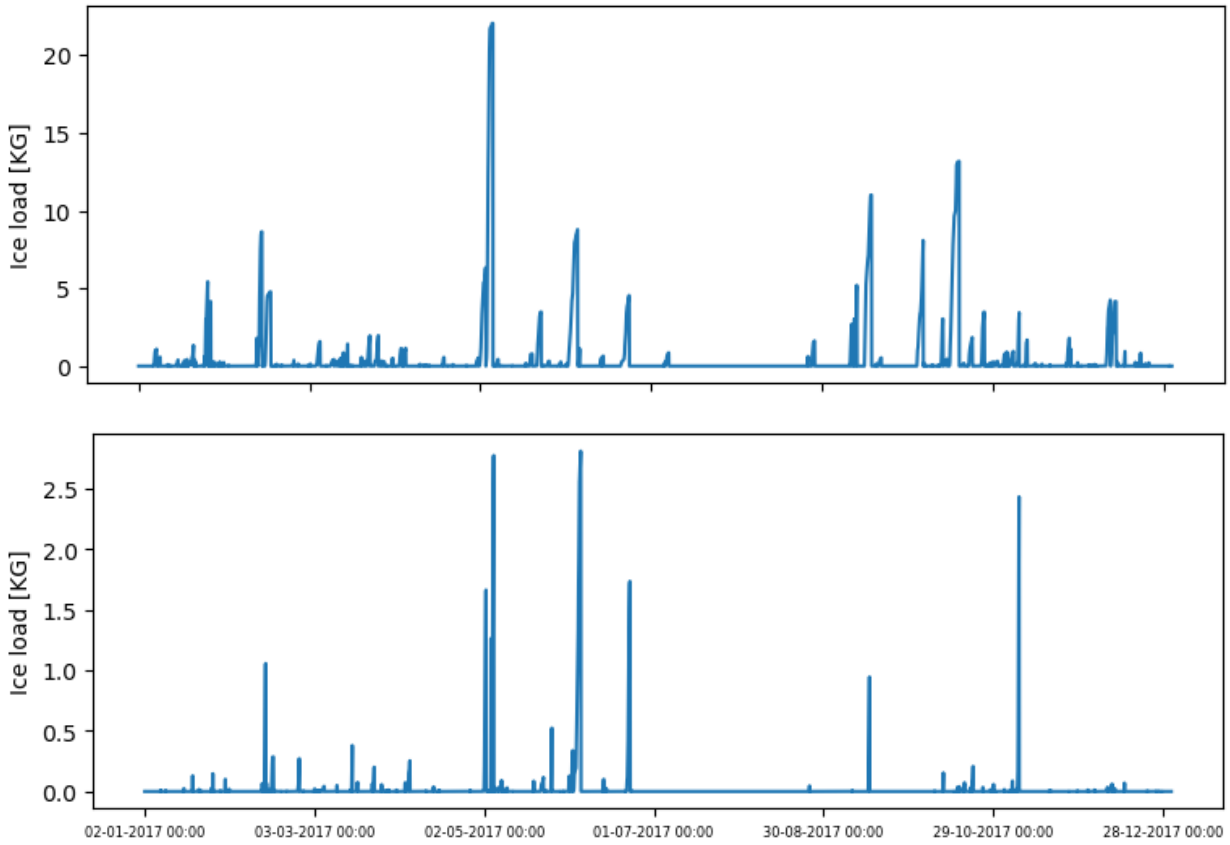

Figure 4.51: Ice load for turbine T26 (first row) and T22 (second row).

By using this method for the two turbines we looked at previously, we can look at the most extreme icing case (T26) and the least extreme icing case (T22). Figure 4.51 show the ice load during the entire simulation period. Here we can see that T26 have high build up of ice, at the most 22 kg, while T22 reached 2.8 kg at the most. Table 4.3 show the distribution of hours where ice loads exceeds the given threshold. Here we can see that T26 has ice loads above the threshold of 500 grams for 1037 hours during the simulated time period, which correspond to 11.9% of the year.

Turbine	Hours > 10 [g]	Hours > 50 [g]	Hours > 250 [g]	Hours > 500 [g]
T2	1483	1089	665	512
T22	507	324	151	105
T26	2258	1889	1358	1037
T32	1762	1353	835	644
T91	1351	1013	664	501

Table 4.3: Hours above ice load threshold of 10, 50, 250 and 500 grams for turbine location T2, T22, T26, T32 and T91

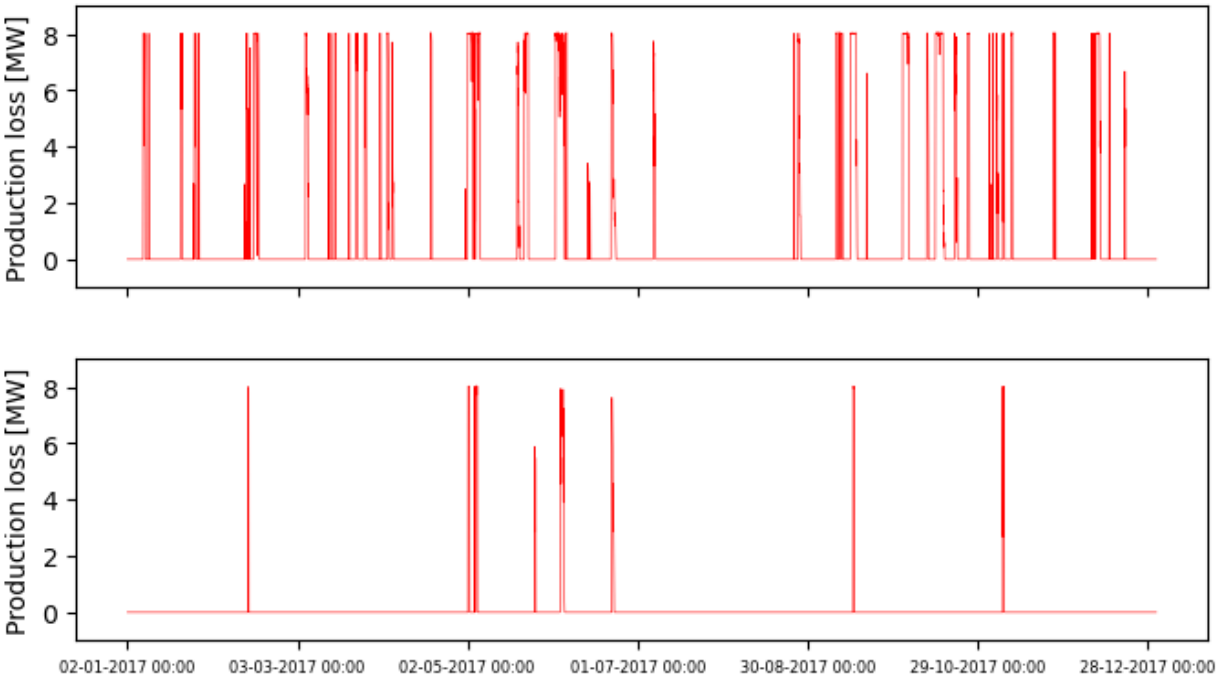

Figure 4.52: Production loss due to icing for turbine T26 (first row) and T22 (second row).

Using the power curve for ice loss shown in figure 3.14, we calculate the production loss based on ice load. To look at the affect of icing on power production we have subtracted the normal ice-free production with the iced production. Figure 4.52 show the amount of production loss due to icing for T26 (first row) and T22 (second row). We can see that turbine T26, as expected experience much more production loss than T22.

IEA Ice class in figure 3.12 tells us that a location with over 10% annual meteorological icing could expect over 20% annual production loss. T26 is

experiencing 17.75% annual meteorological icing, while T22 is seeing 3.17%. This means that T26 could expect above 20% production loss and T22 could expect between 3 - 12%. Table 4.4 show the annual production under normal and iced conditions, and also the percentage loss. Here we can see that our experimental method show slightly less production loss for highly iced location, since T26 show only 19.86% loss for 17.75% annual icing. We can also observe that the annual production loss for T22 is in the lower end of the production based on IEA ice class, with 4.16% production loss for 3.17% annual meteorological icing.

Turbine	Normal [TWh]	Icing [TWh]	Loss [%]
T2	30.57	27.44	10.26
T22	29.30	28.08	4.16
T26	35.09	28.12	19.86
T32	28.69	24.35	15.13
T91	29.68	26.13	11.96

Table 4.4: Annual production for normal condition, icing condition, and percentage production loss for turbine T2, T22, T26, T32 and T91.

4.7.1 Uncertainties

The experimental method for estimating production assumes that 100% of the ice rate is accumulated on the blade. Additionally, it assumes the loss of all ice load when the ice rate reaches zero grams per hour. This is a simplification for the estimation of the ice load to avoid introducing stochastic values for ice shedding. It is important to note that even if the ice rate reaches zero, if the temperature stays in the freezing range, the ice build up will start again when ice rate becomes non-zero.

The assumption introduce uncertainties into the estimations. The actual ice accretion process is highly variable and influenced by many factors. Over- or underestimation may be introduced when not accounting for ice shedding or intermittent ice build up.

5

Conclusion

The aim of this thesis is to look at the impact of icing on the planned location of Davvi wind farm using WRF model with wind turbine scheme. Primary goal is to assess atmospheric icing and identify weather parameters for meteorological icing on wind turbines. We estimate the annual icing intensity for 2017 at the suggested wind turbine locations and compare it to NVE's 2009 icing map. Our turbine location show higher variation and detail in icing hours, with the majority of location resulting in similar values. Terrain height is shown to influence icing severity, we see higher icing rates due to lower temperature and higher liquid water content in higher terrain. Turbine location with the highest icing severity is T26 with 1555 hours above 10 g/h, which correspond to 17.75 % annual meteorological icing. While turbine location with the least amount of icing severity is T22 with 276 hours above 10 g/h, which is 3.17 % annual meteorological icing. Using the established site ice index, shown in figure 3.18, this correspond to strong (s4) icing severity for T26, and light (s2) icing severity for T22. The WRF icing rates are not directly comparable with the NEWA's ice load results. This is due to NEWA using a more complicated IceBlade model, which give lower ice load and ice rate compared to the standard cylinder model used in this thesis.

Secondary goal is to enhance the understanding of icing estimation and weather simulation using NWP model with wind turbine scheme included in the simulation. Result shows that wind turbines positioned downstream, relative to the wind direction, experienced wake effect created by upstream turbines. The maximum annual mean wind speed difference between a location with and

without a turbine is 1.425 m/s, and the greatest difference in icing rate above 10 g/h is 113 hours. Icings maps like in NVE's 2009 report, where the wind turbine scheme is not included, could therefore expect higher icings rate than what a wind park would experience. This show the importance of including wind turbine for wind and ice siting at a location for accurate assessments. Mitigating wake effect could improve the efficiency of a wind farm layout and thereby improve decision making in the wind energy industry.

We aim to estimate the production loss based on icing load, in order to provide valuable economic insight into the icing impact of wind energy production. Our results show promising results with a slightly lower production loss compared to IEA Task 19 icing climate site classification shown in figure 3.12. According to this classification, the location of T26 with 17.75% annual meteorological icing, will expect an annual production loss of over 20%. Whereas, the location for T22 with 3.17% annual meteorological icing, will expect an annual production loss of between 3-12%. Our result show a production loss of 19.86% and 4.16%, for T26 and T22 respectively. The lower production loss is expected, as our method only looked at rime ice and assumes that all ice load is lost when ice rate drops to zero.

5.1 Further research

For proper validation of WRF results, it should be compared to measurements from the actual area. This way we could understand if there is some impact from the local terrain that increase/decrease wind or ice for a turbine. Higher resolution simulation should be also be tested, with higher accuracy of the terrain we could increase the accuracy of the simulated weather parameters.

We have calculated icing with the assumption of dry ice accretion. For higher accuracy, α_2 and α_3 should be implemented. This implementation would include wet icing, and change the estimated icing hours. We have used a fixed values for droplet concentration, for future research this value should change based on origin of air masses. This could increase the accuracy of ice accretion estimation.

The conversion between ice rate and ice load remains problematic due to stochastic nature of ice shedding. Developing a standardized method for this would greatly benefit future ice load predictions and would increase the reliability and consistency of future predictions and accuracy of power production estimation based on ice load.

Bibliography

[Alvik et al., 2023] Alvik, S., Rinaldo, M., Özgün, O., Bjørndalen, J., Fiskevik, I. H., Hadizadeh, M., Horschig, T., Ingeberg, K., Koefoed, A. L., McConnell, E., Narula, H., Romanenko, E., Ryszka, K. A., Selvakkumaran, S., Zambon, A., Zwart, R. J., Aarrestad, K., Irvine, M., and Vandbakk, A. (2023). Energy transition norway 2023. *DNV*.

[Barthelmie and Jensen, 2010] Barthelmie, R. J. and Jensen, L. E. (2010). Evaluation of wind farm efficiency and wind turbine wakes at the nysted offshore wind farm. *Wind Energy*, 13(6):573–586.

[Betz, 2013] Betz, A. (2013). *The Maximum of the Theoretically Possible Exploitation of Wind by Means of a Wind Motor*. *Wind Engineering*, 37:441 – 446.

[Bredesen et al., 2017] Bredesen, R. E., Cattin, R., Clausen, N.-E., Davis, N., Jordaens, P. J., Khadiri-Yazami, Z., Klintström, R., Krenn, A., Lehtomäki, V., Ronsten, G., Wadham-Gagnon, M., and Wickman, H. (2017). 13. wind energy projects in cold climates. *IEA Wind Technology Collaboration Programme*.

[Brotzge et al., 2023] Brotzge, J., Berchoff, D., Carlis, D. L., Carr, F. H., Carr, R. H., Gerth, J. J., Gross, B. D., Hamill, T. M., Haupt, S. E., Jacobs, N., McGovern, A., Stensrud, D. J., Szatkowski, G., Szunyogh, I., and Wang, Z. (2023). Challenges and oppertunities in numerical weather prediction. *AMS 2022 Summer Community Meeting*, page E698–E705.

[Carvalho et al., 2012] Carvalho, D., Rocha, A., Gómez-Gesteira, M., and Santos, C. (2012). A sensitivity study of the wrf model in wind simulation for an area of high wind energy. *Environmental Modelling Software*, 33:23–34.

[Chen et al., 2011] Chen, F., Kusaka, H., Bornstein, R., Ching, J., Grimmond, C. S. B., Grossman-Clarke, S., Loridan, T., Manning, K. W., Martilli, A., Miao, S., Sailor, D., Salamanca, F. P., Taha, H., Tewari, M., Wang, X., Wyszogrodzki, A. A., and Zhang, C. (2011). The integrated wrf/urban modelling system:

development, evaluation, and applications to urban environmental problems. *International Journal of Climatology*, 31(2):273–288.

[Davis, 2014] Davis, N. (2014). *Icing Impacts on Wind Energy Production*. PhD thesis, Technical University of Denmark (DTU).

[Davis et al., 2018] Davis, N., Bredesen, R. E., Lehtomäki, V., Krenn, A., Jordaens, P. J., Godreau, C., Khadiri-Yazami, Z., Ronsten, G., Wickman, H., Bourgeois, S., and Beckford, T. (2018). Available technologies for wind energy in cold climates - report. *IEA Wind*. Task 19.

[Dörenkämper et al., 2020] Dörenkämper, M., Olsen, B. T., Witha, B., Hahmann, A. N., Davis, N. N., Barcons, J., Ezber, Y., García-Bustamante, E., González-Rouco, J. F., Navarro, J., Sastre-Marugán, M., Sīle, T., Trei, W., Žagar, M., Badger, J., Gottschall, J., Sanz Rodrigo, J., and Mann, J. (2020). The making of the new european wind atlas – part 2: Production and evaluation. *Geoscientific Model Development*, 13(10):5079–5102.

[Emeis, 2018] Emeis, S. (2018). *Wind Energy Meteorology: Atmospheric Physics for Wind Power Generation*. Green Energy and Technology. Springer International Publishing AG, 2nd ed. 2018 edition.

[Farzaneh, 2008] Farzaneh, M. (2008). *Atmospheric Icing of Power Networks*. Springer Netherlands : Imprint: Springer, Dordrecht, 1st ed. 2008. edition. pp. 4-9.

[Fikke, 2005] Fikke, S. (2005). *Modern Meteorology and Atmospheric Icing*. *IWAIS 2005*.

[Fikke et al., 2007] Fikke, S., Ronsten, G., Heimo, A., Kunz, S., Makkonen, L., Wichura, B., Ostrozlik, M., Person, P. E., Sabata, J., Warein, B., Chum, J., Laakso, T., and Säntti, K. (2007). *COST 727: Atmospheric Icing on Structures. Measurement and data collection on icing: State of the Art*. *Veröffentlichung MeteoSchweiz*, (75).

[Finstad et al., 1988] Finstad, K. J., Lozowski, E. P., and Makkonen, L. (1988). On the median volume diameter approximation for droplet collision efficiency. *Journal of the Atmospheric Sciences*, 45(24).

[Fitch et al., 2012] Fitch, A., Olson, J., Lundquist, J., Dudhia, J., Gupta, A., Michalakes, J., and Barstad, I. (2012). Local and mesoscale impacts of wind farms as parameterized in a mesoscale nwp model. *Monthly Weather Review*, 140.

[Fortin et al., 2006] Fortin, G., Laforte, J.-L., and Ilinca, A. (2006). Heat and

mass transfer during ice accretion on aircraft wings with an improved roughness model. *International Journal of Thermal Sciences*, 45(6):595–606.

[Grenselandet AS, 2022] Grenselandet AS (2022). *Konsesjonssøknad, Davvi vindkraftverk i Lebesby kommune*. Technical report.

[Hersbach et al., 2023] Hersbach, H., Bell, B., Berrisford, P., Biavati, P., Horányi, A., Sabater, J. M., Nicolas, J., Peubey, C., Radu, R., Rozum, I., Schepers, D., Simmons, A., Soci, C., Dee, D., and Thépaut, J.-N. (2023). Era5 hourly data on single levels from 1940 to present. DOI: 10.24381/cds.adbb2d47. Retrieved: 30.03.2024.

[Homola et al., 2011] Homola, M., Virk, M., Nicklasson, P., and Sundsbø, P. (2011). Modelling of ice induced power losses and comparison with observations. *Winterwind*.

[Homola, 2011] Homola, M. C. (2011). *Atmospheric icing on wind turbines*. phdthesis, NTNU Norwegian University of Science and Technology.

[Hämäläinen and Niemelä, 2017] Hämäläinen, K. and Niemelä, S. (2017). Production of a numerical icing atlas for finland. *Wind Energy*, 20(1):171–189.

[Iacono et al., 2008] Iacono, M. J., Delamere, J. S., Mlawer, E. J., Shephard, M. W., Clough, S. A., and Collins, W. D. (2008). Radiative forcing by long-lived greenhouse gases: Calculations with the aer radiative transfer models. *Journal of Geophysical Research: Atmospheres*, 113(D13).

[Ingvaldsen et al., 2019] Ingvaldsen, K., Nygaard, B., Byrkjedal, , and Iversen, E. (2019). Validation of modelled in-cloud ice accretion on overhead power lines at exposed high altitude sites in norway. *IWAIS 2019*.

[Jiménez et al., 2012] Jiménez, P. A., Dudhia, J., González-Rouco, J. F., Navarro, J., Montávez, J. P., and García-Bustamante, E. (2012). A revised scheme for the wrf surface layer formulation. *Monthly Weather Review*, 140(3):898–918.

[Jin, 2021] Jin, J. Y. (2021). *Study of Atmospheric Ice Accretion on Wind Turbine Blades*. PhD thesis, UiT The Arctic University of Norway.

[Kain, 2004] Kain, J. S. (2004). The kain-fritch convective parameterization: An update. *Applied Meteorology and Climatology*.

[Kalmikov, 2017] Kalmikov, A. (2017). *Wind Energy Engineering: A Handbook for Onshore and Offshore Wind Turbines*. Elsevier Science Technology. II. Wind Resource and Wind Energy Worldwide pp.15-124.

[Lamraoui et al., 2014] Lamraoui, F., Fortin, G., Benoit, R., Perron, J., and Masson, C. (2014). Atmospheric icing impact on wind turbine production. *Cold Regions Science and Technology*, 100:36–49.

[Liu et al., 2023] Liu, H., Chen, J., Zhang, J., Chen, Y., Wen, Y., Zhang, X., Yan, Z., and Li, Q. (2023). Study on atmospheric stability and wake attenuation constant of large offshore wind farm in yellow sea. *Energies*, 16(5).

[Lutgens et al., 2019] Lutgens, F. K., Tarbuck, E. J., Herman, R. L., and Tasa, D. (2019). *The Atmosphere: An Introduction to Meteorology*. Pearson Education, fourtheenth edition.

[Makkonen, 2000] Makkonen, L. (2000). Models for the growth of rime, glaze, icicles and wet snow on structures. *Philosophical Transactions of the Royal Society of London. Series A: Mathematical, Physical and Engineering Sciences*, 358(1776):2913–2939.

[Makkonen and Stallabrass, 1987] Makkonen, L. and Stallabrass, J. (1987). Experiments on the cloud droplet collision efficiency of cylinders. *Journal of Applied Meteorology*, 26.

[Makkonen et al., 2018] Makkonen, L., Zhang, J., Karlsson, T., and Tiihonen, M. (2018). Modelling the growth of large rime ice accretions. *Cold Regions Science and Technology*, 151:133–137.

[Manwell et al., 2009] Manwell, J. F., McGowan, J. G., and Rogers, A. L. (2009). *Wind Energy Explained: Theory, Design and Application*. Wiley, second edition.

[Nakanishi and Niino, 2009] Nakanishi, M. and Niino, H. (2009). Development of an improved turbulence closure model for the atmospheric boundary layer. *Journal of the Meteorological Society of Japan. Ser. II*, 87(5):895–912.

[Niu et al., 2011] Niu, G.-Y., Yang, Z.-L., Mitchell, K. E., Chen, F., Ek, M. B., Barlage, M., Kumar, A., Manning, K., Niyogi, D., Rosero, E., Tewari, M., and Xia, Y. (2011). The community noah land surface model with multiparameterization options (noah-mp): 1. model description and evaluation with local-scale measurements. *Journal of Geophysical Research*, 116(D12).

[Nygaard et al., 2011] Nygaard, B. E. K., Kristjánsson, J. E., and Makkonen, L. (2011). Prediction of in-cloud icing conditions at ground level using the wrf model. *Journal of Applied Meteorology and Climatology*, 50(12):2445 – 2459.

[Olson et al., 2019] Olson, J. B., Kenyon, J. S., Angevine, W. A., Brown, J. M.,

Pagowski, M., and Sušelj, K. (2019). A description of the mynn-edmf scheme and the coupling to other components in wrf–arw. *National Oceanic and Atmospheric Administration (NOAA)*.

[Pu and Kalnay, 2018] Pu, Z. and Kalnay, E. (2018). Numerical weather prediction basics: Models, numerical methods, and data assimilation. *Handbook of Hydrometeorological Ensemble Forecasting*.

[Skamarock et al., 2021] Skamarock, W. C., Klemp, J. B., Dudhia, J., Gill, D. O., Liu, Z., Berner, J., Wang, W., Powers, J., Duda, M., Barker, D., et al. (2021). A description of the advanced research wrf version 4.3. *NCAR techical note*.

[Solbakken et al., 2021] Solbakken, K., Birkelund, Y., and Samuelsen, E. M. (2021). Evaluation of surface wind using wrf in complex terrain: Atmospheric input data and grid spacing. *Environmental Modelling Software*, 145:105182.

[Stull, 2018] Stull, R. (2018). *Practical Meteorology: An Algebra-based Survey of Atmospheric Science*. Sundog Publishing.

[Taylor, 2001] Taylor, K. E. (2001). Summarizing multiple aspects of model performance in a single diagram. *Journal of Geophysical Research: Atmospheres*, 106(D7):7183–7192.

[Thompson et al., 2008] Thompson, G., Field, P. R., Rasmussen, R. M., and Hall, W. D. (2008). Explicit forecast of winter precipitation using an improved bulk microphysics scheme part ii: Implementation of a new snow parameterization. *American Meteorolical Society*.

[Thompson et al., 2009] Thompson, G., Nygaard, B. E., Makkonen, L., and Dierer, S. (2009). Using the weather research and forecasting (wrf) model to predict ground/structural icing. *IWAIS XIII*.

[Turkia et al., 2013] Turkia, V., Huttunen, S., and Wallenius, T. (2013). Method for estimating wind turbine production losses due to icing. *VVT Technology*, (114).

[Wang et al., 2022] Wang, W., Bruyère, C., Duda, M., Dudhia, J., Gill, D., Kavulich, M., Werner, K., Chen, M., Lin, H.-C., Michalakes, J., Rizvi, S., Zhang, X., Berner, J., Munoz-Esparza, D., Reen, B., Ha, S., Fossell, K., Beezley, J. D., Coen, J. L., and Mandel, J. (2022). User's Guide For The Advanced Research WRF (ARW) Modeling System version 4.4, Chapter 3: WRF Preprocessing System (WPS). Retrieved: 19.02.24.

[Wang et al., 2023] Wang, W., Bruyère, C., Duda, M., Dudhia, J., Gill, D., Kavulich, M., Werner, K., Chen, M., Lin, H.-C., Michalakes, J., Rizvi, S., Zhang, X., Berner, J., Munoz-Esparza, D., Reen, B., Ha, S., Fossell, K., Beezley, J. D., Coen, J. L., and Mandel, J. (2023). User's Guide For The Advanced Research WRF (ARW) Modeling System version 4.5. Retrieved: 25.03.2024.

[Wetterzentrale, 2024] Wetterzentrale (2024). UKMO analysis. Retrieved 14.05.

[Wold et al., 2022] Wold, M., Rikheim, H., Hernes, B., and Østenby, A. M. (2022). Report 2022 norway. Technical report, IEA Wind Technology Collaboration Programme.

[Yang et al., 2011] Yang, Z.-L., Niu, G.-Y., Mitchell, K. E., Chen, F., Ek, M. B., Barlage, M., Longuevergne, L., Manning, K., Niyogi, D., Tewari, M., and Xia, Y. (2011). The community noah land surface model with multiparameterization options (noah-mp): 2. evaluation over global river basins. *Journal of Geophysical Research*, 116(D12).

[Øyvind Byrkjedal et al., 2009a] Øyvind Byrkjedal, Åkervik, E., and Kjeller Vindteknikk (2009a). *Vindkart for Norge*. Technical Report 9.

[Øyvind Byrkjedal et al., 2009b] Øyvind Byrkjedal, Åkervik, E., and Kjeller Vindteknikk (2009b). *Vindkart for Norge. Kartbok 3a: Isingkart i 80m høyde*. Technical report.

Appendix A

Contents of the windturbines.txt file used for the wind turbine scheme. Since the file is very long, it is split half way to fit it on one page.

```
70.19447 26.32963 1 #turbine 1    70.18960 26.23196 1 #turbine 51
70.18519 26.36561 1 #turbine 2    70.11228 26.29277 1 #turbine 52
70.18827 26.34966 1 #turbine 3    70.18038 26.40144 1 #turbine 53
70.07793 26.22688 1 #turbine 4    70.15754 26.41002 1 #turbine 54
70.18818 26.32586 1 #turbine 5    70.15948 26.21459 1 #turbine 55
70.18167 26.38422 1 #turbine 6    70.13229 26.25122 1 #turbine 56
70.18459 26.21496 1 #turbine 7    70.17160 26.21678 1 #turbine 57
70.13902 26.25230 1 #turbine 8    70.15956 26.23307 1 #turbine 58
70.08724 26.31073 1 #turbine 9    70.19086 26.21340 1 #turbine 59
70.15765 26.44301 1 #turbine 10   70.13521 26.30913 1 #turbine 60
70.14102 26.30498 1 #turbine 11   70.10217 26.34577 1 #turbine 61
70.16655 26.42297 1 #turbine 12   70.16513 26.27908 1 #turbine 62
70.17535 26.37384 1 #turbine 13   70.10106 26.29184 1 #turbine 63
70.17977 26.35653 1 #turbine 14   70.12318 26.33061 1 #turbine 64
70.07982 26.24917 1 #turbine 15   70.14288 26.32206 1 #turbine 65
70.18199 26.23488 1 #turbine 16   70.15423 26.24515 1 #turbine 66
70.14989 26.27961 1 #turbine 17   70.14678 26.40900 1 #turbine 67
70.13559 26.29066 1 #turbine 18   70.15176 26.29934 1 #turbine 68
70.16575 26.21304 1 #turbine 19   70.15181 26.44053 1 #turbine 69
70.16073 26.42709 1 #turbine 20   70.10844 26.34557 1 #turbine 70
70.14591 26.29426 1 #turbine 21   70.11875 26.34525 1 #turbine 71
70.19540 26.22513 1 #turbine 22   70.17182 26.38848 1 #turbine 72
70.09391 26.29734 1 #turbine 23   70.12402 26.31346 1 #turbine 73
70.13549 26.26693 1 #turbine 24   70.10649 26.30350 1 #turbine 74
70.18788 26.24921 1 #turbine 25   70.15705 26.27672 1 #turbine 75
70.08492 26.29107 1 #turbine 26   70.16071 26.29376 1 #turbine 76
70.17537 26.26023 1 #turbine 27   70.11334 26.33488 1 #turbine 77
70.17184 26.27488 1 #turbine 28   70.11716 26.27943 1 #turbine 78
70.09092 26.33429 1 #turbine 29   70.08563 26.24633 1 #turbine 79
70.09675 26.33673 1 #turbine 30   70.10728 26.27714 1 #turbine 80
70.17457 26.40689 1 #turbine 31   70.11778 26.32288 1 #turbine 81
70.14091 26.27597 1 #turbine 32   70.13260 26.21957 1 #turbine 82
70.08213 26.26618 1 #turbine 33   70.16153 26.39670 1 #turbine 83
70.16584 26.23284 1 #turbine 34   70.09949 26.23661 1 #turbine 84
70.17619 26.24302 1 #turbine 35   70.13888 26.21933 1 #turbine 85
70.09027 26.28300 1 #turbine 36   70.11103 26.31784 1 #turbine 86
70.11861 26.30573 1 #turbine 37   70.09371 26.24866 1 #turbine 87
70.14443 26.26002 1 #turbine 38   70.11293 26.23348 1 #turbine 88
70.18105 26.33667 1 #turbine 39   70.14254 26.23766 1 #turbine 89
70.15310 26.42202 1 #turbine 40   70.14796 26.24538 1 #turbine 90
70.09308 26.31448 1 #turbine 41   70.14728 26.42746 1 #turbine 91
70.18207 26.25470 1 #turbine 42   70.12785 26.26324 1 #turbine 92
70.13626 26.23657 1 #turbine 43   70.13024 26.29875 1 #turbine 93
70.13105 26.27895 1 #turbine 44   70.10358 26.24962 1 #turbine 94
70.15341 26.26233 1 #turbine 45   70.10525 26.32988 1 #turbine 95
70.16098 26.25018 1 #turbine 46   70.12460 26.34902 1 #turbine 96
70.09983 26.32084 1 #turbine 47   70.14025 26.33798 1 #turbine 97
70.17834 26.22048 1 #turbine 48   70.14560 26.21908 1 #turbine 98
70.16829 26.40575 1 #turbine 49   70.15281 26.22804 1 #turbine 99
70.16726 26.25127 1 #turbine 50   70.08795 26.26334 1 #turbine 100
```

Appendix B

Contents of the wind-turbine1.tbl file used for the wind turbine scheme.

```
24
200. 164. 0.1 8.0
2.       0.8      0.
3.       0.8      0.
4.       0.8      100.
5.       0.82     650.
6.       0.85     1150.
7.       0.78     1850.
8.       0.71     2900.
9.       0.65     4150.
10.      0.59     5600.
11.      0.52     7100.
12.      0.45     7800.
13.      0.38     8000.
14.      0.32     8000.
15.      0.27     8000.
16.      0.22     8000.
17.      0.18     8000.
18.      0.14     8000.
19.      0.13     8000.
20.      0.12     8000.
21.      0.12     8000.
22.      0.11     8000.
23.      0.11     8000.
24.      0.10     8000.
25.      0.10     8000.
```